CRUSTAL STRUCTURE IN SOUTHERN CALIFORNIA FROM ARRAY DATA

Thesis by

Thomas Martin Hearn

In Partial Fulfillment of the Requirements

for the Degree of

Doctor of Philosophy

California Institute of Technology

Pasadena, California

1985

(Submitted November 2, 1984)

To my parents

Carolyn Ruth Hearn and Thomas Muir Hearn

Acknowledgements

It is rare in life that one is able to pursue his own interests, do his own work and learn from his own mistakes in as open an atmosphere as at the Seismo. Lab. It is for this experience that I would most like to thank the faculty, students and staff at the Caltech Seismology Lab.

I would like to thank the faculty for their quiet support including Rob Clayton for being my advisor for most of my stay at Caltech. It was he who introduced the concept of tomography that led to chapters 3 and 4. J. Bernard Minster and Hiroo Kanamori also acted as advisors during my stay at Caltech. It was Bernard who first got me interested in the Southern California array data. Dave Harkrider was my academic advisor. Lee Silver has acted as my primary motivator and advisor toward the geologic implications of this work. Discussions with Don Anderson and Brad Hager are also appreciated. Shawn Biehler at the University of California, Riverside, was the one who first encouraged me to follow a career in geophysics.

Almost all of the data used in this thesis was collected on the digital Southern California array. The array staff all deserve credit and thanks for making the data possible. Carl Johnson brought the array to its modern state by introducing the digital earthquake collection and processing systems used in the array. The day to day operations and data collection was run by Kate Hutton with the help of Geary Riley, Kathy Watts, Ann Blanchard, Peter

German, Doug Given, Gary Guteriez, Victor Lamanuzzi and many others.

My interest in array data has coincided with that of many of the students. Eugene Humphreys, Marianne Walck, and Victor Lamanuzzi all have worked with the array data and discussions with them about their work are appreciated. Ed Corbett cleverness in deciphering the array data has saved me and many others a great deal of work. Jennifer Haase worked on some very useful software for extracting the array data.

Chapter 2, having been published, benefited greatly from the detailed reviews of Dave Hadley and Jim Pechmann.

I would also like to thank my officemates, Ronan LeBras, Mark Richards and Doug Schmitt, for putting up with me and for keeping the office full. The work in this thesis was supported by the U.S.G.S., contract number 14-08-001-21210 and by Sun Oil Company.

Abstract

Crustal structure in Southern California is investigated using travel times from over 200 stations and thousands of local earthquakes. The data are divided into two sets of first arrivals representing a two-layer crust. The Pg arrivals have paths that refract at depths near 10 km and the Pn arrivals refract along the Moho discontinuity. These data are used to find lateral and azimuthal refractor velocity variations and to determine refractor topography.

In Chapter 2 the Pn raypaths are modeled using linear inverse theory. This enables statistical verification that static delays, lateral slowness variations and anisotropy are all significant parameters. However, because of the inherent size limitations of inverse theory, the full array data set could not be processed and the possible resolution was limited. The tomographic backprojection algorithm developed for Chapters 3 and 4 avoids these size problems. This algorithm allows us to process the data sequentially and to iteratively refine the solution. The variance and resolution for tomography are determined empirically using synthetic structures.

The Pg results spectacularly image the San Andreas Fault, the Garlock Fault and the San Jacinto Fault. The Mojave has slower velocities near 6.0 km/s while the Peninsular Ranges have higher velocities of over 6.5 km/s. The San Jacinto block has velocities only slightly above the Mojave velocities. It may have overthrust Mojave rocks. Surprisingly, the Transverse Ranges are not apparent at Pg depths. The batholiths in these mountains are possibly only surficial.

Pn velocities are fast in the Mojave, slow in Southern California Peninsular Ranges and slow north of the Garlock Fault. Pn anisotropy of 2% with a NWW fast direction exists in Southern California. A region of thin crust (22 km) centers around the Colorado River where the crust has undergone basin and range type extension. Station delays see the Ventura and Los Angeles Basins but not the Salton Trough, where high velocity rocks underlie the sediments. The Transverse Ranges have a root in their eastern half but not in their western half. The Southern Coast Ranges also have a thickened crust but the Peninsular Ranges have no major root.

Table of Contents

Chapter 1

Introduction

Crustal structure and earthquake travel times

In this thesis the Southern California array is used to deduce the gross features of Southern California crustal structure. This, in turn, allows us to see more clearly the imprint that tectonic process, past and present, have left on the crust. These processes have left their signature, primarily lateral structural variations, and it is these lateral variations that this work will focus on. The vertical variations in structure have already been extensively studied and they provide a foundation to build upon.

Early studies of California earthquakes found two main phases that dominated as first arrival. Their apparent linearity on a travel time plot enables an easy interpretation as refracted arrivals. The Pg arrivals refract in the upper crust and have apparent velocities of near 6.2 km/s with variations of over 0.2 km/s over the array. The Pn arrivals refract along the Moho discontinuity at depths around 30 km and have apparent velocities around 7.9 km/s. Pn velocity can also vary by 0.3 km/s. It is difficult to investigate since Pn anisotropy is commonly observed world wide as well locally (Raitt et al., 1969, 1971; Vetter and Minster, 1981). Other phases have also been documented. Near the earthquake a direct phase, $\overline{P}$, is usually seen, especially if

the event is deep. The direct phase will have a nonlinear travel time moveout. Often a fast midcrustal refracted phase, P^*, is seen. This phase has a higher apparent velocity of 6.5 km/s or more. Sometimes P^* is seen as the first arrival instead of Pg. Other times it is seen as an extra first arrival branch between Pg and Pn thus indicating refraction off a deeper crustal layer. Without detailed refraction profiles it is often difficult to differentiate between P^* and Pg. In this thesis they will both be treated as Pg.

In the Peninsular Ranges P^* is observed at velocities of 6.5-7.0 km/s arriving from depths near 14 km (Hadley, 1978). Slower material with more normal Pg velocity overlies this (Hadley 1978; Simmons, 1977). Estimates of Pn velocity are near 8.0 km/s (Simmons, 1977; Nava and Brune, 1983). The existence of a root in this area is an important question that will be addressed in the thesis. Nava and Brune (1983) estimate a crustal thickness of 40 km for the region. Gravity, however, does not clearly reflect a root. Instead gravity shows a large uncompensated isostatic gravity high in the region between San Diego and the Elsinore Fault (Oliver, 1981).

High P^* velocities have also been seen in the San Gabriel Mountains and the Santa Monica Mountains while in the rest of the region Pg velocities of 6.2 km/s are normal (Hadley,1978). Studies of the Transverse Ranges have given somewhat scattered results. Hadley observed a reversed Pn velocity of 8.3 km/s in the area but other researchers have been unable to find similar velocities (Keller ,1983; Lamanuzzi, 1980). This phase arrives as a small precursor to the Pn arrivals and may often be missed in routine travel time picking. Geological studies indicate that the San Gabriel batholith has been

transported northward along the San Andreas Fault and that the westernmost Transverse Ranges have undergone ninety degree rotations (Powell, 1981; Luyendyk et al., 1980). A small root exists under the San Bernardino portion of the range but not under the San Gabriel portion (Lamanuzzi, 1980). Isostatically this is not a problem. Oliver (1981) points out that the average elevation of the San Gabriel mountains near Mt. San Antonio is only 700 m and the average elevation rises well into the Antelope Valley region. A local root is then not needed to balance the San Gabriels.

A major part of the interest in the Transverse Range area comes from the mantle high velocity anomaly that underlies the mountains (Humphreys et al., 1984; Walck, 1982; Raikes, 1980; Hadley,1978). The high velocity feature is a narrow slab-like zone extending from near the base of the crust to 250 km down. The fact that this feature, as well as the mountain range, is not offset by the San Andreas Fault led Hadley and Kanamori (1977) to propose that the plate boundary in the mantle lies to the east of the Transverse Range province at depth. Undoubtedly the height of the Transverse Ranges is related to the curvature in the big bend region of the San Andreas Fault. The coincidence of the high velocity ridge with the topographic high is astonishing but a direct relationship is not clear.

Pn velocities average 8.2 km/s along the coast north of Los Angeles and 7.8 km/s between Los Angeles and Lake Mead (Roller and Healy, 1963; Healy, 1963). Normal depths near 30 km were also found in those areas. In the Salton Trough, however, crustal thickness of near 20 km and apparent velocities of 7.8 km/s exist (Hadley, 1978). Refraction studies of the Trough find that

the surface sediments are rapidly metamorphosed with depth and that mafic intrusives form a shallow high velocity basement (Fuis et al., 1982). Humphreys et al. (1984) find low velocity mantle in the first 100 km beneath the Trough. The actual Moho and mantle structure underneath the Salton Trough reflect the type of mechanism that causes spreading in this major continental rift zone.

Most studies of crustal structure in the past have focused on determining the vertical velocity structure. In this thesis, I focus on the lateral variations in structure. Lateral variations in velocity and structure are more directly related to the laterally varying surface geology. Processes observed on the surface may be substantially different from those at depth where ductile deformation occurs. By studying lateral velocity variations at depth we effectively extend our knowledge of the surface geology and tectonics downward.

Review of the data

It would be short sighted to simply mass process the data without first developing a qualitative feel for the data quality and the amount of information available. To do this one must understand how the data are gathered. Also, a short observational review of some individual travel time curves can give information which can be used as a check for further results.

Although data have been collected at Caltech for the purpose of locating earthquakes since 1932, it was not until 1977 that the array was updated to digitally record traces from all stations (Johnson, 1979). Prior to this events

were recorded either on film or paper. Because of the inherent clumsiness involved in using films and picking arrivals off them, the number of stations used and the number of events located was limited. Also, error control was not complete. When CEDAR recording system was introduced in June 1977 the array processing became much more automated and consistent.

The CEDAR system automatically triggered on each earthquake and 160 stations were then recorded in a multiplexed manner. The arrival times were interactively picked by members of the USGS staff at Caltech. Each individual trace was displayed upon a terminal, a cursor was moved to the arrival, and then, by pushing a button, the position of the cursor was converted to an arrival time and automatically stored. All the processor had to do was correctly identify the arrival and line the cursor up on it. With the picking of the time the user would also record other trace attributes. These were the first motion (up or down), the arrival type (impulsive or emergent) and the data quality (0, 1, 2, 3, or 4). More than one arrival could be recorded per trace.

Figure 1 is a composite travel time plot of all first arrivals recorded on the CEDAR system. Note that some S arrivals have been incorrectly picked as first arrivals . Also there is a background scatter of outliers in this plot. The CEDAR system ran until June 1980 when events at Mammoth Lakes, California, overwhelmed the system and the new recording system CUSP was being implemented.

The new system, CUSP, introduced new and more efficient data storage formats. Also, the interactive time picking system was improved. With CUSP,

multiple traces can be displayed on the screen with a given reduction velocity. Thus a simulated time-distance plot is shown. Since the traces are then visually side by side mispicks due to bad traces, crossed wires and multiple events are easily recognized and avoided. The data from this system is shown in Figure 2. Note that there are no S arrivals nor is there a background of outliers. The CUSP recording system began in February 1981 and ran until the end of 1983.

Data qualities picked are especially relevant to work presented here. Picks range from near perfect to useless. Quality 0 picks have the highest accuracy of almost 0.02 s, the digitization interval. Quality 4 picks are guesses and are never used. Qualities 1, 2, and 3 range between the two extremes and are picked subjectively by the processor. For the purposes of weighting the data, standard errors of 0.05s, 0.10s, 0.20s and 0.50s were used for the quality 0, 1, 2 and 3 arrivals, respectively. These are reasonable estimates of the accuracy.

An example of a well recorded and located event is shown in Figure 3. This is a magnitude 4.9 event occurring at Big Bear which is in the center of the array. Most of the traces on this plot are clipped. Two travel time branches are apparent, the very linear Pg branch and a later Pn branch. The quality of the arrivals degrades with distance. The travel time picks for this event are shown in Figure 4. Although this event is extremely well located, considerable scatter exists in the Pn data. This scatter is due to the structural variations in Southern California that we wish to investigate.

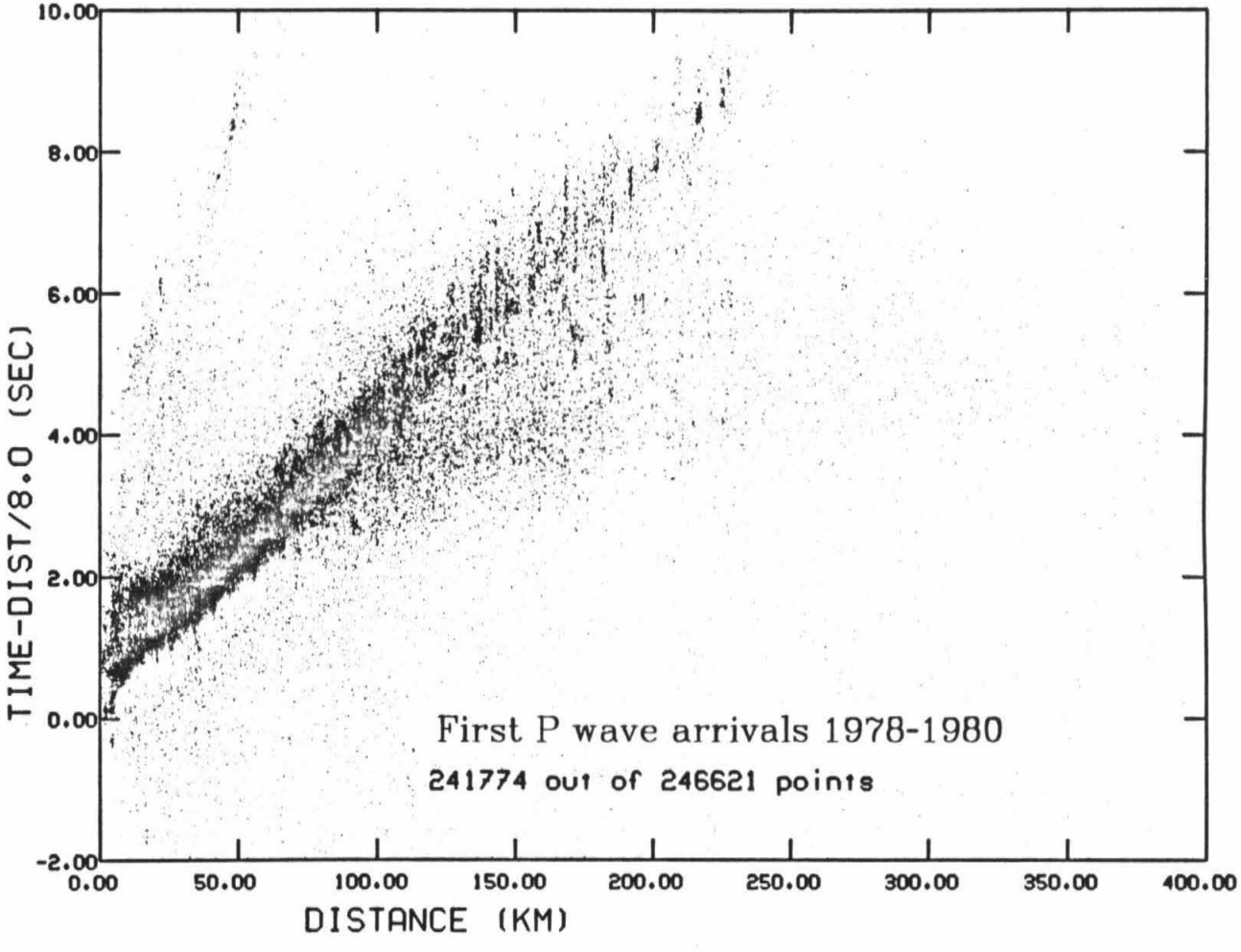

Figure 1. P wave first arrivals from the southern California array, 1978-1980.

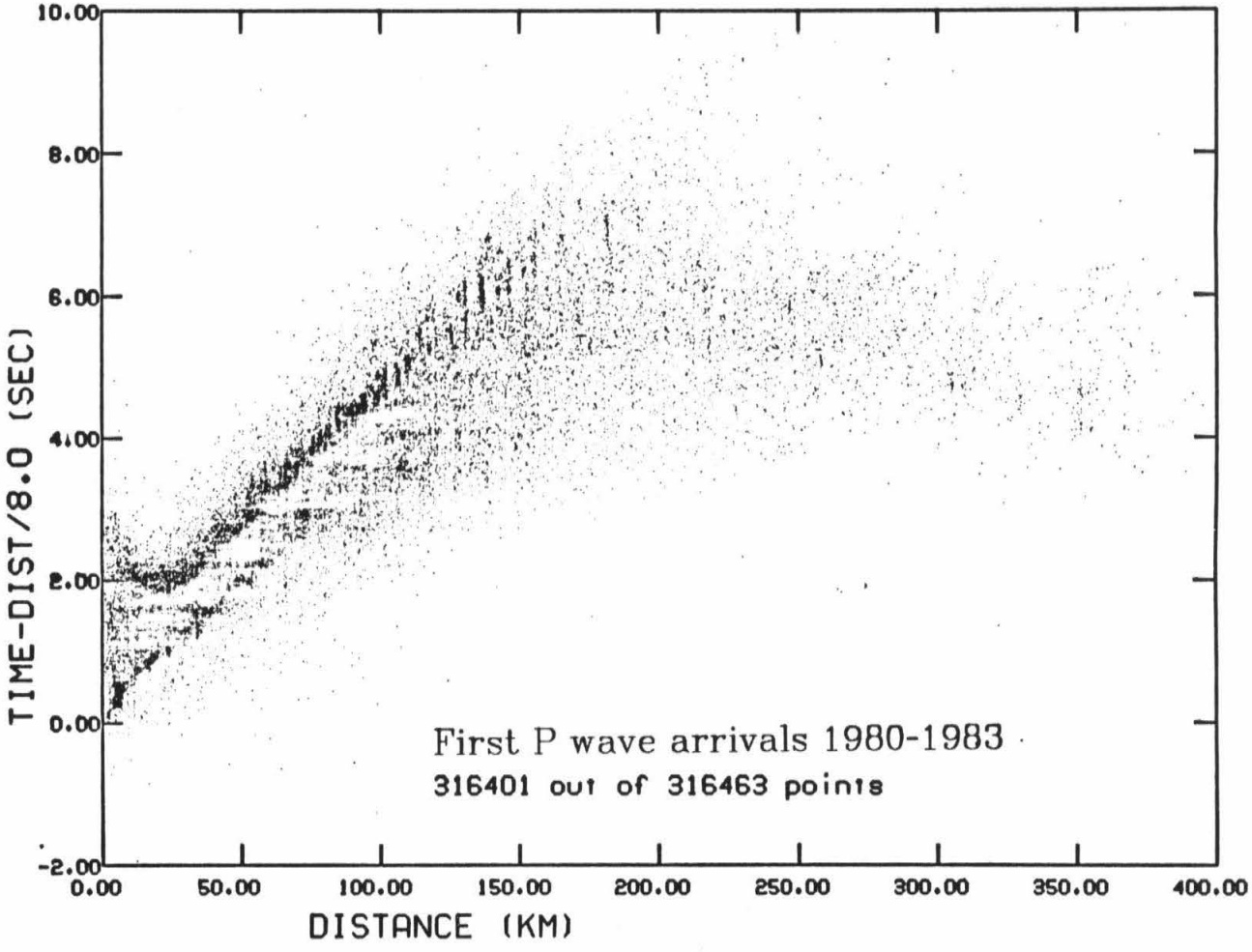

Figure 2. P wave first arrivals from the Southern California array, 1980-1983.

Two more event travel time plots are shown in Figures 5 and 6. These are for the 1978 Santa Barbara earthquake and the 1979 Imperial Valley earthquake. Both these travel time plots are dominated by high quality arrivals and both are well-located. Despite this, both these figures show considerable scatter. The Santa Barbara event shows considerable scatter in both the Pg and Pn branches. This arises due to the complicated structures east of Santa Barbara which include the Ventura and Los Angeles basins, the Transverse Ranges, and complications associated with the San Andreas Fault. The Imperial Valley event does not show a clear cross over form Pg to Pn and has a low overall Pn velocity. This is characteristic of events in this area. Also, Pn stations in the Mojave did not record well despite the large size of this earthquake. Again, this seems to be common for events in this area. The scatter in these travel time plots is the data that we will use to determine crustal structure.

In order to study Pn arrivals, one of the first steps was to get a set of well-recorded events. For this purpose, 65 events were collected and travel time plots were made for each. To obtain an overview of variations in crustal velocity, the velocities for each event were estimated and noted on a map. A transparent overlay with various slopes printed on it was used to estimate Pg and Pn velocities. In Figures 7 and 8 the Pg and Pn velocities, respectively, are noted at the earthquake epicenter. Events within the array have raypaths in all directions while events on the edge of the array have raypaths directed into the array. These plots, though crude, demonstrate the geographical variations found in velocities. They have provided a quick check for

more detailed results. Pg velocities vary from 6.0 to 7.0 km/s. Low velocities are found in the Mojave, and the highest are in the Imperial Valley and Baja California. The Peninsular Ranges have events with higher Pg velocities of 6.5 km/s into the Anza region. Offshore Pg velocities are 6.3-6.5 km/s. Pn velocities vary form 7.6 to 8.3 km/s. Low velocities are found from events in Baja California and the southern Imperial Valley; high velocities are found from events in the southern Sierra and offshore. Velocities for both Pn and Pg are very consistent in the Mojave where travel time curves are often strikingly linear.

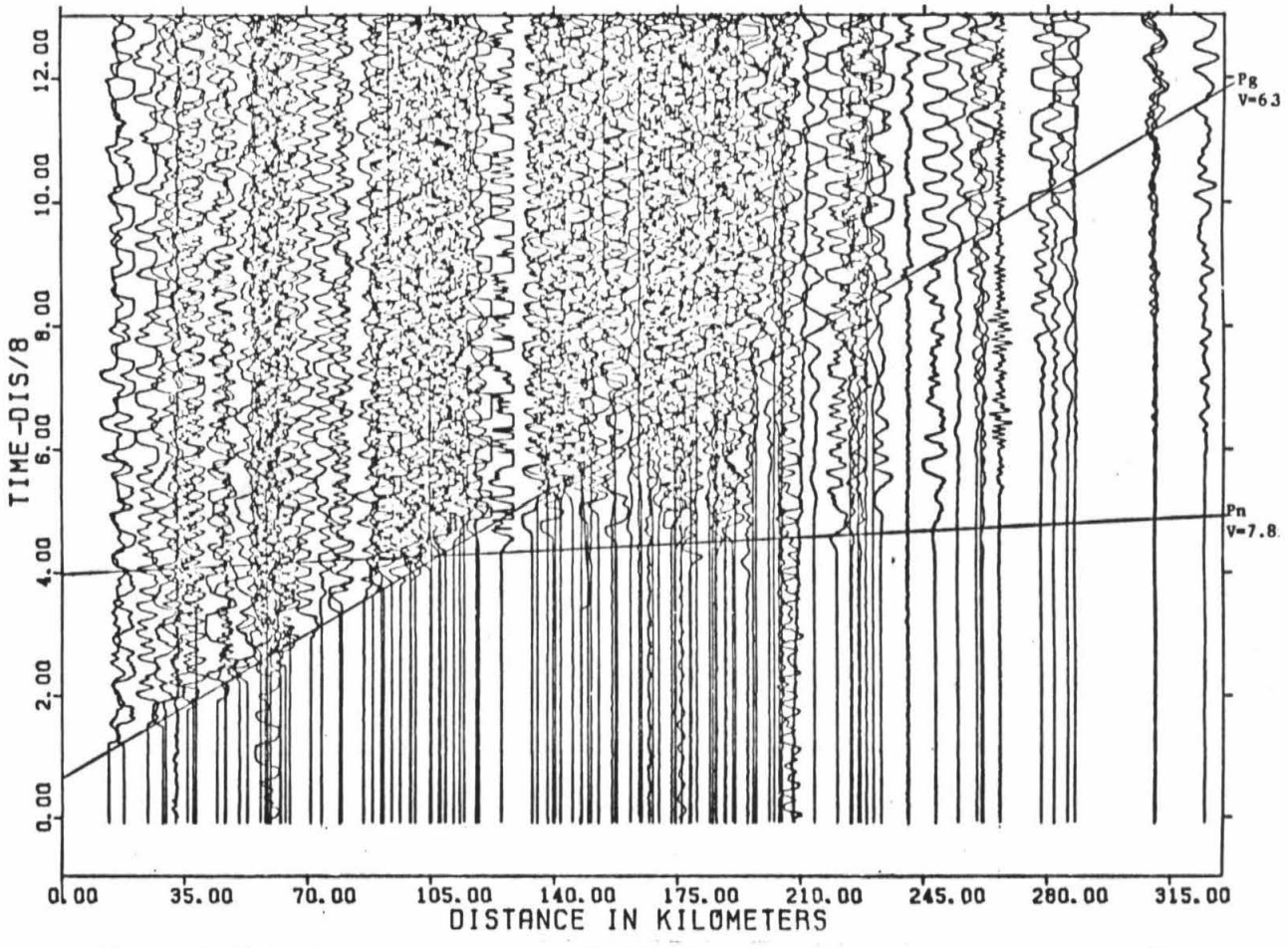

Figure 3. Data from the Southern California array for a magnitude 4.9 earthquake in the center of the array, at Big Bear, showing the Pg and Pn travel time branches. Note the linearity of these segments despite the broad area covered by these arrivals.

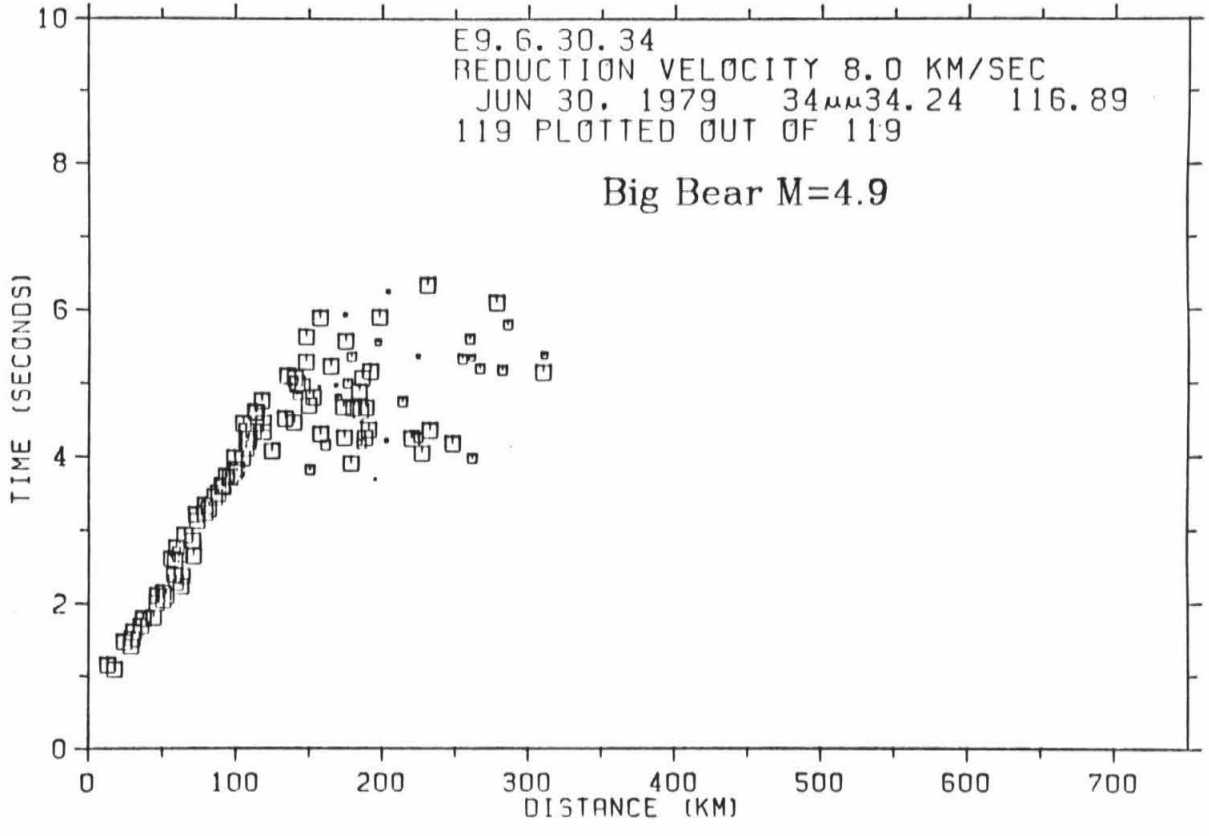

Figure 4. Travel time data for the event at Big Bear shown in Figure 3.

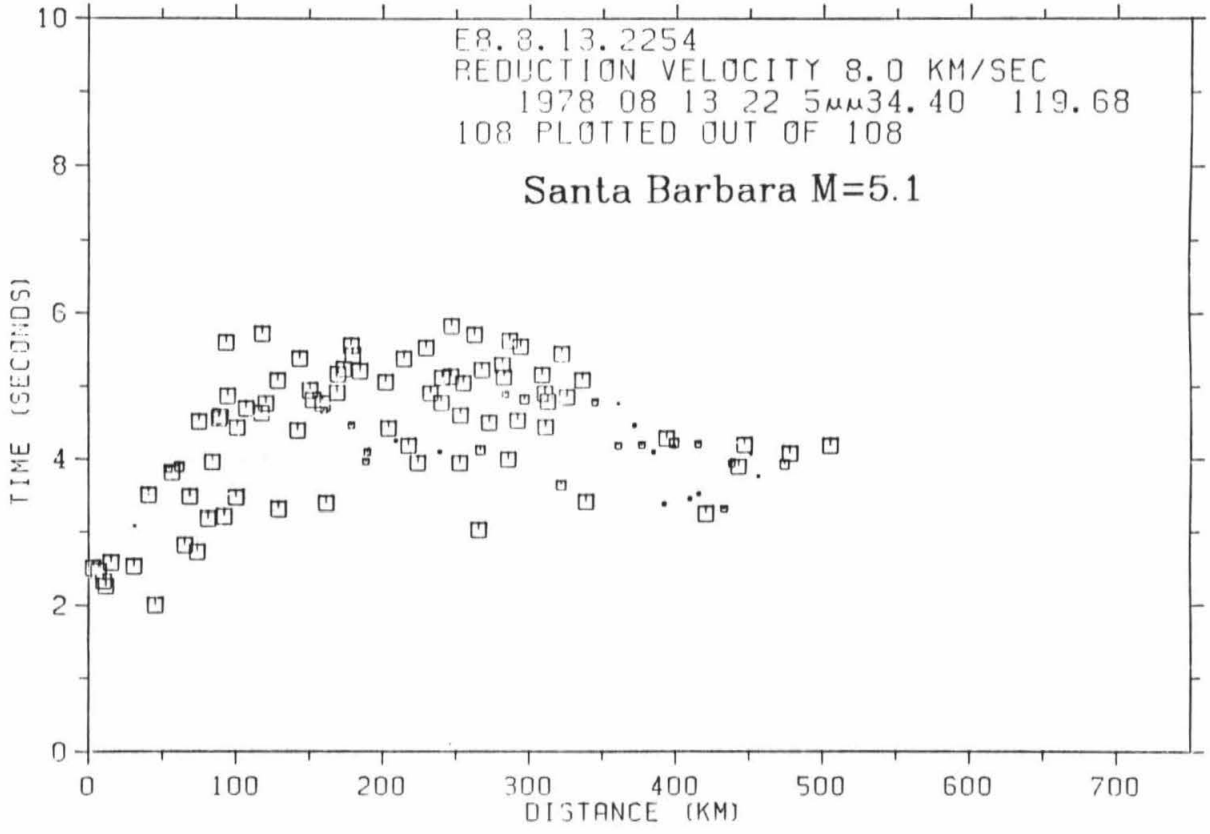

Figure 5. Travel time data for an event occurring on August 13, 1978 at Santa Barbara.

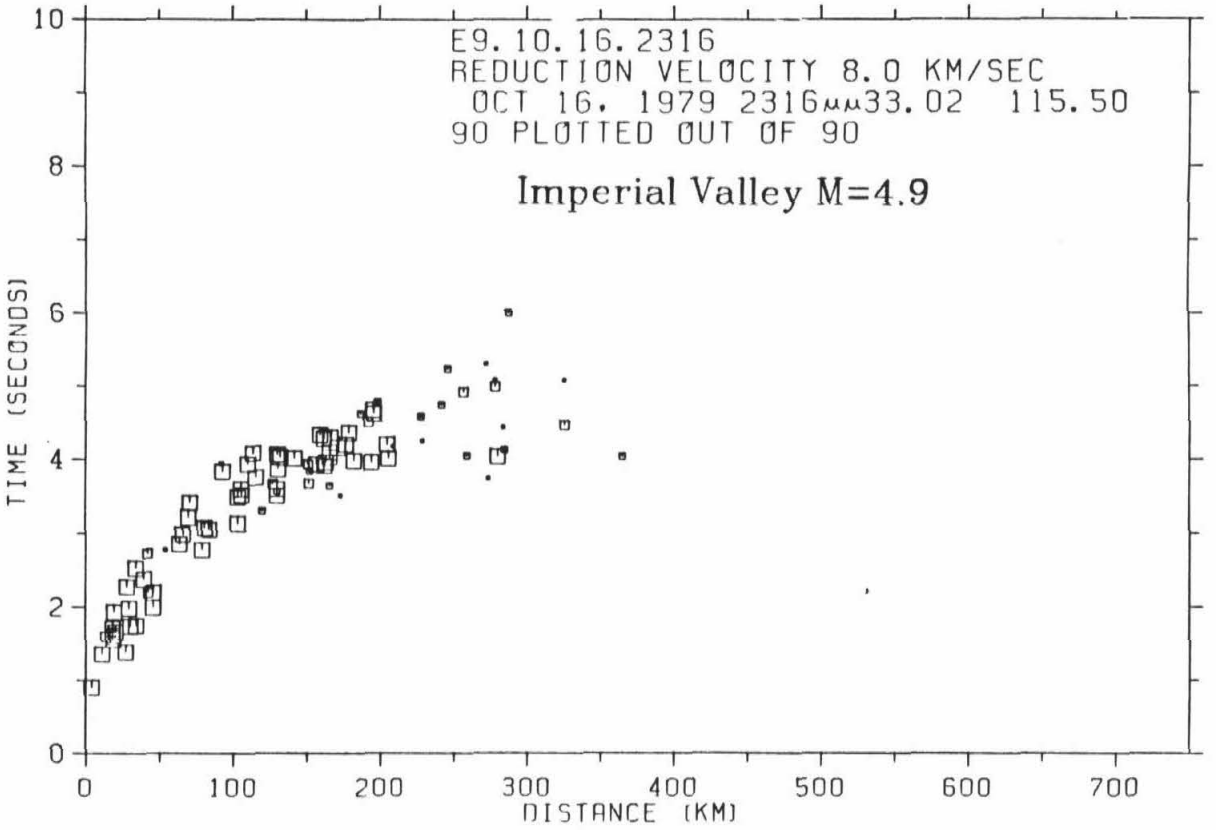

Figure 6. Travel time data for an event occurring on October 16, 1979 in the Imperial Valley.

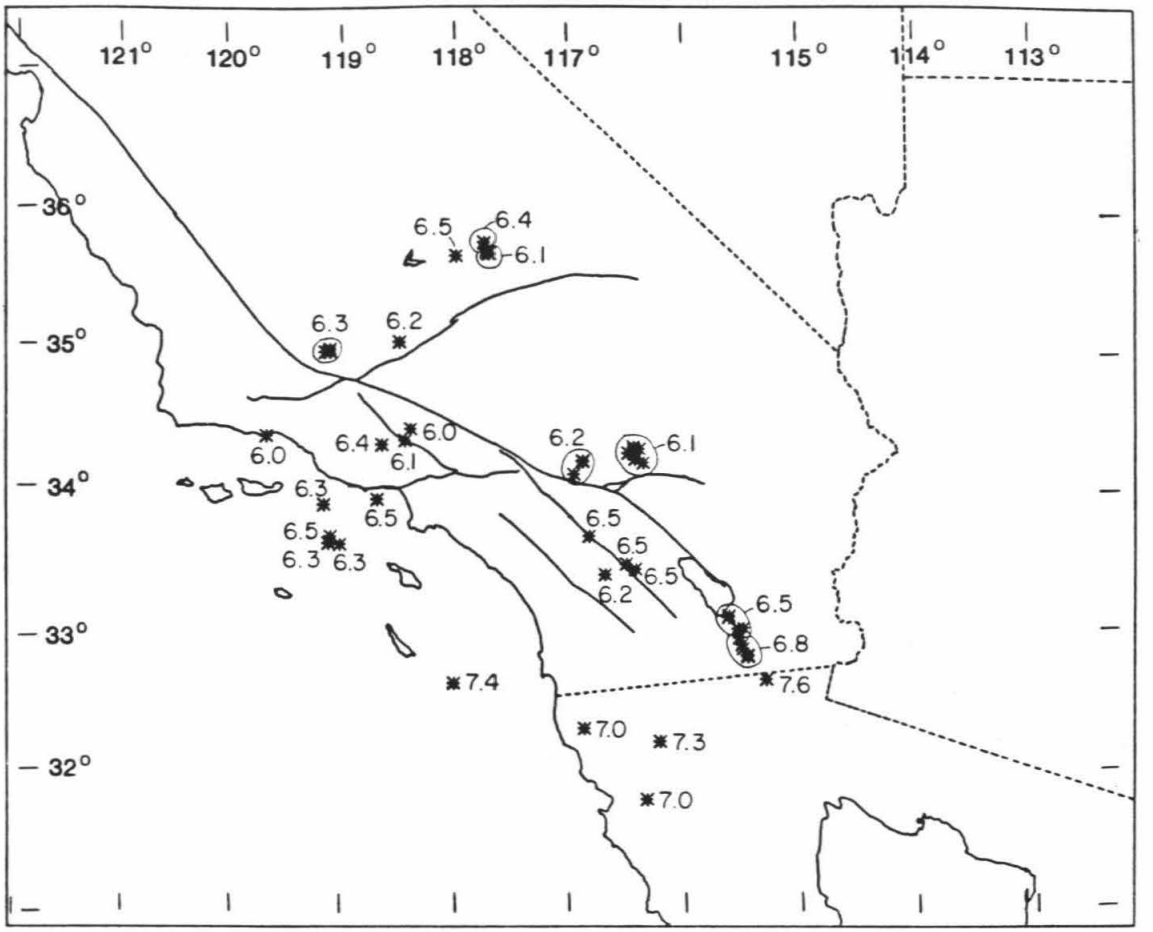

Figure 7. Apparent Pg velocities for some events in Southern California. They range from 6.1 to 7.4 km/s.

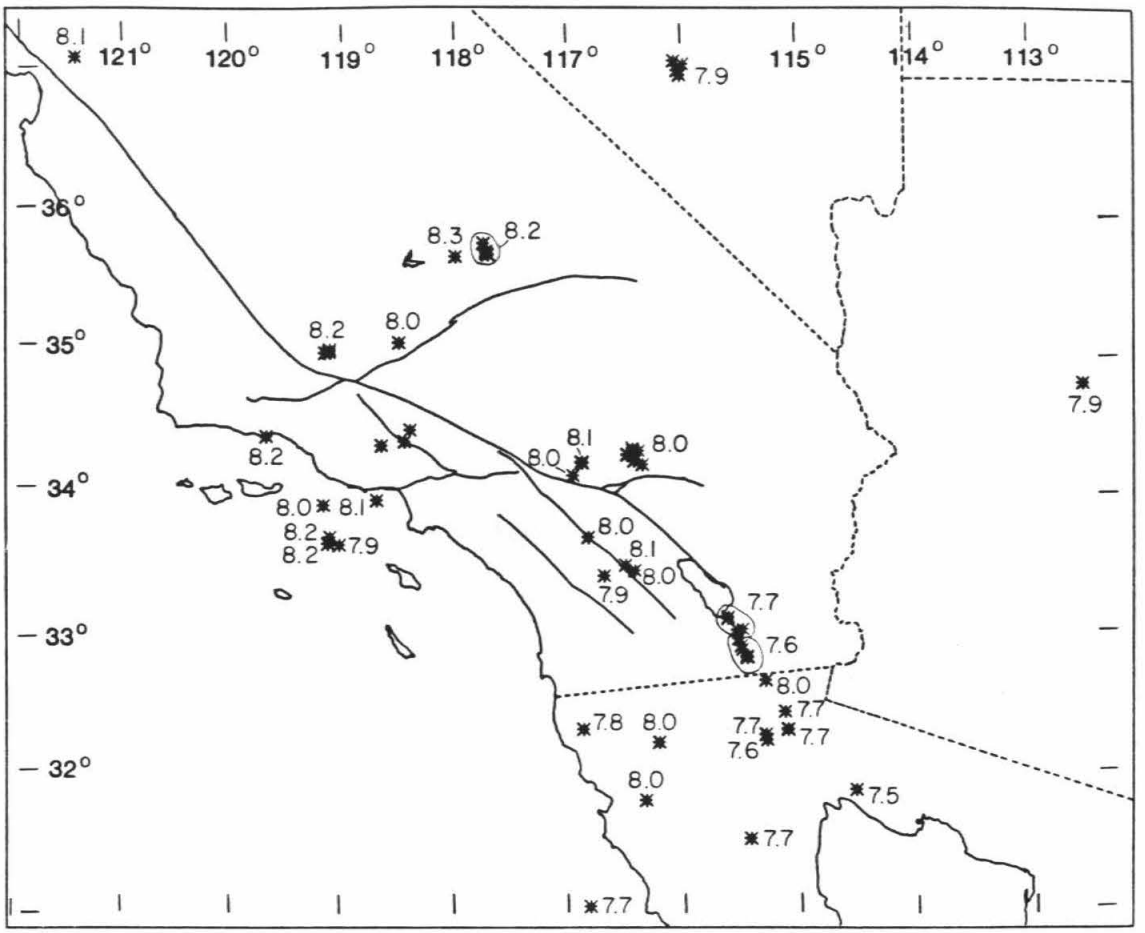

Figure 8. Apparent Pn velocities for some events in Southern California. They range from 7.6 to 8.3 km/s.

Chapter 2

Pn Travel Times in Southern California

Introduction

The Southern California array (Figure 1) has been used extensively to study upper mantle heterogeneity [Hadley and Kanamori, 1977; Raikes and Hadley, 1979; Raikes, 1980; Walck and Minster, 1982]. Little is known, however, about systematic lateral variations in crustal structure. Hadley [1978] analyzed several refraction profiles in Southern California. He found that the Pg arrivals (the first arrival from 20 to 135 km) have velocities between 6.1 and 6.6 km/s and that the Pn arrivals have velocities between 7.7 and 8.2 km/s. For profiles in the Transverse Ranges, Hadley observed a subcrustal arrival of 8.3 km/s. Ergas and Jackson [1981] analyzed upper crustal velocities and found little variation in the upper crustal velocity of 6.1 km/s. Lamanuzzi [1981] demonstrated that considerable variation occurs in the Pn arrivals. He confirmed the crustal thinning under the Salton Trough and found evidence for a 3- to 8-km root to the San Bernardino Mountains. Nava and Brune [1982] found a narrow root under the Peninsular Ranges.

Moho anisotropy was found to be present in Southern California by Vetter and Minster [1981]. They specifically looked for evidence of anisotropy under the Pasadena and Mojave regions. Although none was found in the Mojave, Pasadena showed an apparent anisotropy of 3-3.5% in which the fast axis of anisotropy paralleled the azimuth of plate motion along the San

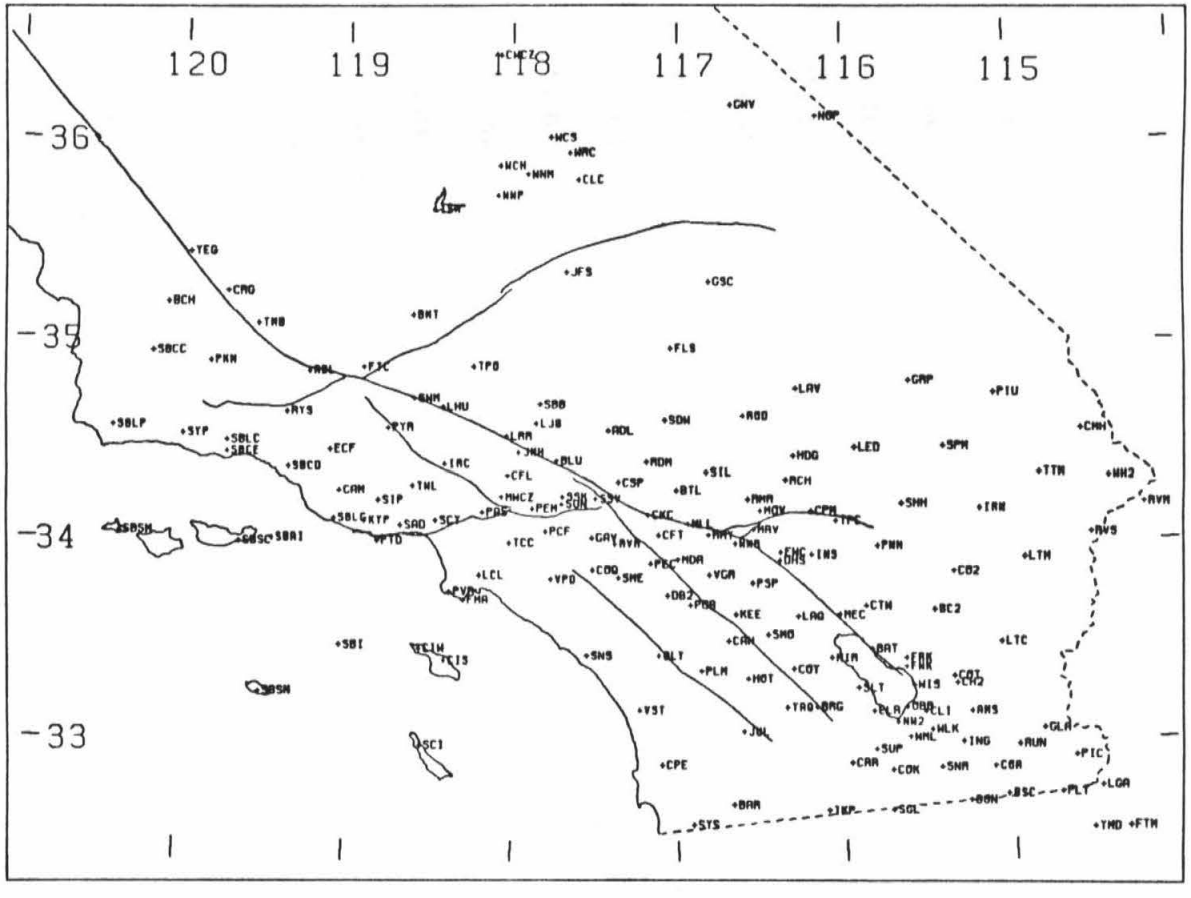

Figure 1. Map of stations of the Joint USGS-Caltech Southern California Seismographic Network used in this study.

Andreas Fault. This suggests that the cause of anisotropy is related to shear stress. Other investigators, Bamford et al. [1979], Raitt et al. [1969, 1971], and Morris et al. [1969], have found apparent anisotropy underneath the western United States and in the Pacific Ocean off California and Hawaii. Their studies used the time term refraction method, which will be used here.

The time term method of refraction seismology was first introduced by Scheidegger and Willmore [1957] and Willmore and Bancroft [1960]. This method allows us to determine crustal delay times that can be interpreted in terms of Moho topography. Raitt et al. [1969, 1971] and Morris et al. [1969] extended this method to account for anisotropy and applied it to oceanic data collected in the Pacific Ocean. They used the method to show 8% anisotropy in the 6-km-thick crust off Hawaii. Bamford et al. [1979] applied this method to northern Britain and the eastern and western United States. They found the latter to be anisotropic by nearly 3%. Bamford [1973a, b, 1977] also did extensive work on West German data. He found that crustal thickness increases toward the Alps and also concluded that 6-7% anisotropy was present.

Method

In this study, an expanded form of the time term method is derived and then is used to determine delay times, lateral velocity variations, and regional anisotropy. The vast amount of data from the Southern California array and the heterogeneous source and station distribution make this method ideal for application to Southern California.

The travel time between an event and a station overlying a horizontal velocity boundary can be expressed as

$$t_{es} = \Delta_{es} \cdot S + \tau_e + \tau_s \qquad (1)$$

where Δ_{es} is the horizontal distance between event "e" and station "s"; S is the refractor slowness; and τ_s and τ_e are the source time term for station "s" and the event time term for event "e." They can be expressed as

$$\tau_s = \int_0^h (S(z)^2 - S^2)^{1/2}\, dz \qquad (2)$$

$$\tau_e = \int_z^h (S(z)^2 - S^2)^{1/2}\, dz \qquad (3)$$

Here, h is the Moho depth and z is the depth of event e. $S(z)$ is the crustal slowness profile. Slowness, the inverse of velocity, is the linear medium parameter in the time term equation. It will be used instead of velocity in what follows to describe the medium.

The time terms, or delays, are important because for a constant velocity crust they are proportional to the crustal thickness. This will be their primary interpretation. Although both the Pn slowness and the crustal slowness profile affect the magnitude of the time terms, excessive slowness perturbations are required to change their values appreciably. The time terms may be thought of as the intercept time on a time-distance plot of refraction travel time data. Since the depths of the earthquakes are not accurately known, no attempt will be made to interpret their relative time terms. They serve to partially absorb errors in the event locations.

This travel time equation is accurate for nearly horizontal or slightly warped refractors [Scheidegger and Willmore, 1957; Willmore and Bancroft, 1960; Bath, 1978]. Using a data set of many source-receiver pairs we can set up a system of linear equations,

$$\mathbf{Ax} = \mathbf{t} \tag{4}$$

The **A** is a matrix containing the parameter coefficients of (1). It contains mostly zeros and ones with one column listing the event-source distance. The vector **x** contains the unknown time terms and the unknown slowness. And the **t** vector contains the observed travel times. The least squares solution is given by

$$\mathbf{x} = (\mathbf{A}^T\mathbf{A})^{-1}\mathbf{A}^T\mathbf{t} \tag{5}$$

In solving the time term equations it is necessary to specify an additional condition to keep the equations from being singular. It is clear from (1) that τ_e can be increased by an arbitrary amount and τ_s decreased by the same amount and still satisfy the equation. To constrain for this nonuniqueness, we introduce the condition that all the station time terms average to zero and then solve for the relative station time terms. This is easily done by introducing additional equations into the least squares problem. Later, the time terms for a set of close shallow earthquakes are used to estimate the absolute time terms.

To account for possible anisotropy and lateral velocity variations, the travel time equation is linearized with respect to slowness [Raitt et al., 1969].

$$t_{es} = \Delta_{es} \cdot S_0 + \tau_e(S_0) + \tau_s(S_0) + \left[\Delta_{es} + \frac{\partial \tau_s}{\partial S} + \frac{\partial \tau_e}{\partial S}\right]_{S=S_0} \cdot \delta S(x,y,\varphi) \quad (6)$$

or

$$t_{es} = \Delta_{es} \cdot S_0 + \tau_e(S_0) + \tau_s(S_0) + (\Delta_{es} - F_e - F_s) \cdot \delta S(x,y,\varphi) \quad (7)$$

where F_e and F_s are the event and station offset distances. They can be expressed as

$$F_e = \int_z^h \left[\frac{S}{(S(z)^2 - S^2)^{1/2}}\right] dz \quad (8)$$

$$F_s = \int_0^h \left[\frac{S}{(S(z)^2 - S^2)^{1/2}}\right] dz \quad (9)$$

The offset distance is the horizontal distance the ray travels between the Moho and the source or receiver while in the crust. Since the offset distances are a function of Pn velocity, crustal velocity, Moho depth, and event depth, none of which is known a priori, it is necessary to approximate these by an assumed constant offset distance "F." Then

$$t_{es} = \Delta_{es} \cdot S_0 + \tau_e(S_0) + \tau_s(S_0) + (\Delta_{es} - 2F) \cdot \delta S(x,y,\varphi) \quad (10)$$

For an anisotropic structure the slowness is expanded as [Backus, 1965]

$$\delta S(\varphi) = A \sin 2\varphi + B \cos 2\varphi + C \sin 4\varphi + D \cos 4\varphi \quad (11)$$

The travel time equation then becomes

$$t_{es} = \Delta_{es} \cdot S_0 + \tau_e(S_0) + \tau_s(S_0) + (\Delta_{es} - 2F) \cdot \delta S(\varphi) \qquad (12)$$

We can thus solve the least squares problem with four extra parameters to account for anisotropy.

To study regional velocity variations, a block-type time term inversion over the Southern California area is performed. The region is divided into a number of blocks (one half degree elements) and then the slowness for each block is estimated along with the time terms for the events and stations. For a ray traveling in such a medium the travel time is

$$t_{es} = \tau_e(S_e) + \tau_s(S_s) + \sum_{i=0}^{n} \Delta_i S_i \qquad (13)$$

where S_e is the Pn velocity at the event location, S_s is the Pn velocity at the station location, Δ_i is the horizontal distance traveled by the ray path in or above block i, and $S_i = 1/V_i$ is the slowness of block i.

We wish, however, to determine $\tau_e(S_0)$ and $\tau_s(S_0)$, not $\tau_e(S_e)$ and $\tau_s(S_s)$. Otherwise, we can not correctly compare the time terms to each other. Essentially, the time terms must be corrected for the effect of varying Pn velocity. To first order, the travel time equation is then

$$t_{es} = \tau_e(S_0) + \tau_s(S_0) + \sum_{i=0}^{n} \Delta_i S_i - F\delta S_e - F\delta S_s \qquad (14)$$

where δS_e and δS_s are the slowness perturbations from the mean slowness, $S_0 = 1/V_0$, at the event and station locations, respectively. Reexpressing this equation so that we solve for only the relevant parameters

$$t_{es} = \tau_e(S_0) + \tau_s(S_0) + \sum_{i=0}^{n} \Delta_i S_i - F\cdot(\delta S_e + S_0) - F\cdot(\delta S_s + S_0) + 2FS_0 \quad (15)$$

$$t_{es} = (\tau_e(S_0)+2FS_0) + \tau_s(S_0) + \; + \sum_{i=0}^{n} \Delta_i S_i - FS_e - FS_s \quad (16)$$

$$t_{es} = (\tau_e(S_0)+2FS_0) + \tau_s(S_0) + \sum_{i=0}^{n} \Delta_i' S_i \quad (17)$$

where $\Delta_i' = \begin{cases} \Delta_i \text{ if } i \neq e \text{ and } i \neq s \\ \Delta_i - F \text{ if } i = e \text{ or } i = s \end{cases}$

The Δ_i' represents the distance the ray travels along the Moho in each block. This definition accounts for the offset at the ends of the ray path. In tracing the rays across the grid, the starting and ending points are shifted by the offset distance. Because of this, (17) is actually more realistic than (13), which would have us improperly trace the ray to points on the mantle directly underneath the station and source. As before, the mean of the station time terms is set to zero. The equations are solved for the unknowns $(\tau_e(S_0)+2FS_0)$, $\tau_s(S_0)$, and the S_i . The mean Pn slowness in Southern California, S_0, can be found from the mean of the individual block slownesses that are determined. The station time terms can then be estimated if desired. The block model is easily extended to include gross anisotropy by using the form

$$t_{es} = (\tau_e(S_0)+2FS_0) + \tau_s + \sum_{i=0}^{n} \Delta_i' S_i + (\Delta_{es} - 2F)\cdot \delta S(\varphi) \quad (18)$$

In solving for the block slownesses, the least squares problem was damped. Trade-offs between grid elements, particularly the edge elements,

make this necessary if we want a coherent picture. This is because not all of the grid elements have adequate ray coverage to determine uniquely their slownesses. In most applications of damped least squares, the parameters are perturbations that are damped to zero. In the model used here we are not dealing with perturbations but actual values. For this case, the slowness elements are damped to the a priori value of 7.9 km/s. The time terms are not damped. If the linear system of equations is again expressed as $\mathbf{Ax} = \mathbf{t}$, the solution to this damped problem is given by solving the normal equation [Bierman, 1977]

$$(\mathbf{A}^T\mathbf{A} + k\,\mathbf{D})\mathbf{x} = \mathbf{A}^T\mathbf{t} + k\,\mathbf{D}\mathbf{b}_0 \tag{19}$$

Here $\mathbf{D}$ is a diagonal matrix with the diagonal elements corresponding to the slowness elements equal to one and equal to zero for the other parameters. The vector $\mathbf{b}_0$ contains the a priori slowness values in places corresponding to the slowness elements and zero for the other parameters. The damping constant is k.

The F test [Draper and Smith, 1966] can be used to test the statistical significance of adding new parameters to the model. The F ratio is given by

$$F = \frac{(\mathrm{RSS}_1 - \mathrm{RSS}_2)/(\mathrm{DOF}_1 - \mathrm{DOF}_2)}{(\mathrm{RSS}_2/\mathrm{DOF}_2)} \tag{20}$$

where RSS refers to the residual sum of squares and DOF refers to the number of degrees of freedom. The subscripts 1 and 2 refer to models without and with the extra parameters, respectively. If F is large, we reject the null hypothesis and accept the new terms as being different from zero.

The computed F ratio can be compared to tables for the F distribution with DOF_1–DOF_2 and DOF_2 degrees of freedom at the 99% confidence level.

Data Set

The Southern California Array for Research on Local Earthquakes and Teleseisms (SCARLET) has been digitally recording seismograms since 1977 [Johnson, 1979]. Over 200 stations have been used with as many as 160 recording simultaneously. During this period, arrival times for local earthquakes have been routinely collected and used for the location of local earthquakes. The data set in this study consists primarily of these routine arrival time picks. The data set collected by Lamanuzzi [1981] from this array was also used. A few of the larger events were retimed and relocated to assure a proper location and to make certain that Pn was timed out to the maximum possible distance. The relocations did not change appreciably from the original locations.

In order to obtain a quality data set, a travel time plot was made for all events greater than about magnitude 4.0 that were recorded by SCARLET. Events smaller than this do not generally record well in the Pn distance range. Earthquakes with "erratic" travel time plots were discarded. These were generally events with locations outside the array, badly mislocated events, or events with too few high-quality arrivals. Events from the Mammoth Lakes area were not used, since the locations are poor and the ray paths from Mammoth are affected by the Sierra Nevada root. A list of events used is given in Table 1 and is shown in Figure 2.

TABLE 1. Events Used in This Study

Date	Time,LT	Latitude	Longitude	Depth,km	Magnitude
Feb. 2, 1976	0004:57.1	34°44.20	112°27.80	8.0	4.7
April 4, 1976	1521:38.1	34°20.81	118°39.74	12.0	4.6
Aug. 12, 1977	0219:26.0	34°22.78	118°27.53	9.5	4.5
Sept. 9, 1977	1400:00.1	37°09.06	116°04.08	0.0	4.8
Sept. 24, 1977	2128:24.3	34°27.76	118°24.58	4.9	4.2
Oct.. 4, 1977	1451:44.0	31°50.39	114°32.60	5.0	4.0
Nov. 14, 1977	0205:48.5	32°49.45	115°28.21	5.4	4.2
Nov. 14, 1977	0536:55.9	32°48.72	115°28.16	5.0	4.1
Nov. 14, 1977	1220:20.1	32°48.99	115°27.80	10.1	4.3
Feb. 13, 1978	2152:60.9	37°02.77	116°00.85	4.9	3.7
Feb. 23, 1978	1700:00.6	37°04.74	116°02.27	4.9	4.4
March 11, 1978	2357:48.8	32°24.90	115°08.73	6.0	4.4
March 12, 1978	0030:17.6	32°17.41	115°07.42	6.0	4.4
March 12, 1978	1842:24.8	32°17.01	115°07.26	6.0	4.5
March 23, 1978	1629:59.2	37°07.49	115°59.31	1.0	4.3
May 5, 1978	2103:15.8	32°12.68	115°18.21	6.0	4.5
May 5, 1978	2242:08.9	32°14.96	115°18.95	6.0	3.8
May 7, 1978	0241:40.1	32°15.21	115°18.76	6.0	3.8
May 9, 1978	0110:07.7	31°00.63	116°49.24	1.6	3.6
May 23, 1978	0916:50.8	33°54.33	119°09.94	6.0	3.9
June 5, 1978	1602:63.9	33°25.21	116°41.88	11.9	4.2
June 6, 1978	0421:31.6	35°02.08	119°08.23	1.7	4.3
Aug. 13, 1978	2254:52.8	34°23.92	119°40.88	12.6	5.1
Aug. 19, 1978	0931:05.7	32°18.15	116°52.85	19.8	3.8
Aug. 29, 1978	1802:13.8	31°29.76	115°27.36	10.1	3.5
Nov. 20, 1978	0654:69.5	34°09.06	116°58.34	6.0	4.2
Jan. 1, 1979	2314:38.8	33°56.91	118°41.85	12.5	5.0
Feb. 12, 1979	0448:42.3	33°27.47	116°26.05	3.8	4.2
March 15, 1979	2017:49.8	34°18.56	116°26.42	0.1	4.9
March 15, 1979	2106:76.5	34°19.64	116°26.69	0.6	5.2
March 15, 1979	2133:85.5	34°20.91	116°27.17	0.0	4.5
March 15, 1979	2307:58.1	34°19.79	116°26.57	5.0	4.8
March 16, 1979	1736:59.0	34°19.74	116°23.87	5.0	4.0
March 18, 1979	2252:62.6	34°13.81	116°21.80	3.4	4.2
March 31, 1979	0016:08.5	34°18.15	116°29.93	0.1	4.2
June 14, 1979	0739:28.2	35°43.76	118°01.40	5.0	4.6
June 29, 1979	0553:20.4	34°14.80	116°53.90	9.2	4.6
June 30, 1979	0034:11.5	34°14.62	116°53.50	10.1	4.9
June 30, 1979	0703:52.8	34°14.98	116°53.76	10.0	4.5
July 13, 1979	0225:63.5	34°15.41	116°26.13	5.0	4.0
Aug. 6, 1979	1705:22.7	37°06.12	121°30.80	5.0	5.9
Aug. 22, 1979	0201:36.3	33°42.06	116°50.20	5.0	4.1
Oct. 15, 1979	2316:54.2	32°38.61	115°18.53	9.9	6.6
Oct. 16, 1979	0549:10.1	32°56.98	115°32.38	14.7	5.1
Oct. 16, 1979	0658:42.7	33°00.82	115°33.31	12.8	5.5

Oct.	16, 1979	0723:24.2	32°53.92	115°31.12	4.4	4.2
Oct.	16, 1979	1201:45.6	32°52.38	115°30.43	14.4	4.0
Oct.	16, 1979	2316:32.2	33°01.12	115°30.23	15.2	4.9
Dec	12, 1979	2137:40.9	32°12.12	116°13.73	5.0	4.0
Feb.	2, 1980	1047:00.0	33°29.83	116°85.58	14.2	5.5
April	19, 1981	0902:10.6	35°49.59	117°46.20	8.5	4.2
April	19, 1981	0919:57.1	35°49.89	117°46.51	11.3	4.0
April	25, 1981	0211:55.3	33°06.60	115°37.60	4.8	4.1
April	26, 1981	1209:28.4	33°05.91	115°37.90	3.7	5.7
June	22, 1981	0457:47.2	35°05.71	118°31.13	5.0	4.0
July	11, 1981	2150:29.4	32°37.50	118°00.55	5.0	4.3
July	24, 1981	1138:46.1	31°46.94	116°20.42	15.0	4.6
Sept.	4, 1981	1550:49.4	33°40.54	119°06.25	7.2	5.2
Oct.	23, 1981	1728:15.8	33°37.57	119°07.21	7.2	4.6
Oct.	23, 1981	1915:51.3	33°37.14	119°01.18	7.2	4.6
Nov.	10, 1981	2234:35.5	35°01.10	119°08.43	3.1	4.5
Nov.	10, 1981	2237:05.0	35°00.72	119°10.75	9.4	4.2
March	1, 1982	0310:23.3	35°46.68	117°44.81	3.8	4.2
March	7, 1982	2049:72.7	35°45.60	117°44.81	2.1	4.3
March	8, 1982	1442:46.0	35°45.03	117°43.79	4.4	4.0

After the bad events were discarded, all the travel time sections were then reexamined for outliers in the data. Picks which were 1 s or more outside the body of the data were discarded. This amounts to perhaps 4% of the data. Only events with 10 or more arrivals were used.

All data being used were assigned qualities ranging from near perfect to useless when picked. Zero indicates the highest-quality pick, good to the digitization interval of 0.02 s. Quality 1, 2, and 3 arrivals have standard errors of 0.1, 0.2, and 0.5 s, respectively. Quality 4 arrivals have larger standard errors and were not used at all. On the basis of these errors, a weighting of 400, 100, 25, and 4 was used. A composite travel time plot of all these events is in Figure 3. We used only data recorded at distances over 150 km, where Pn is almost always the first arrival.

Results

The time term method yields a Pn velocity of 7.9 ± 0.1 km/s. This is an averaged velocity for the Southern California region. Individual refraction profiles can have values quite different from this.

Delays found with the time term method are shown in Figure 4. The relative delays span well over 1 s indicating more than 10 km of relief in the crust-mantle boundary. In general, the delays are smaller in the southeastern portion of the array. The largest delays are found in the Ventura Basin area. In constructing this figure, only stations recording more than five arrivals are plotted. The delays were all corrected for elevation by assuming a 5.5 km/s surface velocity. The estimated error of the delays is about 0.1 s. The highest-quality arrivals have standard errors of 0.2 s. This error can be explained by event mislocations of 2 km.

In all inversions explicitly involving the offset parameter (those involving velocity perturbations), an offset distance of 32 km was used. This value was found by trial and error to minimize the residual square. The inversions are not terribly sensitive to this parameter. Note that this offset represents in some sense, the average of the offset for all events and stations. Since the events occur at depth, this value is less than the offsets for just the stations.

To demonstrate the effectiveness of the F test and the importance of the station time terms, the time term model was run without the station time terms. The travel time equation is then

$$t_{es} = \Delta_{es} \cdot S + \tau_e \qquad (21)$$

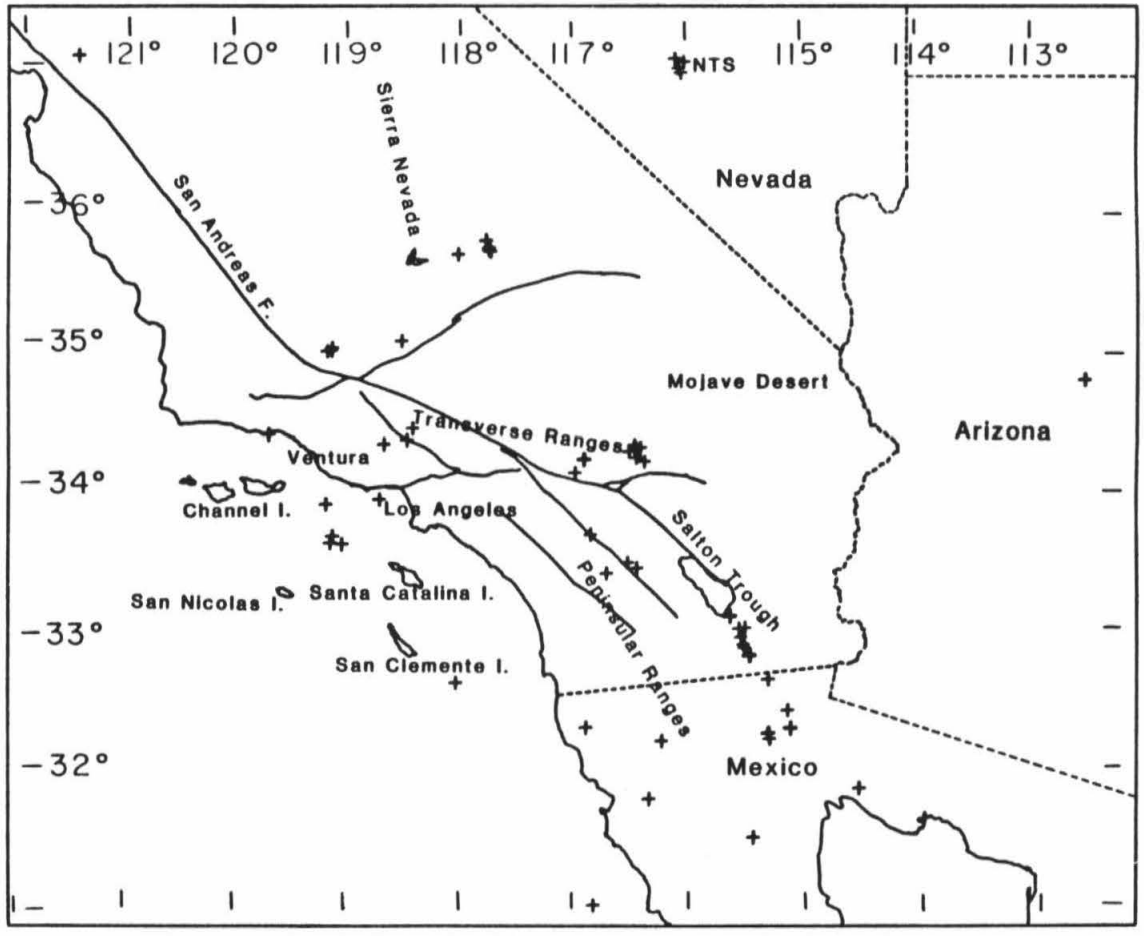

Figure 2. Base map of southern California showing all events used in this study.

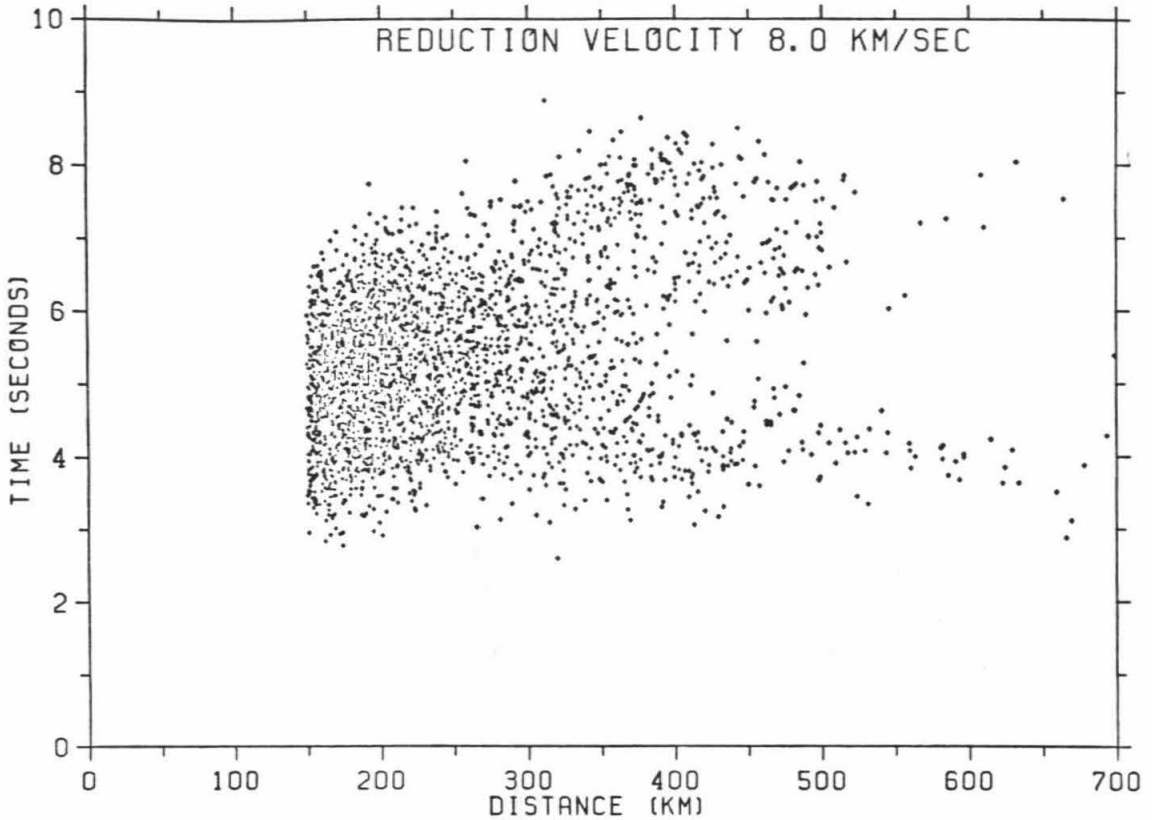

Figure 3. Composite travel time plot of all data used in this study.

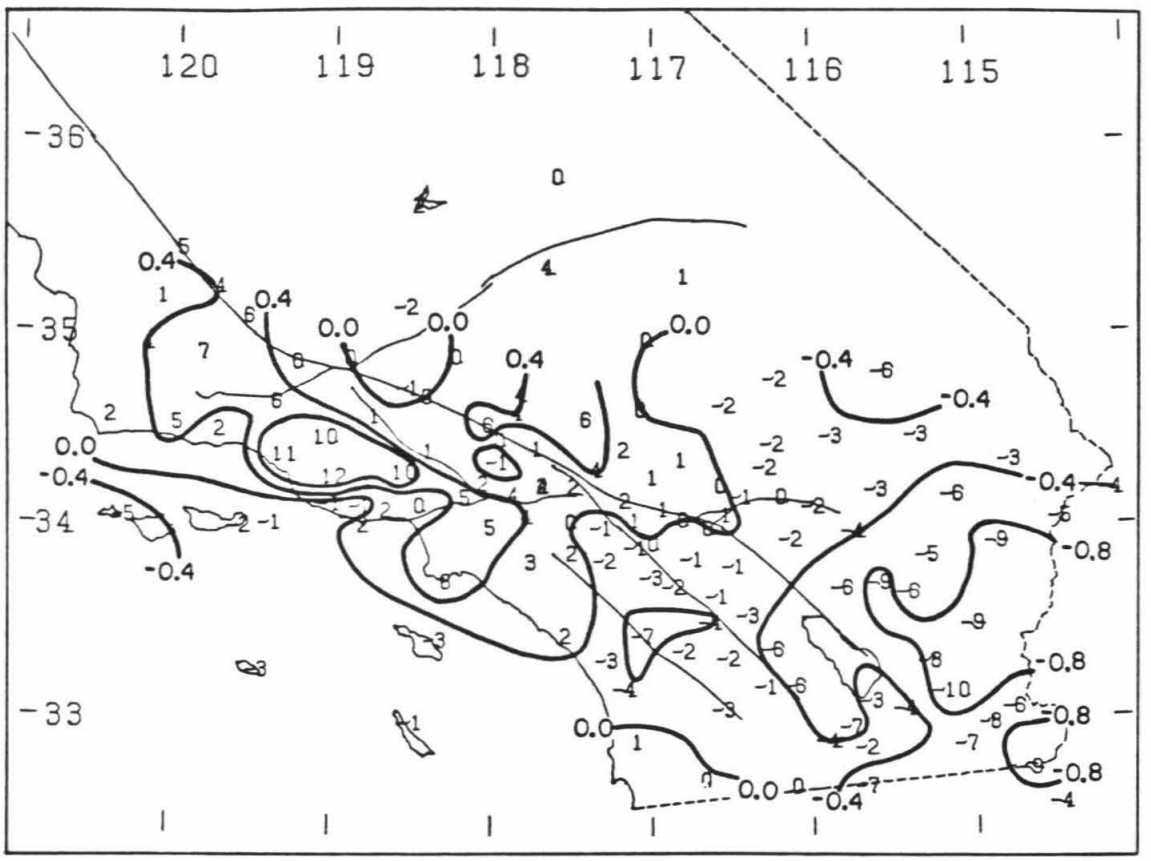

Figure 4. Relative time term surface for distances greater than 150 km. Numbers in tenths of seconds. Elevation corrections have been applied. The time terms are roughly proportional to relative crustal thicknesses.

The omission of the station time terms causes the variances to increase to 0.11 s^2 from 0.05 s^2 and the F test verifies that this is statistically significant (Table 2). Figure 5 shows the azimuthal distribution of residuals for the complete model.

TABLE 2. Analysis of Variance Table Illustrating the Effect of the Station Time Terms

Model	RSS	DOF	Variance	F
$\frac{\Delta_{es}}{V} + \tau_e + \tau_s$	128.5	2555	0.050	15.4
$\frac{\Delta_{es}}{V} + \tau_e$	296.1	2773	0.107	

$F_{218,\infty}(99\%) = 1.0$. RSS is the residual sum of squares, DOF is the number of degrees of freedom, and F is the F ratio statistic. The estimated variance for the highest-quality arrivals is shown. The significance of the station time terms is indicated by the 50% reduction in variance as well as the F ratio.

The azimuthal variations of the residuals on Figure 5 are of interest. The full anisotropic model with terms of 2φ and 4φ (from $\delta V = A \cos 2\varphi + B \sin 2\varphi + C \cos 4\varphi + D \sin 4\varphi$) was tested. The F test demonstrates the anisotropy to be significant (Table 3). The 2φ terms indicate an anisotropic value of 0.15 km/s ($\sim$1.8%) with the fast axis striking N75° W. The 4φ value contributes about 0.05 km/s to the total anisotropy, and the mean velocity remains the same as in the previous inversion. The delay map that includes anisotropy is shown in Figure 6. By use of (10) we can compute $\delta S(\varphi)$ for each arrival by using the time terms and velocity computed from the anisotropic model. This is converted to δV by

$$\delta V(\varphi) = -\delta S(\varphi) / S_0^2 \qquad (22)$$

and plotted in Figure 7. This figure represents the computed azimuthal velocity variations plus the residual noise.

TABLE 3. Analysis of Variance Table That Demonstrates the Effect of Adding Anisotropy Which Varies as a Function of 2φ and 4φ

Model	RSS	DOF	Variance	F
2φ and 4φ	95.0	2551	0.037	224
$\frac{\Delta_{es}}{V} + \tau_e + \tau_s$	128.5	2555	0.050	

$F_{4,\infty}(99\%) = 3.3$. The F ratio indicates that anisotropy cannot be ruled out by this data set. The symbols are the same as for Table 2.

In order to assess fully the azimuthal velocity variations, several inversions were run allowing the velocity to vary as $n\varphi$. Terms of orders higher than 5φ are found by the F test not to be significantly different from zero (Table 4). The 2φ term makes the largest difference. The 3φ and 4φ terms have values near 0.05 km/s, and the 5φ term has less. Table 3 lists an analysis of variance table for these terms. It is disturbing that the 3φ term, which is not due to anisotropy, is only slightly less important than the 4φ term. In view of this, it is difficult to interpret the 4φ in terms of anisotropy.

To investigate lateral Pn velocity variations, the array was divided into 96 elements with one half degree of latitude or longitude on a side. Without damping, the velocity variations and their estimate errors are large, particularly where ray coverage is sparse. To stabilize this, the element velocities are damped to 7.9 km/s, and only grid elements containing more than 100 rays are plotted.

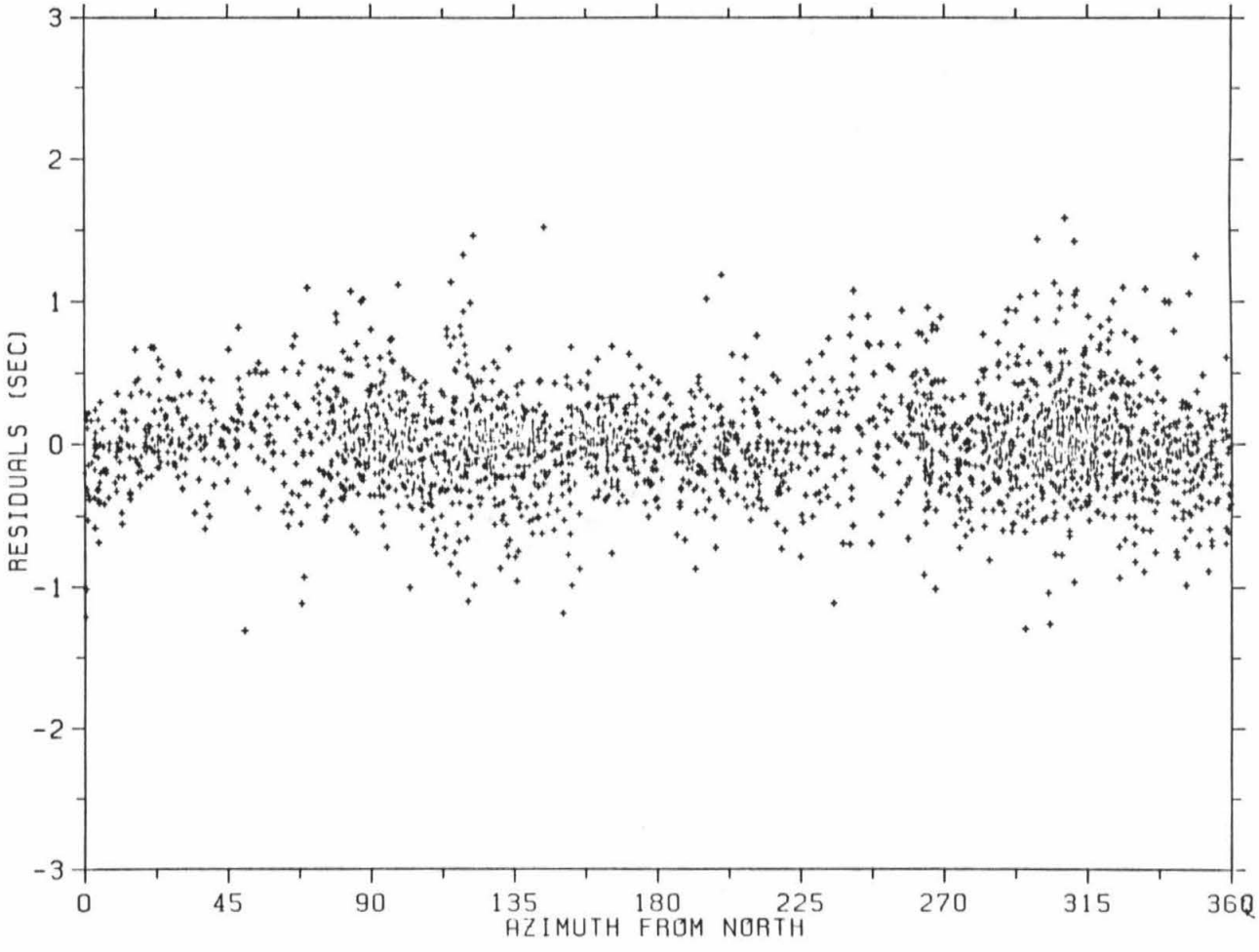

Figure 5. Residuals for the complete time term model $t_{es} = (\Delta_{es} / V) + \tau_e + \tau_s$. Note the apparent variation with azimuth.

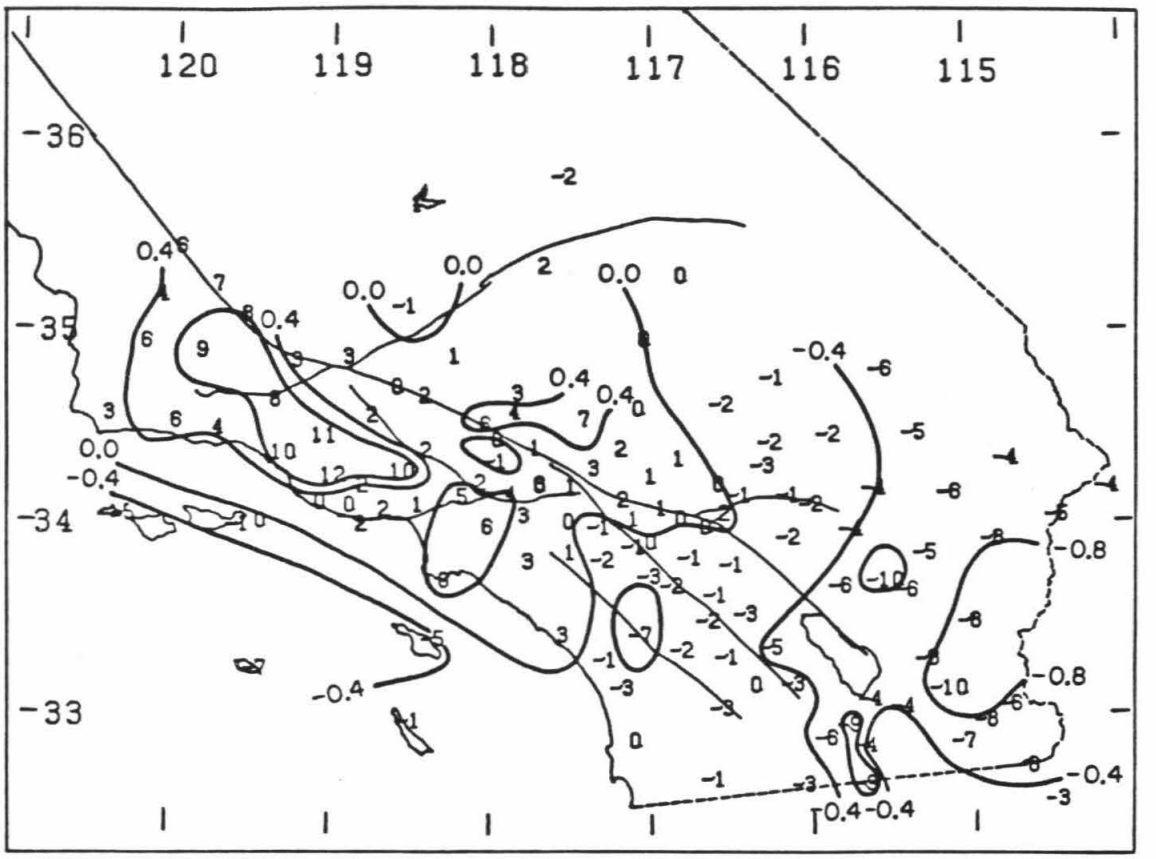

Figure 6. Relative time term surface for the fully anisotropic model (both 2φ and 4φ azimuthal variations.) Numbers in tenths of seconds. Note that this surface has changed very little from Figure 4.

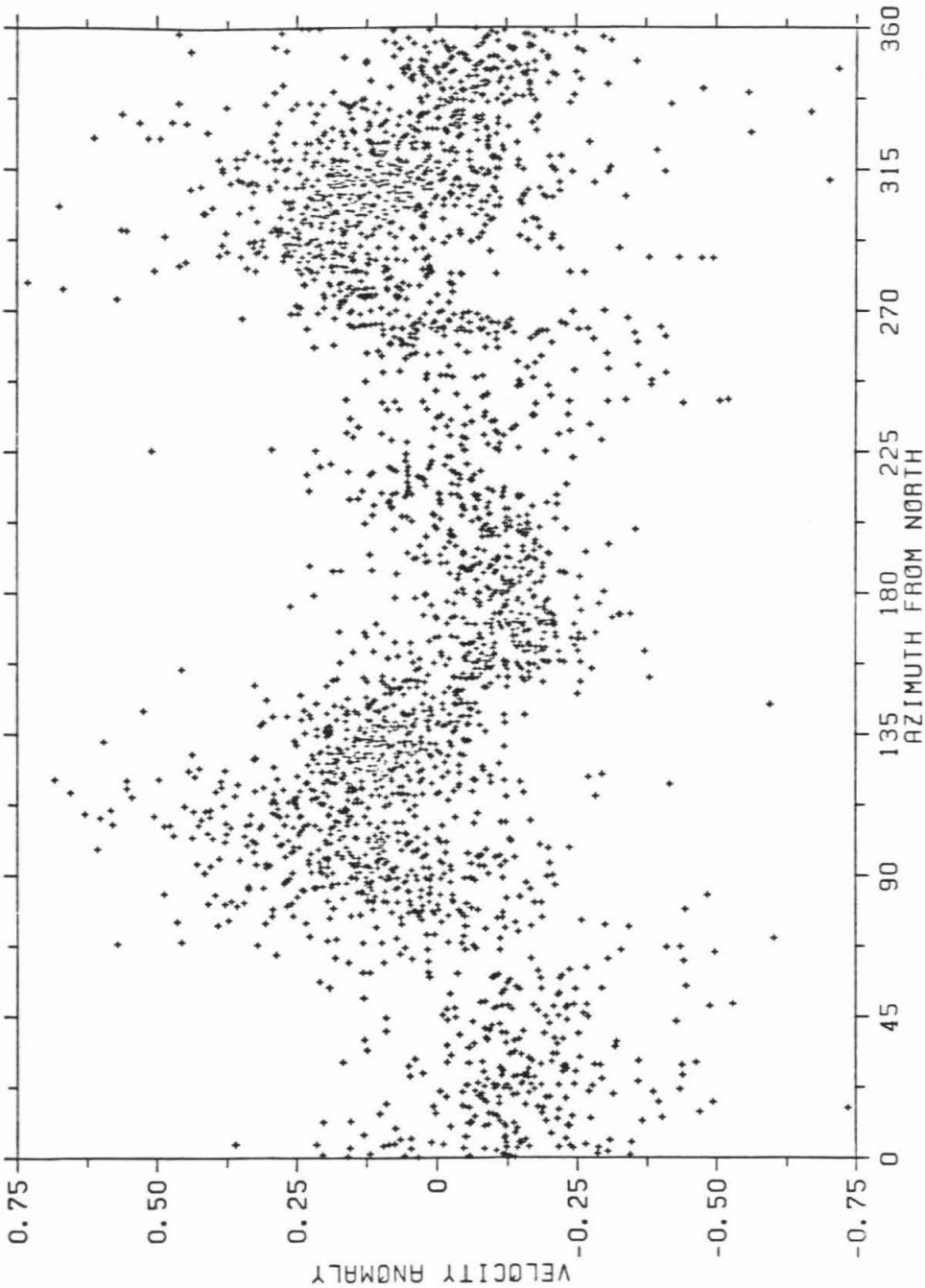

Figure 7. Azimuthal velocity deviations estimated in the anisotropic model.

TABLE 4. Analysis of Variance Table That Investigates the Azimuthal Velocity Variations

Model	RSS	DOF	Variance	F
φ	127.5	2553	0.050	9.5
2φ	101.2	2553	0.040	344.8
3φ	116.7	2553	0.046	128.2
4φ	116.2	2553	0.046	135.1
5φ	124.6	2553	0.049	39.7
6φ	128.1	2553	0.050	3.4*
7φ	128.5	2553	0.050	0.9*
8φ	128.2	2553	0.050	2.8*
$\frac{\Delta_{es}}{V} + \tau_e + \tau_s$	128.5	2551	0.050	

$F_{2,\infty}(99\%) = 4.6$. The 2φ terms, indicating anisotropy, are the most important. The symbols are the same as for Table 2.

* Insignificant terms.

In Figure 8 the regional variation in apparent Pn velocities is shown. Velocities range from a low of 7.7 km/s to a high of 8.3 km/s. The slowest areas are in the middle of the array and on the eastern edge. The fastest areas are the offshore area, the Salton Sea, and the northern Mojave.

The F test (Table 5) demonstrates that these variations are significant. All estimated standard errors are under 0.1 km/s. Figure 9 shows the delay map associated with these velocities. Note that although the time terms have traded off with the new velocity parameters, the overall delay pattern remains the same. The residuals have, of course, decreased, but the variations with azimuth still remain.

Finally, a full model containing all time terms, lateral velocity variations, and regional anisotropy (2φ terms only) was tested. The delay map for this

TABLE 5. Analysis of Variance Table That Shows the Effect of Allowing Velocity to Vary Laterally

Model	RSS	DOF	Variance	F
96 blocks	79.3	2460	0.033	16.0
$\frac{\Delta_{es}}{V} + \tau_e + \tau_s$	128.5	2555	0.050	

$F_{96,\infty}(99\%) = 1.4$. The inclusion of the velocity variations makes a considerable improvement. The symbols are the same as for Table 2.

inversion is in Figure 10; the velocity variations are in Figure 11. Again the F test shows that the mean anisotropy found is significantly different from zero. Further inversions demonstrate that the higher-order terms (4φ and up) are much less significant when we allow lateral velocity variations (Table 6). When both 2φ and 4φ terms are used, the magnitude of the 4φ term drops to less than 0.01 km/s and the F ratio drops to nearly the critical value (Table 7). Thus the 4φ terms are greatly influenced by the lateral velocity distribution. The value of anisotropy remains at 0.15 km/s with the same strike as before.

TABLE 6. Analysis of Variance Table Demonstrating the Added Effects of Allowing Azimuthal Velocity Variations in Addition to Lateral Velocity Variations

Model	RSS	DOF	Variance	F
96 blocks and 2φ	61.6	2458	0.025	354.0
96 blocks and 3φ	76.4	2458	0.031	45.7
96 blocks and 4φ	76.8	2458	0.031	39.9
96 blocks and 5φ	78.4	2458	0.032	12.7
96 blocks	79.3	2460	0.032	

$F_{2,\infty}(99\%) = 4.6$. The F statistic again indicates that we cannot exclude anisotropy from this data set. The symbols are the same as for Table 2.

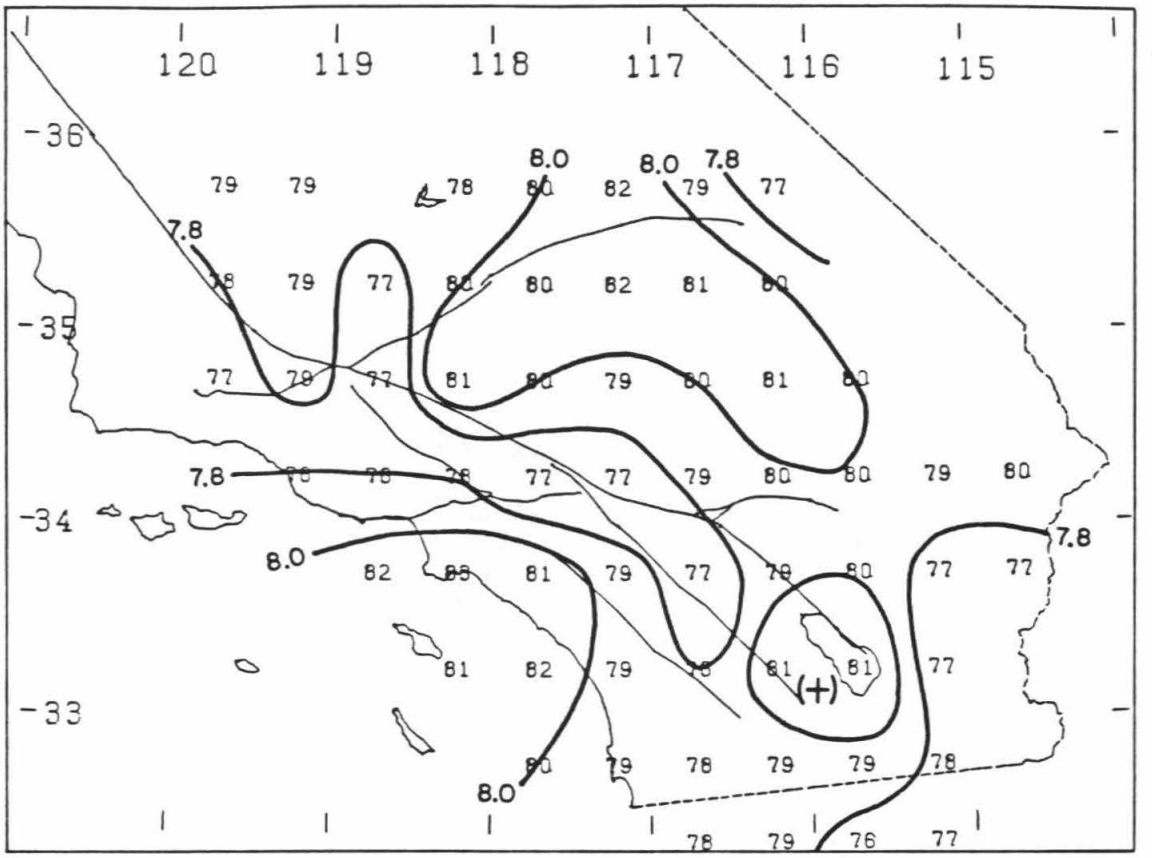

Figure 8. Lateral Pn velocity variations in Southern California from equation (18).

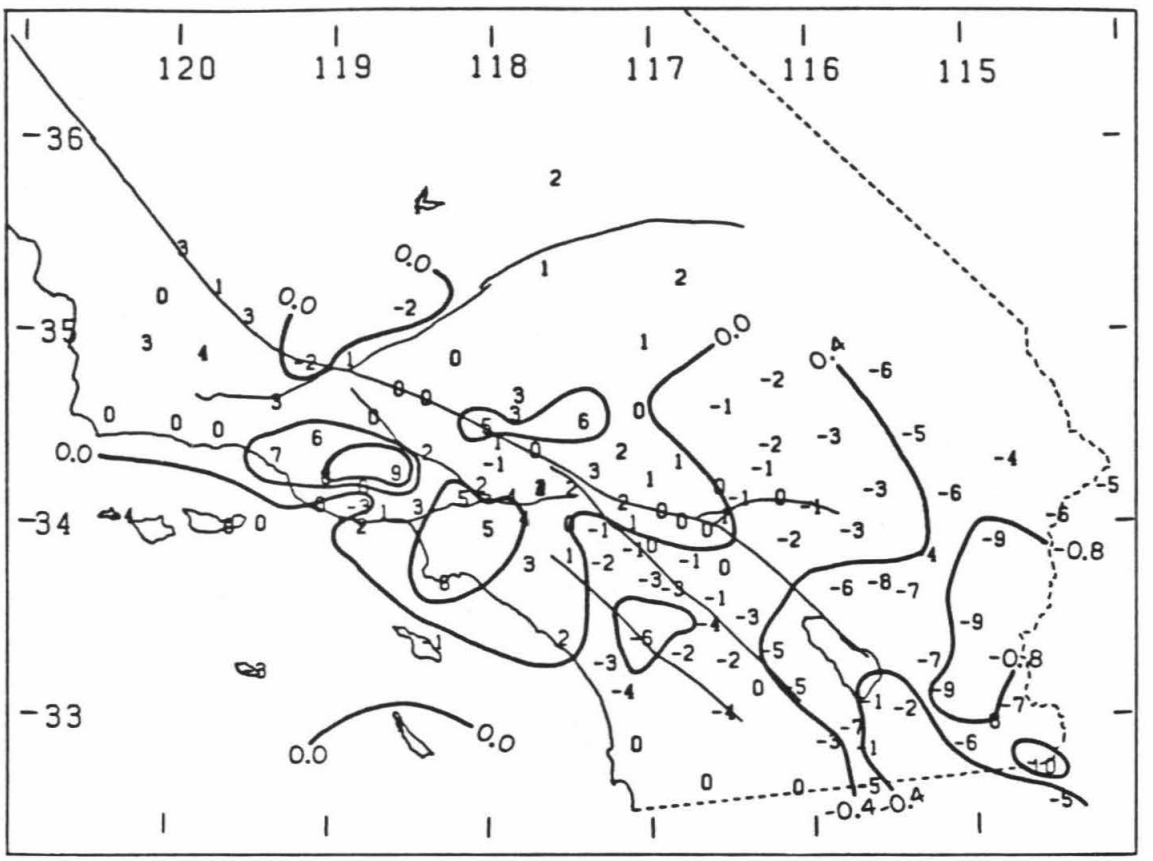

Figure 9. Time term surface of the model (equation (18)), which allows for lateral velocity variations. The time terms are roughly proportional to the relative crustal thicknesses.

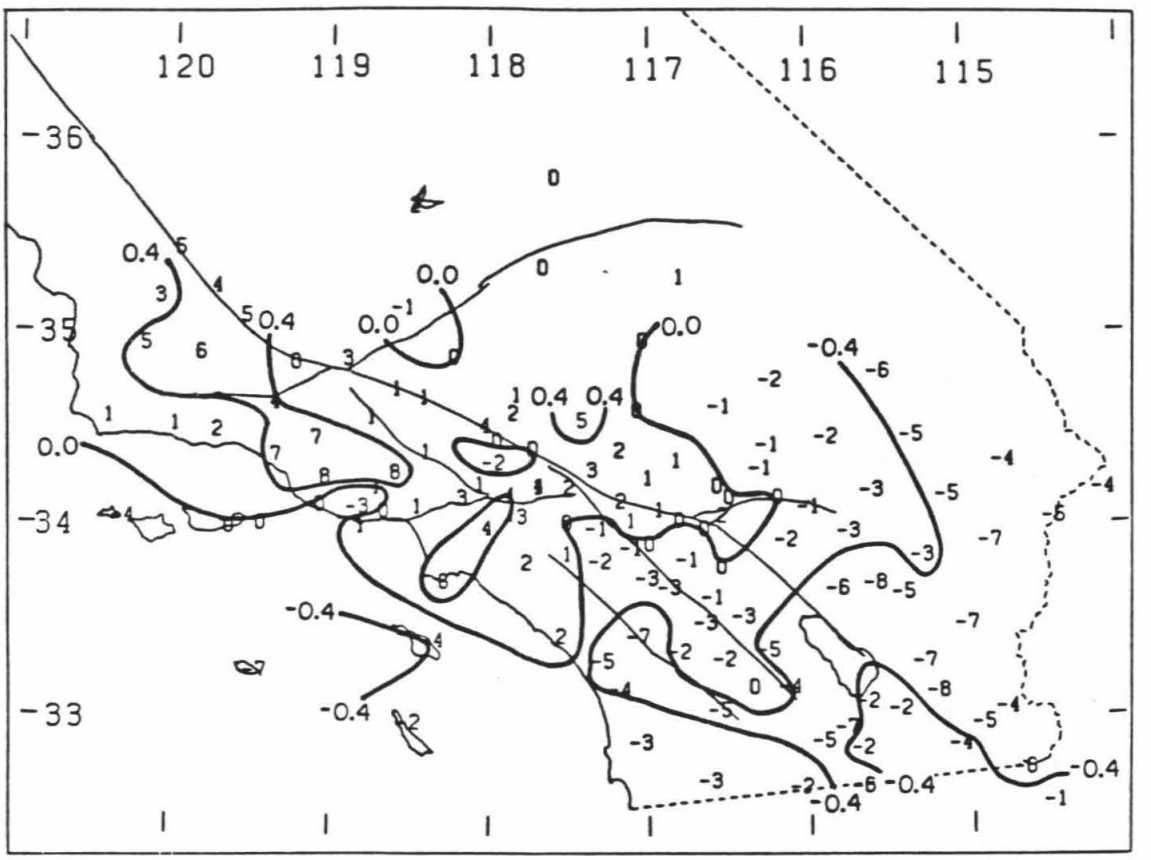

Figure 10. Time term surface of the model which includes both block velocity variations and anisotropy. Elevation corrections have been applied. The time terms are roughly proportional to relative crustal thicknesses. Numbers in tenths of seconds.

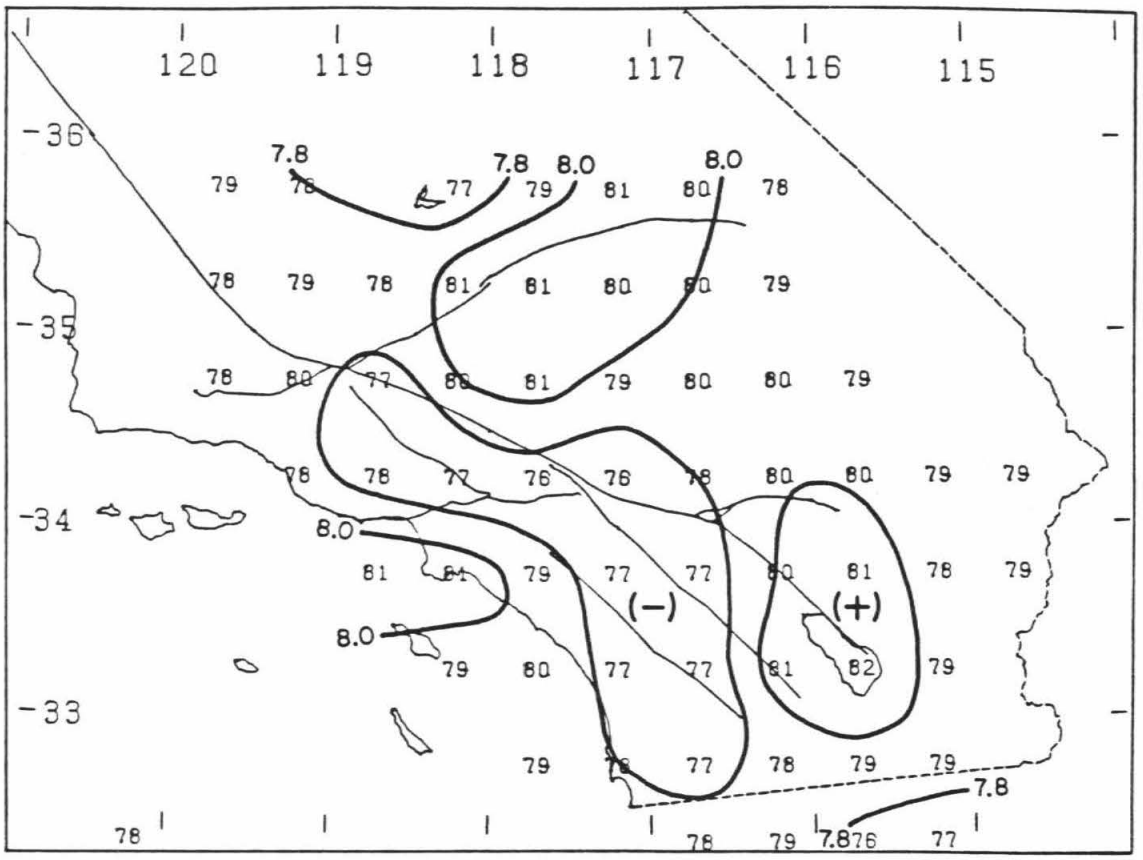

Figure 11. Velocity structure for model including anisotropy. Numbers in tenths of kilometers per second.

TABLE 7. Analysis of Variance Table Showing a Low F Value for the 4φ Anisotropy Terms

Model	RSS	DOF	Variance	F
96 blocks, 2φ and 4φ	60.8	2456	0.025	16.0
96 blocks and 2φ	61.6	2458	0.025	

$F_{2,\infty}(99\%) = 4.6$. This term is then very nearly equal to zero. The symbols are the same as for Table 2.

It is important to note that no matter how much the model is extended to include the effects of velocity deviations and anisotropy, the delay time maps (Figures 4, 6, 9, and 10) do not change drastically. This demonstrates the stability of the basic time term method. Comparison of the lateral velocity variations with and without anisotropy (Figures 8 and 11) shows some disparity but the gross pattern of highs and lows seems fairly stable. Velocities on the edge of the array are particularly influenced by the inclusion of anisotropy due to a poor azimuthal distribution of rays. Lateral velocity variations are much more difficult to determine than are the crustal delays. Figure 12 is the azimuthal velocity variation found.

The station time terms only give information on relative Moho depths. To ascertain absolute Moho depths, we must use the event time terms. It would be preferable to use well-located quarry blasts, but these are not widely enough recorded at Pn distances to give a good estimate of their time terms. The Nevada Test Site blasts used in this study have anomalously large delays (7 s) and so these were not used either. Six events that occurred in the Homestead Valley area (34.3° N, 116.4° W) were chosen as references because of their extremely shallow depths (0-5 km) and their central location. The

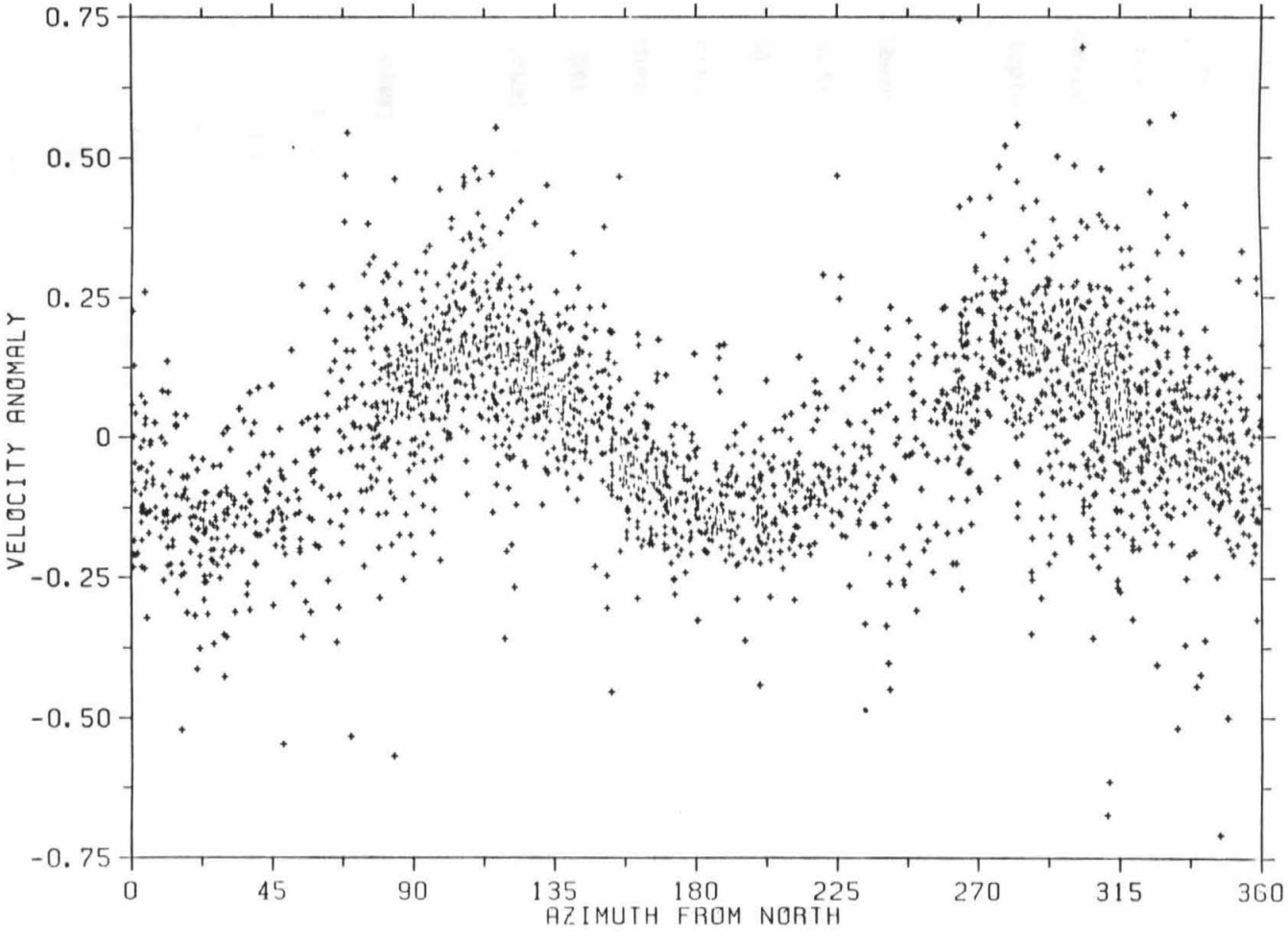

Figure 12. The azimuthal velocity variation found in the final model.

event delays were adjusted for depth and added to the estimated station delay at Homestead Valley (0.0 s). This gives a total two-way travel time at Homestead Valley of 5.5 ± 0.6 s. For a mean crustal velocity of 6.3 km/s this provides an estimate of crustal thickness of 29 ± 3 km. Note that the depth deviations found in this study will be much more accurate than the absolute depth.

The principal results of this study are the estimated delays. To interpret them in terms of crustal thickness, we must know the lateral velocity changes in the crust. For a constant delay time, thickness variations can be masked by velocity variations in slower upper crustal material or the faster lower crustal material. For consistency with the absolute depth calibration, the mean crustal velocity of 6.3 km/s has been used. One second of delay time then corresponds to 10.4 km of crustal thickening or a change in the mean crustal velocity of 0.8 km/s.

Interpretation

Variations in delay time represent both crustal velocity variations and Moho topography. Two examples of the former are the Ventura and Los Angeles basins, where positive anomalies of up to 1 s exist. Assuming a sediment velocity of 4.5 km/s and an upper crustal velocity of 6.0 km/s, this indicates basin depths around 12 km, in agreement with the known geology. Five kilometers of 4 km/s sediments in the Imperial Valley will add about 1/2 s to stations southeast of the Salton Sea [Fuis et al., 1982]. Also, station CFL in the San Gabriel Mountains seems out of place with its early arrival time. This

could be due to the presence of faster granitic rocks in the San Gabriel Mountains. Two areas where velocities higher than the 6.3 km/s used here are observed are the western Transverse Ranges (Hadley, 1978) and the Peninsular Ranges (Hadley, 1978; Nava and Brune, 1982; Pechmann, 1983). If we were to assume a 6.5 km/s mean crustal velocity there, instead of 6.3 km/s, the Moho would be 2.5 km deeper in these areas.

In Figure 13 an estimate of crustal thickness is contoured from Figure 10. Attempts to compensate for the presence of the Los Angeles Basin, Ventura Basin and the Salton Trough are made by smoothing the contours over these areas. No compensation for regional velocity differences was made since differences are not well-delineated spatially. Attempts to make more accurate crustal corrections have been made in the past. For example, Raikes [1980] gives teleseismic sediment delays of up to 0.75 s for 23 stations. The array is much larger now, and data for systematic estimation of crustal corrections are not available for all stations. Also, recalling that the Pn rays emerge at angles near 50° from the vertical, the subsurface geology must be known for some distance around each station. Rather than risk overcorrecting the data, only the most obvious corrections were made.

The large low in the delay time map along the California-Arizona border region (southern Basin and Range) corresponds to a thin crust. The early arrivals here are best explained by near 10 km of crustal thinning. Attributing these early arrivals entirely to velocity structure would require an absurd mean crustal velocity of 7.2 km/s. Warren [1969], using Pn data from central Arizona, found that the crust thinned from 40 km under the Colorado Plateau

to 21 km near Gila Bend in southwestern Arizona. Thus an area of thin crust is centered along the California-Arizona border region extending approximately from the San Andreas Fault in the Imperial Valley into Arizona. This area of thin crust corresponds well with the detachment faulting observed in the metamorphic core complexes along the Colorado River [Davis et al., 1980]. This detachment faulting is often explained in terms of crustal stretching and uplift. The presence of thin crust supports a connection between detachment faulting and crustal thickness in this area.

In Figure 14 the Bouguer gravity anomaly for Southern California is shown [Oliver, 1982]. The 60+ mGal gravity difference between the Channel Islands and the mainland supports the almost 5 km of crustal thinning to these islands. On the crustal thickness map, Santa Catalina and San Clemente islands have crustal thicknesses near 26 km with more thinning toward San Nicholas Island. Shor and Raitt [1958] have obtained similar results. Large gradients are evident in both the delays and the gravity along the Ventura coast. This suggests an abrupt change in structure there from the thick sediments of the Ventura Basin to the offshore crust.

To the north, under the southern Coast Ranges, thick crust of 34 km exists. This might be overestimated by 1 or 2 km in this area due to low crustal velocities. For example, Pechmann [1983] finds a velocity of 6.2 km/s for the arrivals here, and Healy [1963] finds a velocity of 6.1 km/s. However, Hadley [1978], has observed arrivals with apparent Pg velocities of 6.36 km/s in this area. Gravity is consistent with a 34-km thickness.

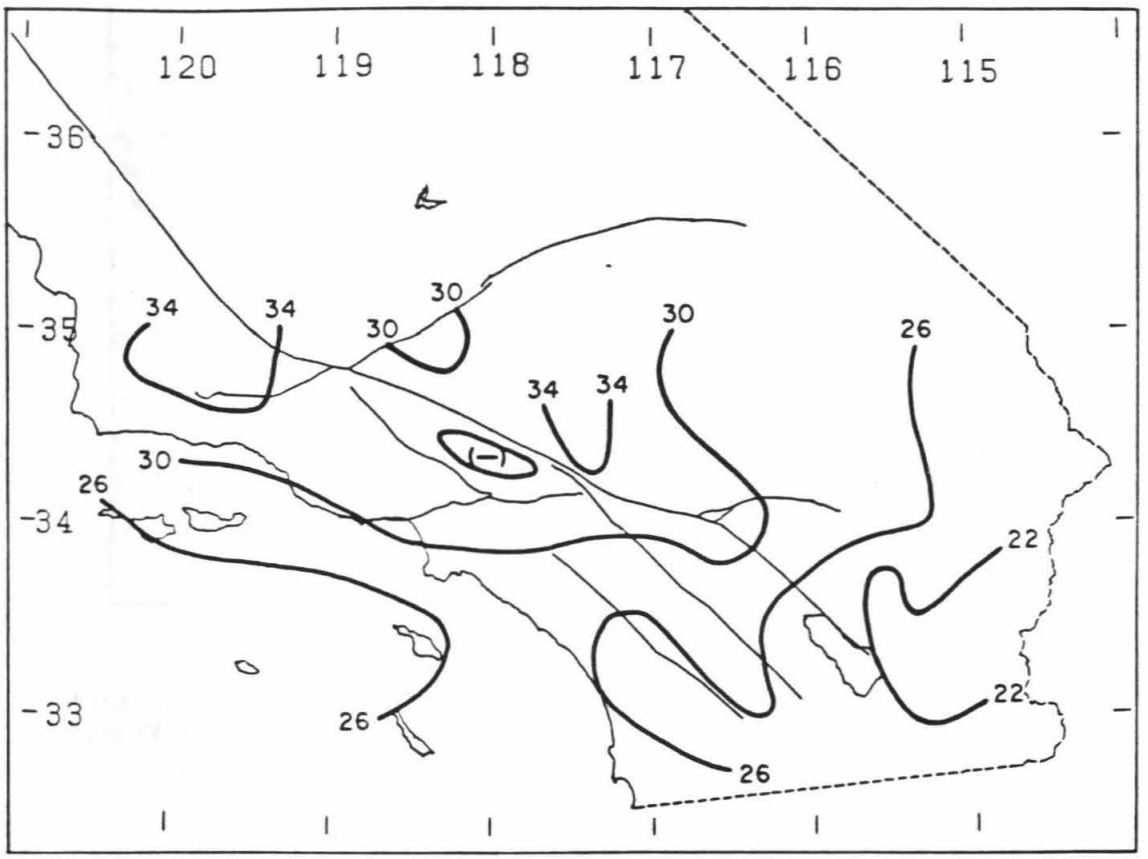

Figure 13. An estimate of crustal thickness in the Southern California region based on a mean crustal velocity of 6.3 km/s. The estimate attempts to account for sediments in the Ventura Basin, the Los Angeles Basin, and the Salton Trough by smoothing the contours over those areas. High crustal velocities in the Peninsular Ranges and the Transverse Ranges could cause these areas to be a few kilometers thicker than shown.

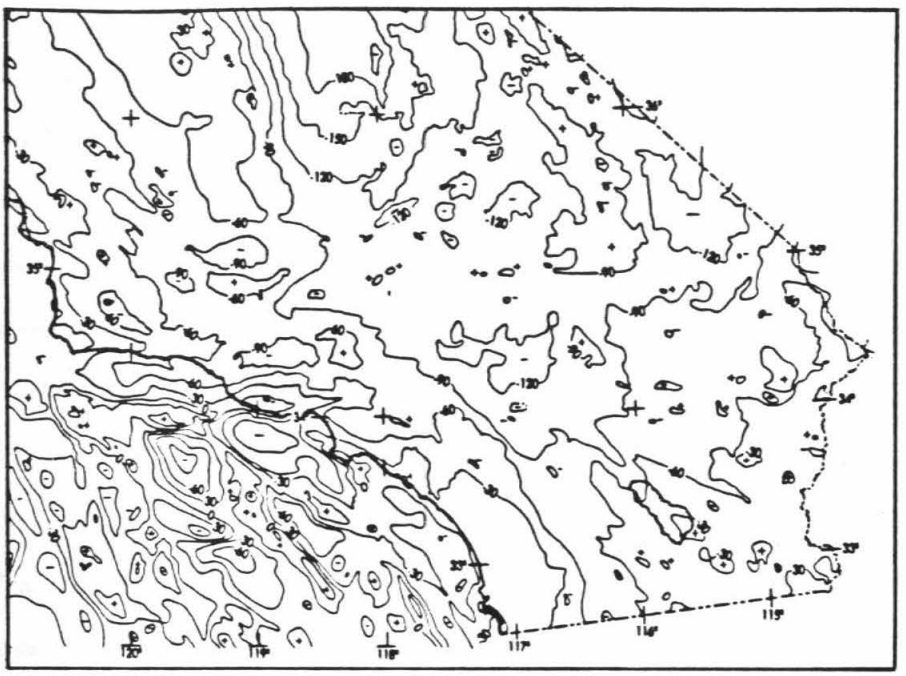

Figure 14. Bouguer anomaly gravity map of Southern California, modified from *Oliver et al.* [1982].

The Salton Trough presents some disagreement between gravity and the computed Moho depth. Gravity increases from -70 mGal in the Peninsular Ranges to a maximum of -30 mGal in the Salton Trough and back to values of -50 mGal in Arizona. This has been traditionally interpreted as evidence for a local Moho anticline under the Salton Trough [Elders et al., 1972]. This study finds that the crust thins from average depths of 26 km or more under the Peninsular Ranges to 22 km under the Salton Trough and to even less near Arizona. Hadley [1978] has an unreversed Pn profile for the northern Salton Trough which gives a crustal thickness of 20 km, in reasonable agreement with this study. To explain the gravity, without a Moho anticline, requires dense upper crustal material. Fuis et al. [1982] find such rocks in their refraction study of the Imperial Valley. They infer high-density intrusive rocks along the axis of the valley. The thinner crust in the southeastern Mojave contributes to high gravity values of -50 mGal there.

Seismic refraction profiles carried out by Roller and Healy [1963] and Healy [1963] allow a comparison with the results presented here. A profile between Santa Monica Bay (near Los Angeles) and Lake Mead [Healy, 1963] is interpreted to give a 29-km crust at Santa Monica, 36 km under the Transverse Ranges, 26 km in the Mojave, and 30 km at Lake Mead. Another profile [Healy, 1963] from Santa Monica north to San Francisco yields a crustal thickness of 35 km at Santa Monica thinning to 23 km northward. In view of the large surface delays found near Santa Monica, their thickness there is probably overestimated. The thickness for the Transverse Ranges is deduced from reflections and, as Roller and Healy [1963] state, is not very accurate. It

too, is probably overestimated due to surface delays. The delay map (Figure 10) shows thicker crust north of Santa Monica, indicating that the thinning must occur north of the array.

With the time term method, raypaths to a given station form a cone from the mantle that is over 80 km in its basal diameter. The delay time computed represents the mean delay over this cone. Thus, small features such as mountain roots will be spread out by an extra 40 km in the delay time map. Lamanuzzi [1981] demonstrates that the San Bernardino Mountains (eastern Transverse Ranges) have a 3- to 8-km root. He does this by examining Pn residuals from different azimuths and observing the shadow of the root precessing around the mountain range. The only indication of a root in the delay map (Figure 10) is the eastward swing of the 0.0-s contour. The root is probably at the lower end of Lamanuzzi's thickness range. The -120-mGal anomaly centered at 34.3° N, and 117.0° W is due to this mountain root. The San Gabriel Mountains (western Transverse Ranges) are anomalously early, indicating that no root is present.

The Peninsular Ranges seem to possess, at most, a small root of a few kilometers in an area where normal crustal thickness is about 26 km. Also, lower Pn velocities are apparent there. Again, features of this nature are difficult to assess with the azimuthally averaged time terms. The root is more apparent when the Pn velocity variations are accounted for. The -60-mGal gravity contour corresponds well with the approximate position and small size of this root. High midcrustal arrivals (6.7-6.9 km/s) are often found in this region [Hadley, 1978; Nava and Brune, 1982; Pechmann, 1983]. However, even

with such velocities, crustal thicknesses much over 30 km are not supported by the data used in this study.

In contrast with this, Nava and Brune [1982] use an approximately reversed profile to infer a 42-km thickness for the Peninsular Ranges. Their study uses the Pino Solo earthquake, located in Baja California (31.8°N,115.8°W.), recorded at Pn distances at stations PAS, MWC, and RVR, just north of the Peninsular Ranges. To reverse this, a blast at Corona (near the north end of the Peninsular Ranges) was recorded in Baja California. The intercept times for these profiles (corrected for earthquake depth) are about 7 s. This intercept time can be compared directly to the delays calculated here. The delays calculated in this study are 0.2-0.5 s for the northern stations and Corona plus the 5.5-s round trip delay at Homestead Valley. These delays in California contribute 5.7-6.0 s to the total 7 s intercept. This implies a relative crustal delay of 1.0-1.3 s in Baja California that can be compared directly to the delay maps presented here. For their data to be consistent with the data used in this study, a crustal thickness of about 43 km is needed in Baja California but not in Southern California. Additional support for this hypothesis comes from Shor [1955], who estimates a thickness at Corona of 32 km from Moho reflections. Hadley [1978] has a 31-km thickness for the province. Also, Thatcher and Brune [1973] use surface waves to obtain an average thickness of 25 km for the entire Peninsular Range province.

Evidence for possible mantle material variations is shown by the changes in Pn velocity. Higher velocities are more prevalent east of the San Andreas Fault. The velocity varies from 7.6 to 8.2 km/s within the array. Velocities

offshore seem surprisingly fast. The Salton Trough, an area of high heat flow, is also marked by high velocity. The velocities found here agree well with the study by Vetter and Minster [1981], where they determine velocities in the Pasadena area of 7.8 km/s and in the Mojave of 8.1 km/s.

Pn anisotropy in the oceans is known to be oriented with its fast direction perpendicular to the oceanic rise [Fuchs, 1977; Raitt et al., 1971]. The shear stress induced at the time of upwelling is thought to orient the olivine in the upper mantle [Fuchs, 1977]. Okal and Talandier [1980] find that in French Polynesia the present stress field has reoriented the anisotropy. Raitt et al. [1971] find anisotropy in the Pacific Ocean off California of 3% with the fast direction at N72° E. Bamford et al. [1979] find a similar amount of anisotropy in the western United States with nearly the same orientation. They attribute this to the subduction of the now extinct Farallon plate under North America. Vetter and Minster [1981] find anisotropy in a small array around Pasadena with its fast axis subparallel to the plate boundary. In contrast to this, they find no anisotropy in an array centered in the Mojave region. They hypothesize that shear stresses at the plate boundary induce the anisotropy in the Pasadena area. Other work supports this hypothesis [Fuchs, 1977; Crossen and Christenson, 1969]. The area covered in this study encompasses both of the smaller arrays of Vetter and Minster. The anisotropy found in this study then represents the average of a parameter that possibly varies substantially over the region. The direction of anisotropy found here (N75° W) is off by 35° from that found in Pasadena. This suggests that the average anisotropy is a mixture of an original east-west anisotropy such as in the near

ocean, newer anisotropies induced by shear stresses at the plate boundary, and areas of no anisotropy such as the Mojave. Data and techniques that can map anisotropy in more detail are needed before questions about anisotropy can be properly addressed.

Discussion

As more geophysical data have become available, geophysicists keep finding larger lateral crustal variations in the western United States. To the east of the Southern California array, in Arizona, the Moho is at a depth of 40 km under the Colorado Plateau decreasing to 34 km at the plateau rim and further thinning to 21 km near California [Warren, 1969]. In Nevada, thin crust of 22 km in the west part of the state thickens to over 32 km in the east [Priestly et al., 1982]. The Sierra Nevada has a root that reaches to 50 km in places [Pakiser and Brune, 1980]. In Central California, thin crust of 20 km thickens to 27 km on the east side of the San Andreas Fault [Kind, 1972]. This study finds that Southern California also has considerable structure. This includes offshore thinning, small mountain roots, a rootless mountain, and intracontinental crustal thinning of 10 km. The delay time maps only show the gross shape of the Moho but leaves one with the impression that considerable small-scale structures may exist. This is an important consideration when interpreting Pn refraction profiles.

The Southern California array covers a major plate boundary. It is not surprising that this study should reveal 10 km of crustal thinning as well as velocity contrasts. Kind [1972] has 7 km of thinning across the plate

boundary in central California, and Husebye et al. [1976] show that a velocity contrast may extend to as deep as 75 km. Change in the mantle across the San Andreas is particularly important in the Salton Trough where active rifting is taking place. Neither crustal thinning nor thickening seems to be a prerequisite for the spreading. The only indication of unusual structure in the Salton Trough found in this study is the high Pn velocity found there.

Anisotropy adds a new dimension to upper mantle studies. In the ocean the fast axis is usually perpendicular to the ridge. The continental case is not so simple. Almost 2% anisotropy is found here with a fast axis orientation of N75°W. Comparison with the study of Vetter and Minster [1981] shows that this value of anisotropy must be viewed as an average of a laterally varying parameter.

Chapter 3

Upper Crustal Structure in Southern California From a Tomographic Analysis of Array Data

Introduction

Determining the third dimension of crustal geology has been a primary concern of geophysicists. The Southern California seismic array has provided such opportunities in the past to study mantle structure (Humphreys et al., 1984; Walck, 1980; Raikes 1980) as well as Moho structure (Hearn, 1984; Lamanuzzi, 1980; Hadley, 1978). Here the array is used to investigate the structure of the upper crust. The so-called Pg first arrival times collected on the array are ideal for this study since they sample the upper crust.

Prior investigation of Pg rays in Southern California found velocities of 6.1 to 6.4 km/s over most the array (Hadley, 1978). In particular, the Mojave region characteristically shows these slow velocities as does the offshore area (Hadley, 1978; Corbett, 1984; Pechman, 1983). Another phase, P*, is often observed as the first arrival in the Peninsular Ranges at apparent velocities of 6.5 to 6.8 km/s (Hadley, 1978; Pechman, 1983). Hadley concluded that this was due to the thinning of the shallow and slower Pg layer in the Peninsular Ranges. High P* velocities are also found in the Salton Trough. There, metamorphosed sediments form the basement at depths of 5 km with

velocities of around 6.0 km/s and intruded mafic rocks form a crystalline basement at depths of 13 km (Fuis et al., 1982). The Pg and P* phases are not separated in the data. Because only the first arrivals are used, this is not practical. Here Pg arrivals are considered as those first arrivals occurring between the direct arrivals at about 15 km distance and the Pn Moho refractions at about 150 km distance.

Tomography

Tomography is a method that is widely used in medicine for imaging the body. By measuring ray intensity, ultrasonic velocity or gamma ray intensity, medical technology is able to produce images of body slices, often in real time (Roland, 1979; Deans, 1983). Seismic experiments are substantially different than in medicine but many of the same techniques and principles still apply. Geophysical tomography has found application for the whole earth (Clayton and Comer, 1984; Comer and Clayton, 1984; Dzewonski and Anderson, 1984), the upper mantle (Humphreys et al, 1984), and in seismic exploration (Menke, 1984; Dines and Lytle, 1979). Indeed, many migration and slant stack techniques routinely used in industry are forms of tomography (Deans, 1983). Here an algorithm specifically for the crustal arrivals of the Southern California array is developed and applied.

The inversion of travel times into structure is essentially the problem of imaging an object from its shadows. Radon (1917) was the first to consider this problem in detail. Travel times are essentially line integrals of the slowness (inverse velocity) profiles along the raypaths. For a continuous set of

shadow data, Radon's theorems show us how to uniquely invert for the image of the object. The Radon transform is a line integral through space of a spatially varying quantity. Its inverses are used directly in medicine where the experiment is well-controlled. Equally spaced data make inverse techniques based on the Radon transform particularly appealing since fast Fourier transform algorithms can be implemented. Bracewell and Riddle (1967) were among the first to make practical application of Radon's work; they used it for imaging the solar corona from fan beam radio telescope data. Since then, modern technology has enabled tomographic techniques to be used for radio astronomy data in astrophysics, occultation data in planetary science, nondestructive testing work in engineering as well as the myriad of medical applications (Deans, 1983; Rowland, 1979).

In the particular application considered here, that of inverting earthquake travel times, we do not have the choice of data points. The irregular sampling makes direct application of Radon inverses impossible. In addition, the application involves finite path lengths and station and event static corrections, none of which Radon's work encompasses. Because of this, the problem is approached through linear inversion theory. Similar approaches in medicine are the Algebraic Reconstruction Techniques (ART) and the Kaczmarz method (Rosenfeld and Kaz, 1982).

Processing is begun by windowing out the Pg data. This is shown in Figure 1. A straight line is then fit to the data cloud and the residuals calculated relative to this. The straight line fit gives us a starting model. Assuming refracted raypaths, the intercept time gives the refractor depth and the

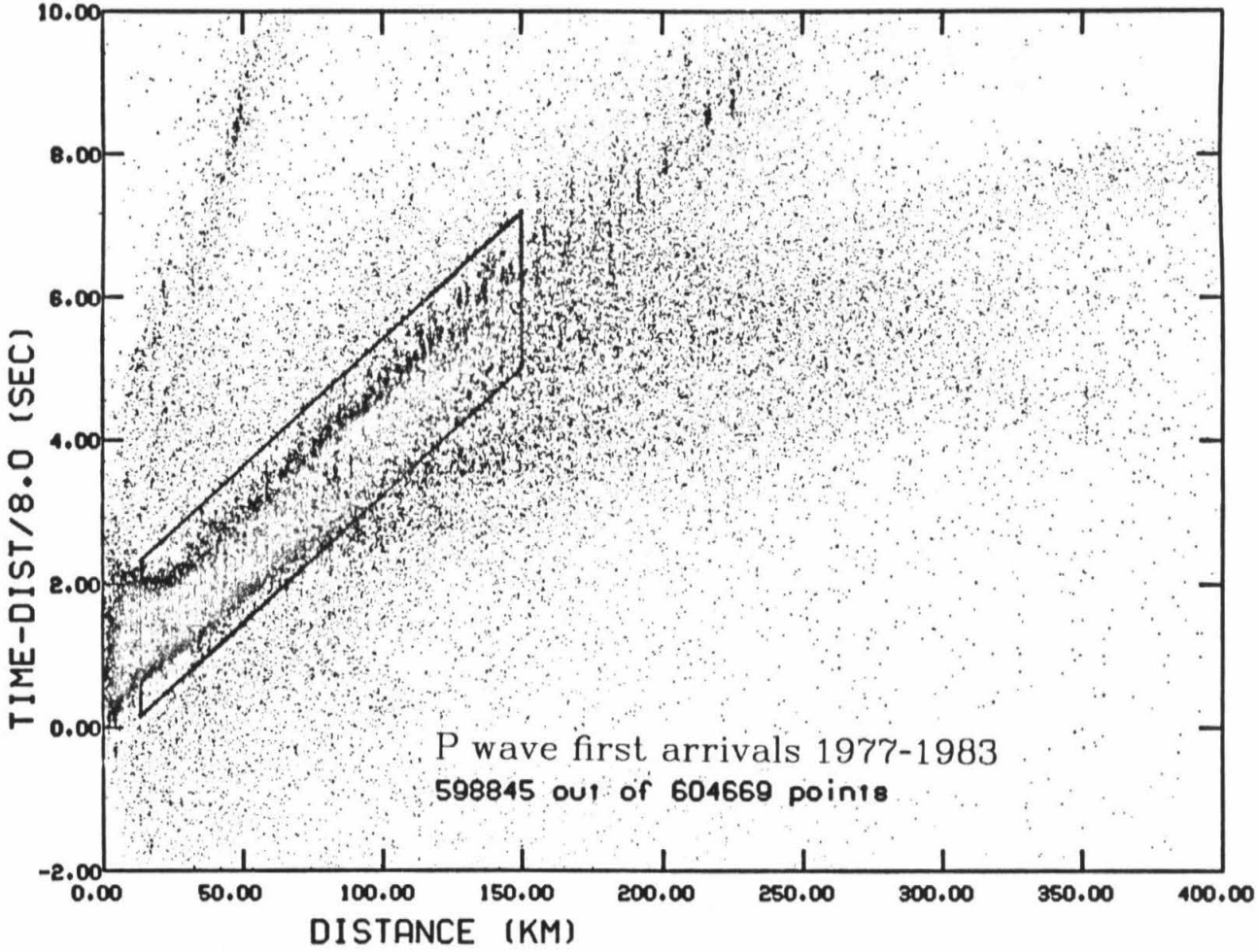

Figure 1. The P wave first arrival data for the Southern California array with the Pg arrivals windowed.

slope gives the slowness. In this starting model, a station elevation correction and an event depth correction are also made. The rest of the processing is to estimate the lateral perturbations in the intercept time and the refractor slowness relative to this initial model.

For refracted rays, the time-term model (Willmore and Scheidigger, 1956) provides an equation which separates the residual travel time into three parts corresponding to the source delay, the station delay, and the refraction path between the source and the receiver. This model is

$$t_{ij} = a_i + b_j + \sum_k d_{ijk} s_k \qquad (1)$$

where t_{ij} is the travel time between source i and receiver j, a_i and b_j are the delays for source i and station j, Δ_{ijk} is the distance the ray travels in block k, and s_k is the slowness in block k. The station delay can be expressed as a function of refractor depth, h, refractor slowness s_0 , and the velocity depth profile, s(z) :

$$a_i = \int_0^h (s(z)^2 - s_0^2)^{1/2} dz \qquad (2)$$

For a constant velocity upper crust, this delay is more simply expressed as

$$a_i = \sqrt{s^2 - s_0^2}\ h \qquad (3)$$

The event delays are similarly expressed only with the total refractor depth, h, replaced by the refractor depth minus the source depth.

To calculate lateral slowness perturbations and crustal delays, a tomographic backprojection method that is based on the Jacobi Iteration technique, of linear algebra is used. With this technique the least squares normal equations are solved by approximating the information matrix by its diagonal elements. This leads to a simple algorithm which allows us to process the travel times on a ray by ray basis. The travel time model (equation 1) can be expressed in a partitioned matrix form as :

$$\begin{bmatrix} \mathbf{A}\,\mathbf{B}\,\mathbf{C} \end{bmatrix} \begin{bmatrix} \mathbf{a} \\ \mathbf{b} \\ \mathbf{s} \end{bmatrix} = \mathbf{t} \qquad (4)$$

where

$\mathbf{A}_{il}$ = 1 if arrival l recorded at station i

= 0 otherwise

$\mathbf{B}_{jl}$ = 1 if arrival l recorded at event j

= 0 otherwise

$\mathbf{C}_{lk} = d_{lk}$ = the distance ray l traveled through cell k

$\mathbf{a}$ = vector of station statics

$\mathbf{b}$ = vector of event statics

$\mathbf{s}$ = vector of slowness deviations .*EQL* $\mathbf{t}$ = vector of travel time residuals

The least squares solution to this problem can be found by solving

$$\begin{bmatrix} \mathbf{A}^T\mathbf{A} & \mathbf{A}^T\mathbf{B} & \mathbf{A}^T\mathbf{C} \\ \mathbf{B}^T\mathbf{A} & \mathbf{B}^T\mathbf{B} & \mathbf{B}^T\mathbf{C} \\ \mathbf{C}^T\mathbf{A} & \mathbf{C}^T\mathbf{B} & \mathbf{C}^T\mathbf{C} \end{bmatrix} \begin{bmatrix} \mathbf{a} \\ \mathbf{b} \\ \mathbf{s} \end{bmatrix} = \begin{bmatrix} \mathbf{A}^T\mathbf{t} \\ \mathbf{B}^T\mathbf{t} \\ \mathbf{C}^T\mathbf{t} \end{bmatrix} \tag{5}$$

Here $\mathbf{A}^T\mathbf{A}$ and $\mathbf{B}^T\mathbf{B}$ are diagonal matrices with the diagonal elements equal to the number of times a specific station or event recorded. Similarly, $\mathbf{C}^T\mathbf{C}$ has elements which correspond to the different cells of the solution. The diagonal elements of $\mathbf{C}^T\mathbf{C}$ give the sum of the squares of the distances through the cell that all the rays take. The off diagonal elements give cross product sums of distances for rays connecting a given pair of cells. The nondiagonal matrices of equation (5) have similar interpretations. The entire information matrix of equation (5) is extremely sparse and diagonally dominant. This allows approximation by its diagonal elements.

Interpretation of the diagonal elements of equation (5) and the elements of the right hand side of equation (5) then give the following estimates for the static delays and the slowness elements.

$$a_i = \sum_j t_{ij} / N_i \tag{6}$$

$$b_j = \sum_i t_{ij} / N_j \tag{7}$$

$$s_k = \frac{\sum_{ij} d_{ijk}^2 (t_{ij} / d_{ijk})}{\sum_{ij} d_{ijk}^2} \tag{8}$$

where N_i and N_j are the number of arrivals at station i and event j, respectively. The static delay estimates are then simply the mean travel time at each station or event. The slowness estimate for a given cell is the average

slowness for all rays delayed by that cell weighted by the square of the distance traveled in the cell. The actual algorithm solves on a ray by ray basis. Each ray is traced across the grid and weighted sums are kept for each cell, station and event involved with that ray. This process is called backprojection since each travel time is projected back along its raypath. Because data are treated sequentially, there is no limit on the amount of data that can be handled.

After backprojection, the convergence of the algorithm is accelerated by determining three-scalar factors, one to multiply all the station delays, one to multiply the event delays and one to multiply the slowness image. The scalars are determined with a three parameter regression to minimize the residual square. Tradeoff between the delays and the slowness image is reduced by this step and its convergence is guaranteed. Note that these scalar constants depend on the data, as does the initial solution estimate; the processing steps are nonlinear. The final minimum residual solution is, however, still a linear function of the original travel time. After first estimate of the delays and slownesses is found, new residuals are computed. Those residuals are backprojected and added to the previous estimate.

The delays computed depend on both the crustal velocity profile and the refractor slowness. Other than the obvious delays caused by the Los Angeles and Ventura Basins and the sediments of the Salton Trough, there is little knowledge of variations in near surface velocities. The delays found depend on both the depth of the refractor and the velocity profile above it. Without independent knowledge of crustal velocities, there is little that can be done to

separate these two effects.

However, the delay estimates can be corrected for variations in refractor velocity. Differentiating equation (3) one finds

$$a_i(s_0) = a_i(s_0+\delta s) - \frac{\partial a}{\partial s_0}\delta s_0 \qquad (9)$$

$$= a_i(s_0+\delta s) + \frac{s_0}{\sqrt{s^2+s_0^2}}\delta s$$

$$= a_i(s_0+\delta s) + F\delta s_0$$

where F, as defined, is the offset distance, the horizontal distance that the ray travels from the refractor to the source or station. As this parameter is dependent upon the crustal velocity profile, which is unknown, it will be approximated by a constant value of 15 km. All station statics are corrected to the constant reference refractor velocity, s_0.

Two possible interpretation extremes then exist for the corrected delays: the delays are due to refractor topography or the delays are due to crustal velocity perturbations. If we assume, a constant velocity crust (5.7 km/s), a 6.2 km/s refractor at 10 km depth, then 0.1s of relative delay corresponds to 1.4 km of refractor topography. If a flat refractor is assumed then 0.1s of relative delay corresponds to 0.12 km/s upper crustal velocity reduction.

The application of tomography to Pg travel time data.

Over 300,000 Pg arrivals are used. These were delineated from the rest of the arrivals by plotting the superimposed travel time plot for all earthquakes that were available from the digital network (Figure 1). The Pg branch was then windowed from 15 to 150 km. A line was fit to this data and outliers of more than 1.1 s were removed. Quality 0, 1, and 2 arrivals were weighted as 400, 100, and 25 respectively. These are the inverses of the estimated variances. Quality 3 and 4 arrivals were not used at all.

The complete algorithm is flowcharted in Figure 2. After determination of delays, the slowness image, and the scaling factors, these effects are removed from the travel time creating a new residual, which in turn is back-projected. All results here are for five iterations. The results for Pg are shown in Figure 3a and the associated delays are shown in Figure 3b. The mean intercept and the inverse slope of the data in Figure 1 are 0.3 s and 6.2 km/s. Assuming a 5.7 km/s upper crustal velocity and assuming an average event depth of around 5 km, we estimate that the Pg rays are bottoming at depths around 10 km.

The velocity range is ± 1.38 km/s but mean velocity perturbations are 0.27 km/s. The high velocities occur in poorly sampled cells on the edge of the array. This agrees well with previously observed velocity range of 6.0-6.8 km/s (Hadley, 1978; Pechman, 1983). The station static delays range over 1 s. Prominent late delays correspond to the Ventura and Los Angeles Basins and the Salton Trough where large sections of sediments have accumulated. In order to more quantitatively assess these results, we must look at the

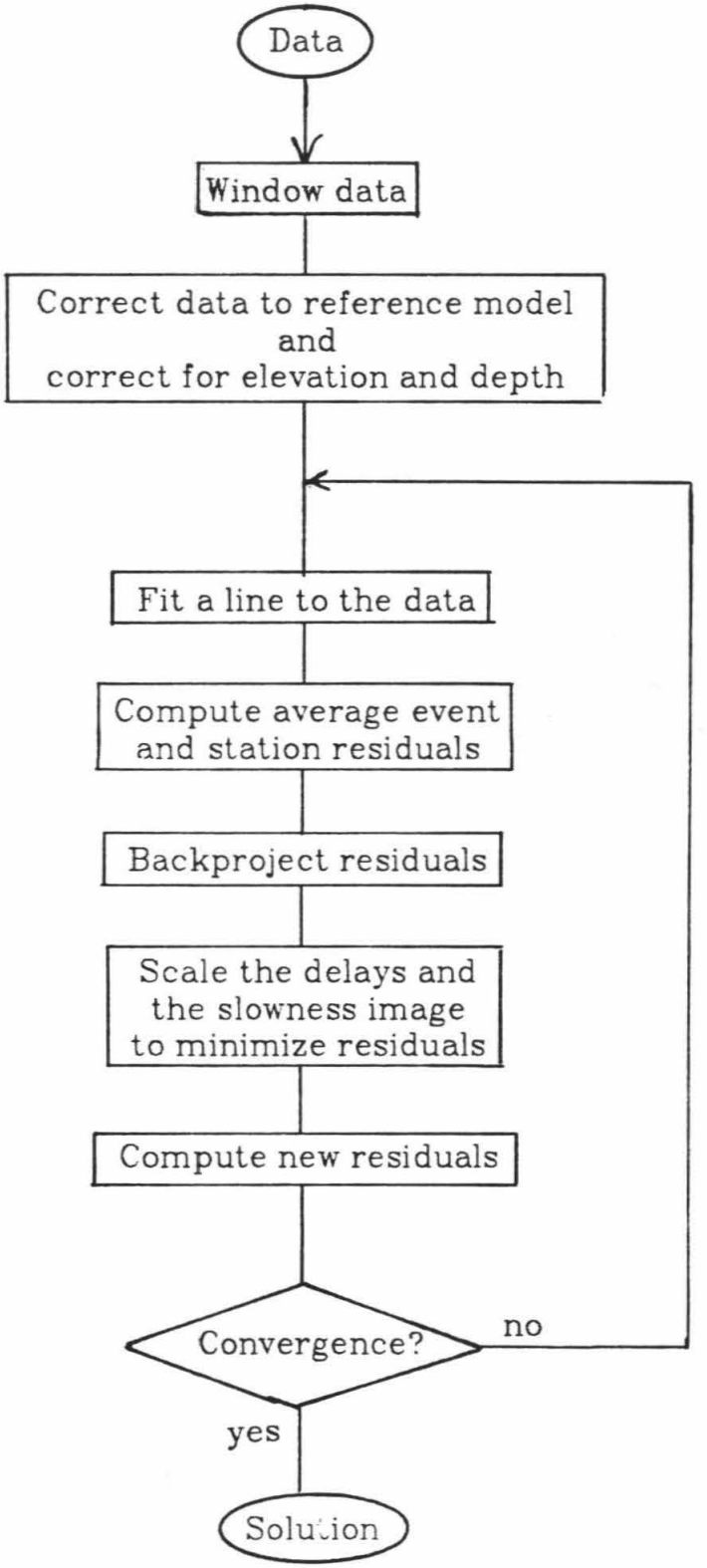
Data
Window data
Correct data to reference model and correct for elevation and depth
Fit a line to the data
Compute average event and station residuals
Backproject residuals
Scale the delays and the slowness image to minimize residuals
Compute new residuals
Convergence?
no
yes
Solution

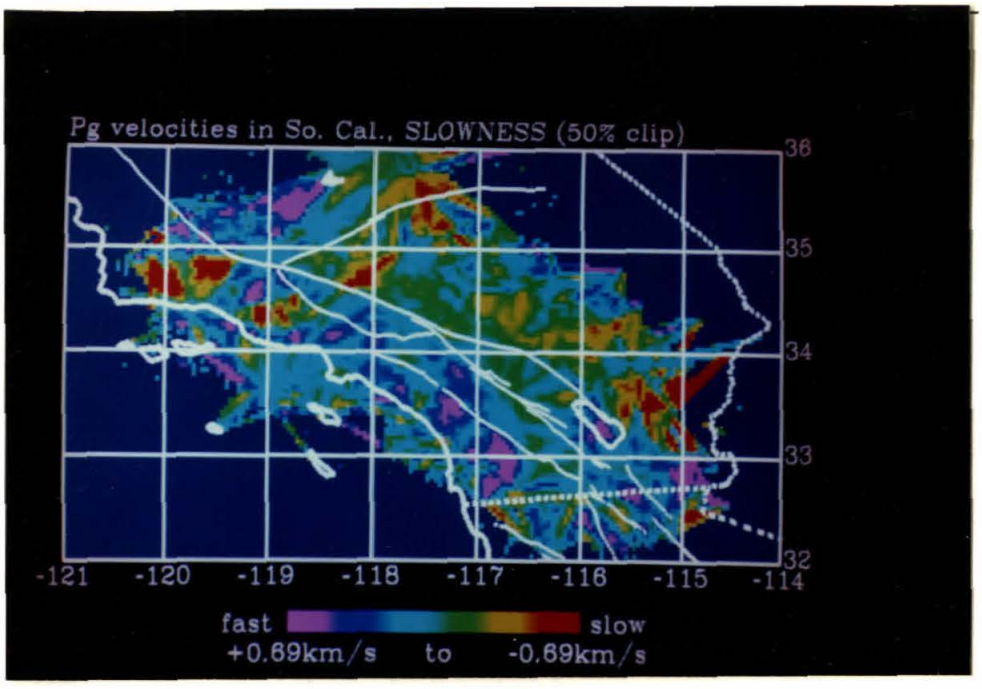

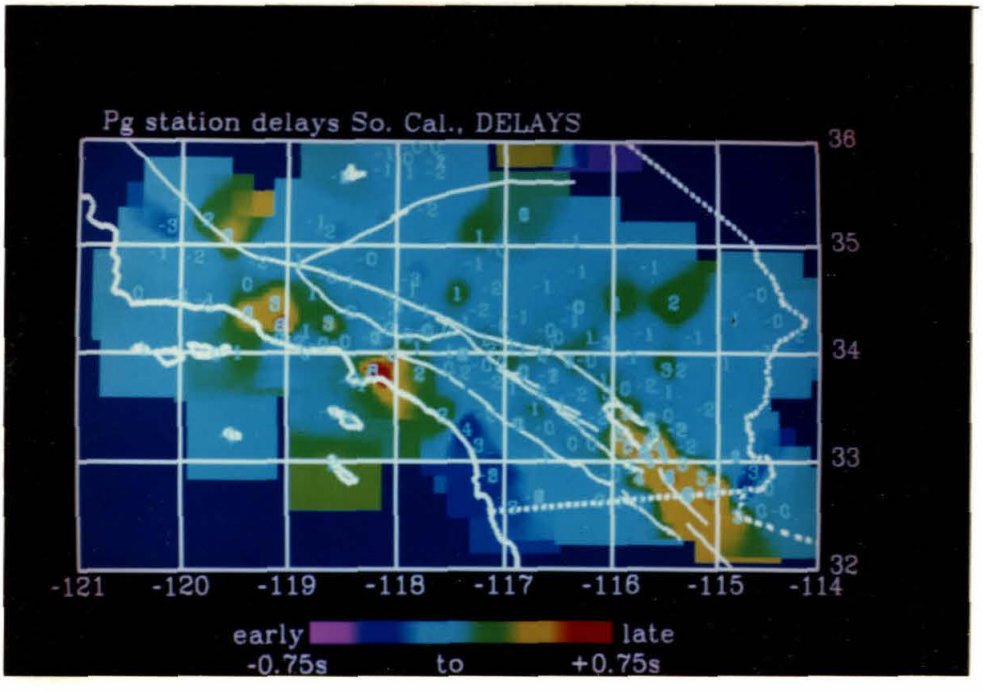

Figures 3a and b. Pg velocity variations in Southern California and Pg station delays in Southern California. Numbers in tenths of seconds.

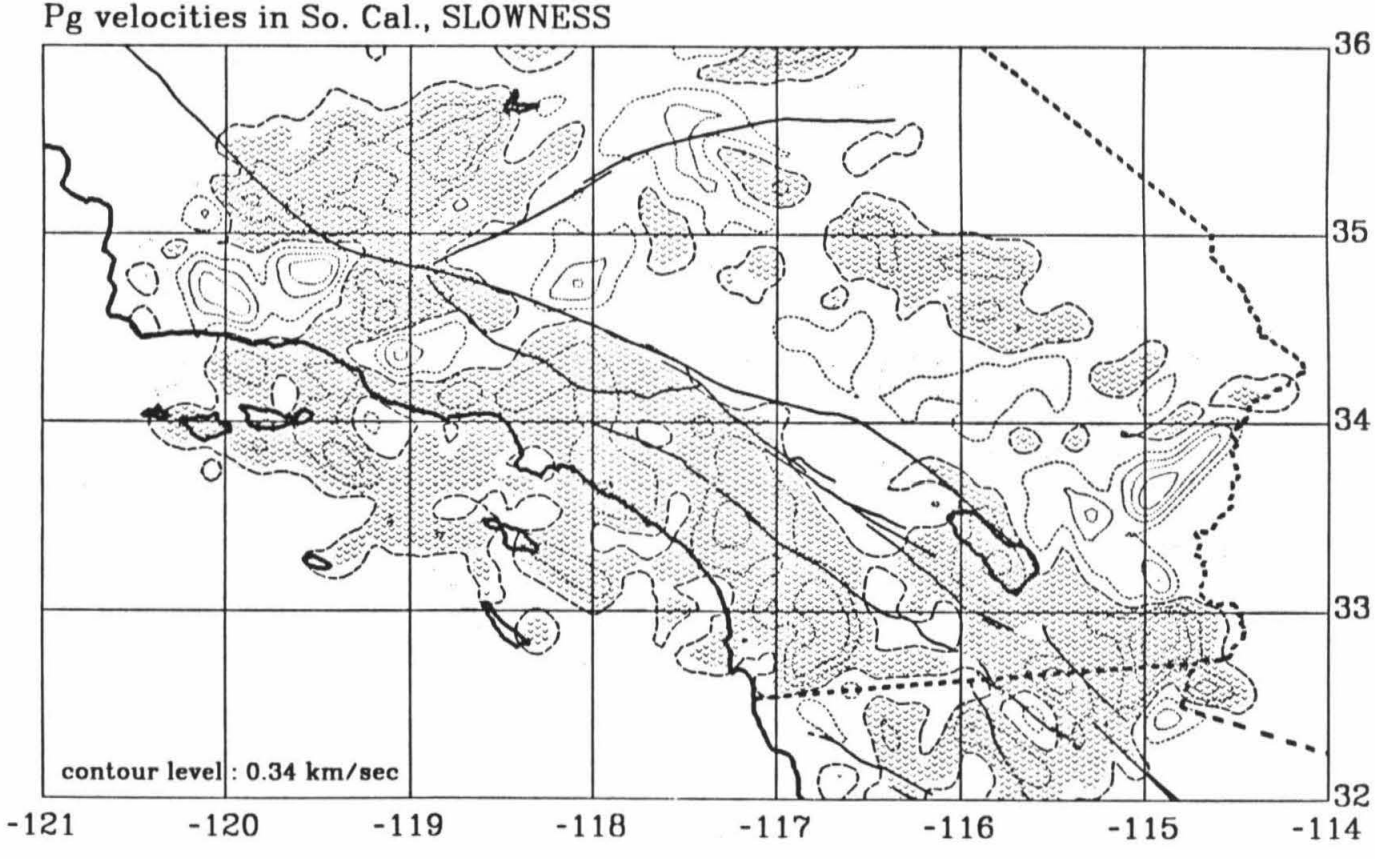

Figure 3c. Pg velocity variations in Southern California. Black and white version.

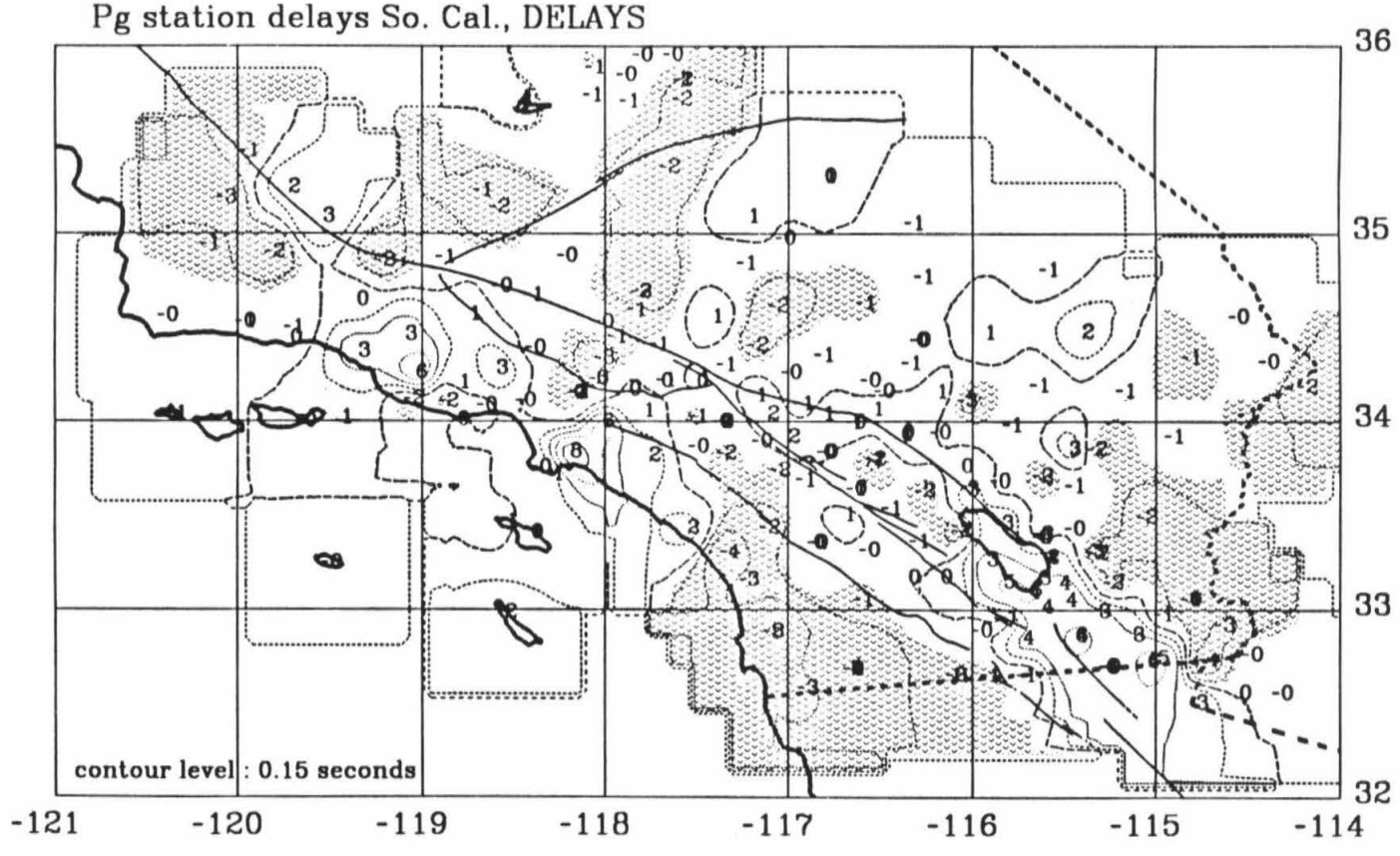

Figure 3d. Pg station delays in Southern California. Numbers in tenths of seconds. Black and white version.

quality of the solution.

Resolution and variance

No inversion study is complete without some discussion of its quality. The quality is investigated by empirically determining the resolution and variances of the slowness elements determined. The use of synthetic data generated with synthetic structures and artificial noise make this process simple and easily interpreted.

The effect of noise is found by using the tomography algorithm on the noise alone. Instead of the actual travel times, times that have a gaussian distribution with an amplitude of 0.55 s for the highest quality arrivals were used. This is a large amount of error, even when epicentral mislocations are taken into account. The actual raypaths of the data set were still used. The results of this are shown in Figure 4a. Note that the maximum amplitude produced by this quantity of noise is 1.33 km/s and that this occurs only on the edge of the region where cells are most poorly sampled. The average noise level is 0.24 km/s. In the center of the array the noise amplitude is below the magnitude of the anomalies that are found. Due primarily to the dense data set, cancellation of noise is extremely efficient. In Figure 4b the delays caused by the noise are shown. The maximum amplitude is 0.06 s. Large delays occur at stations that have only recorded a few arrivals.

With noise then not being a severe problem, our attention turns to resolution. Resolution is the ability of an algorithm to reconstruct a given image. The resolution of a given slowness element can be found by using a synthetic

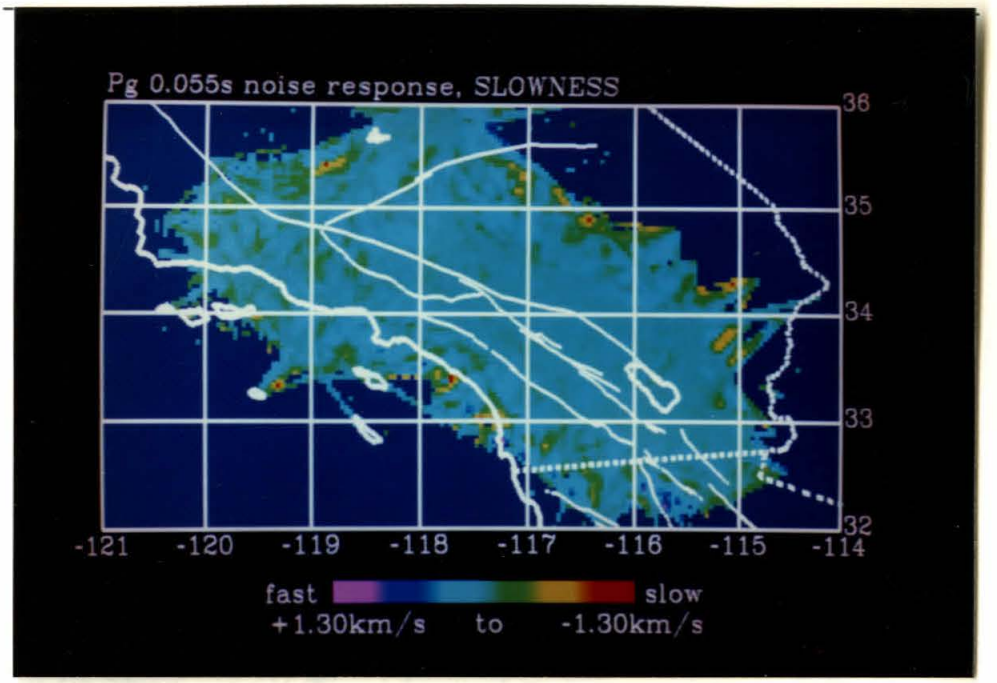

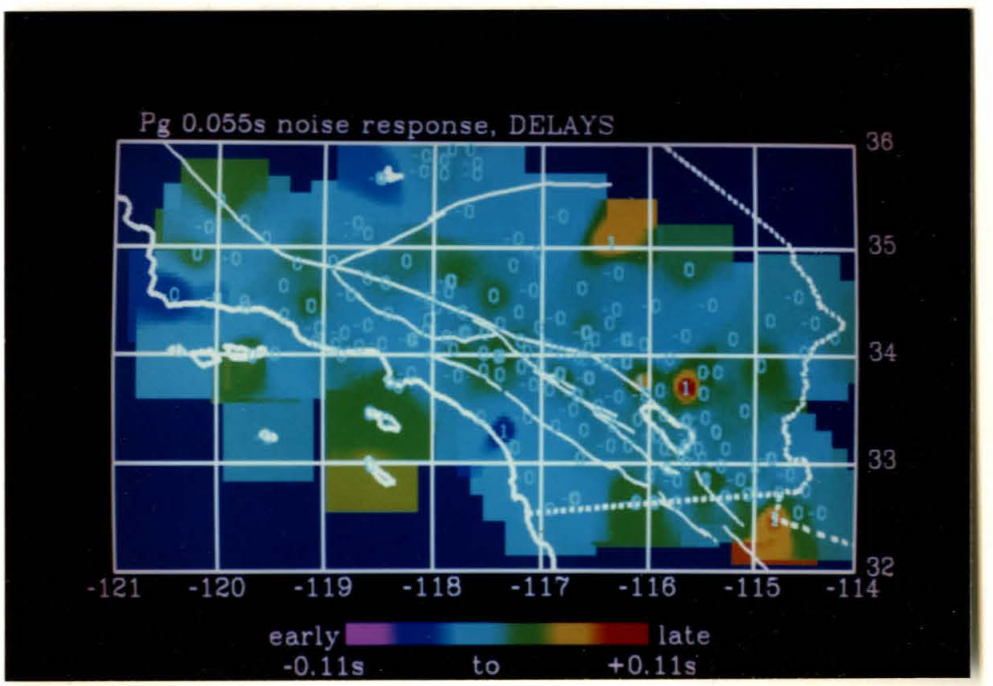

Figures 4a and b. The noise response of Pg velocities and the noise response of Pg station delays. Pure noise with a standard deviation of 0.055 s was input. Numbers in tenths of seconds.

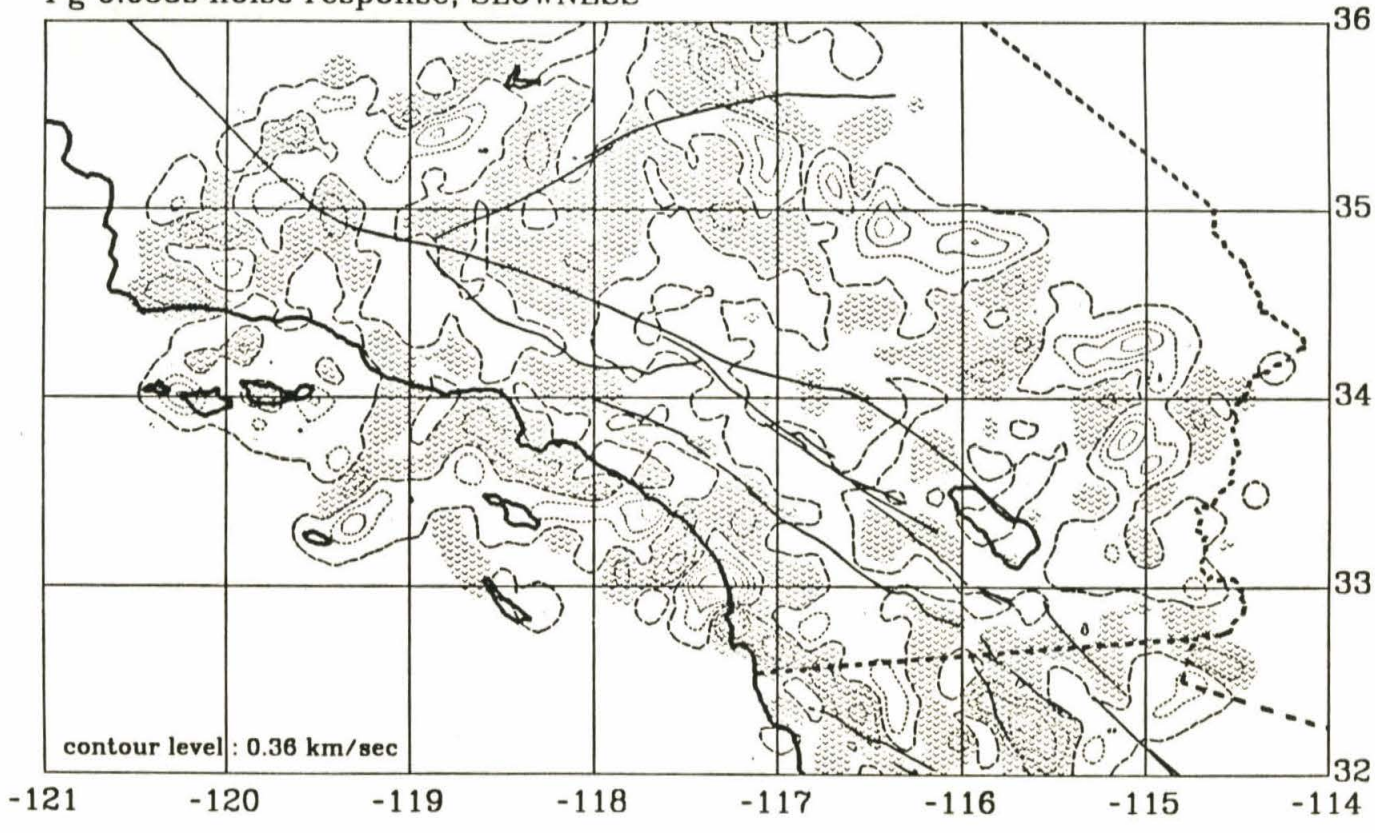

Figure 4c. The noise response of Pg velocities. Pure noise with a standard deviation of 0.055 s was input. Black and white version.

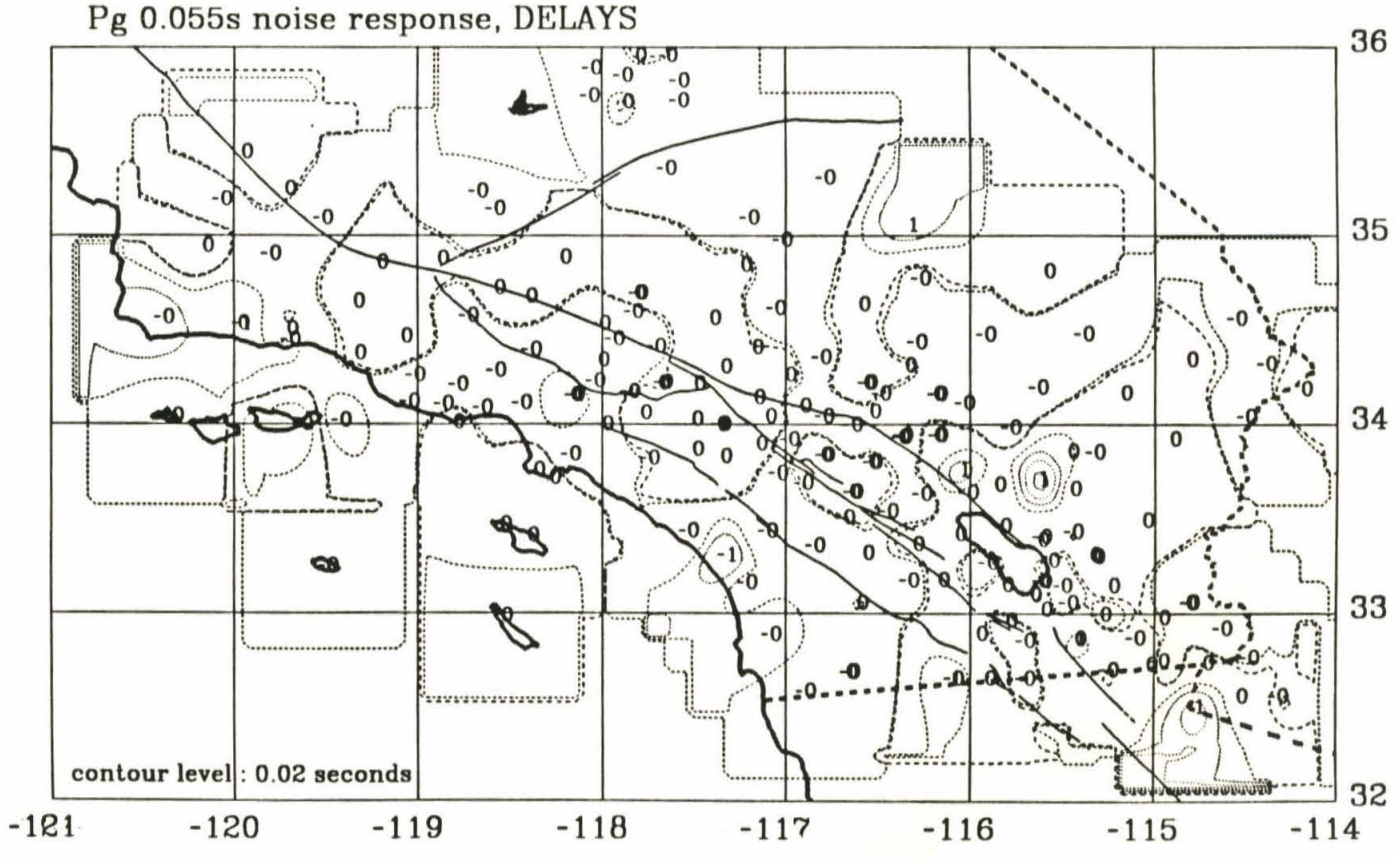

Figure 4d. The noise response of Pg station delays. Pure noise with a standard deviation of 0.055 s was input. Numbers in tenths of seconds. Black and white version.

structure with only that element turned on. Travel times are found using a synthetic structure and the actual raypaths of the data set. This process can give the resolution kernel for any particular element. If this process were to be repeated for all elements, then the equivalent of the resolution matrix that is used in more standard inverse theory would be known (Aki and Richards, 1980). In Figure 5a the resolution for a structure containing separated points is shown. The input slowness element amplitudes were ± 0.39 km/s so 33% of that is reconstructed. Because the anomaly has been blurred into neighboring cells, the amplitude is decreased. Resolution widths are about 25 km for the 4 km by 4 km cells. Some of the cells have streaked along the azimuth of maximum ray density. Figure 5b shows the delays associated with this synthetic structure; note their small amplitude. In Figures 6a and b the resolution of single station delays is shown. Here the synthetic data is constructed with no slowness anomalies and selected stations recording nonzero delays. The delays are reconstructed almost perfectly to their true amplitude of ± 0.1 s and only the slowness elements on the very edge have tradeoff difficulties.

As a final demonstration of resolution, the tradeoff between the delays and slowness perturbations is shown. This has proven to be the most difficult problem with the data. It is extremely difficult to tell if late arrivals are due to a static source or receiver delay, or due to a localized velocity anomaly. The synthetic structure chosen has horizontal bars of constant slowness alternating vertically across the array and vertical bars of constant event and station delay alternating horizontally across the array. Again, the real

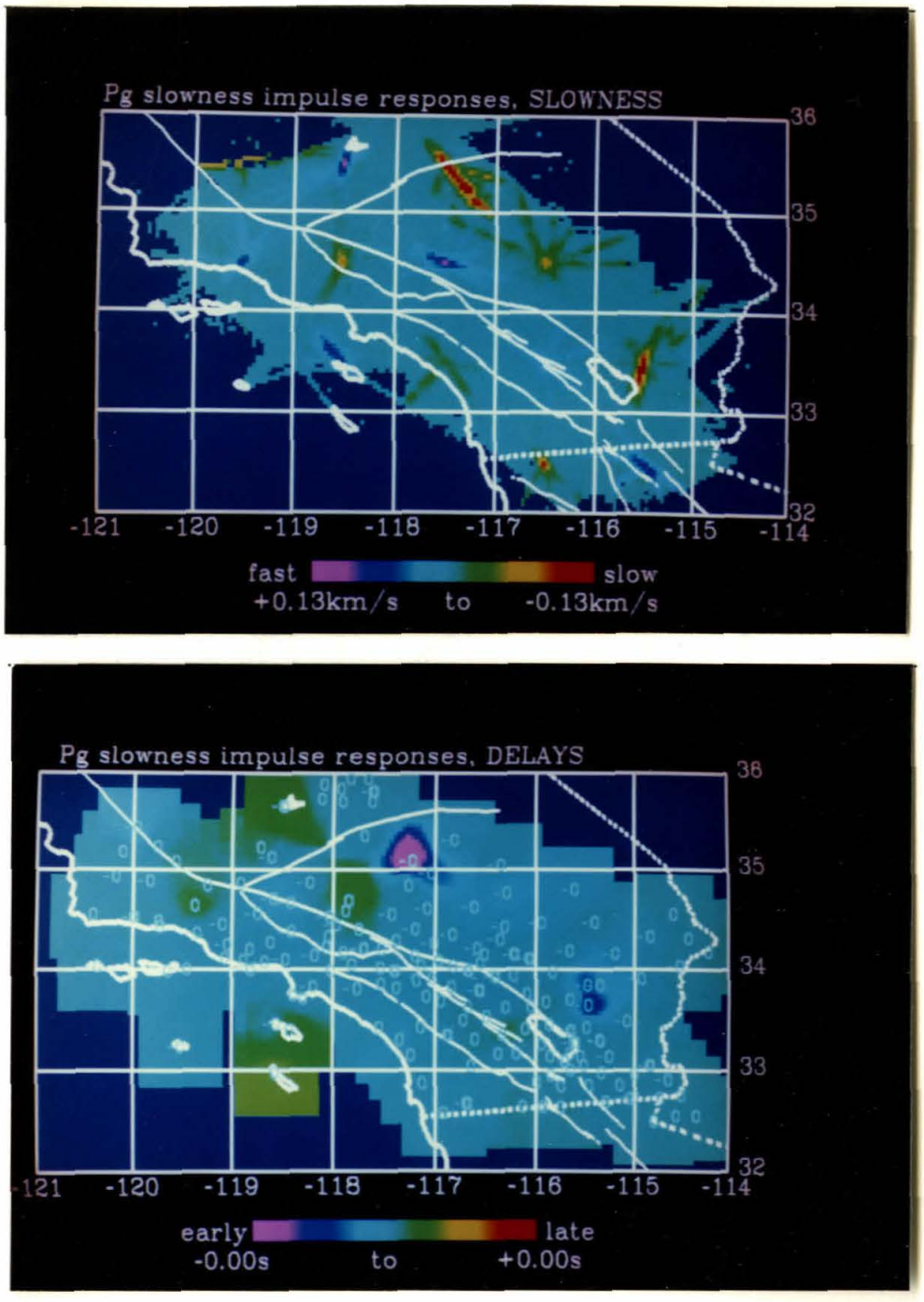

Figures 5a and b. The slowness response of individual slowness cells for Pg arrivals and the station delay response of individual slowness cells for Pg arrivals. Numbers in tenths of seconds.

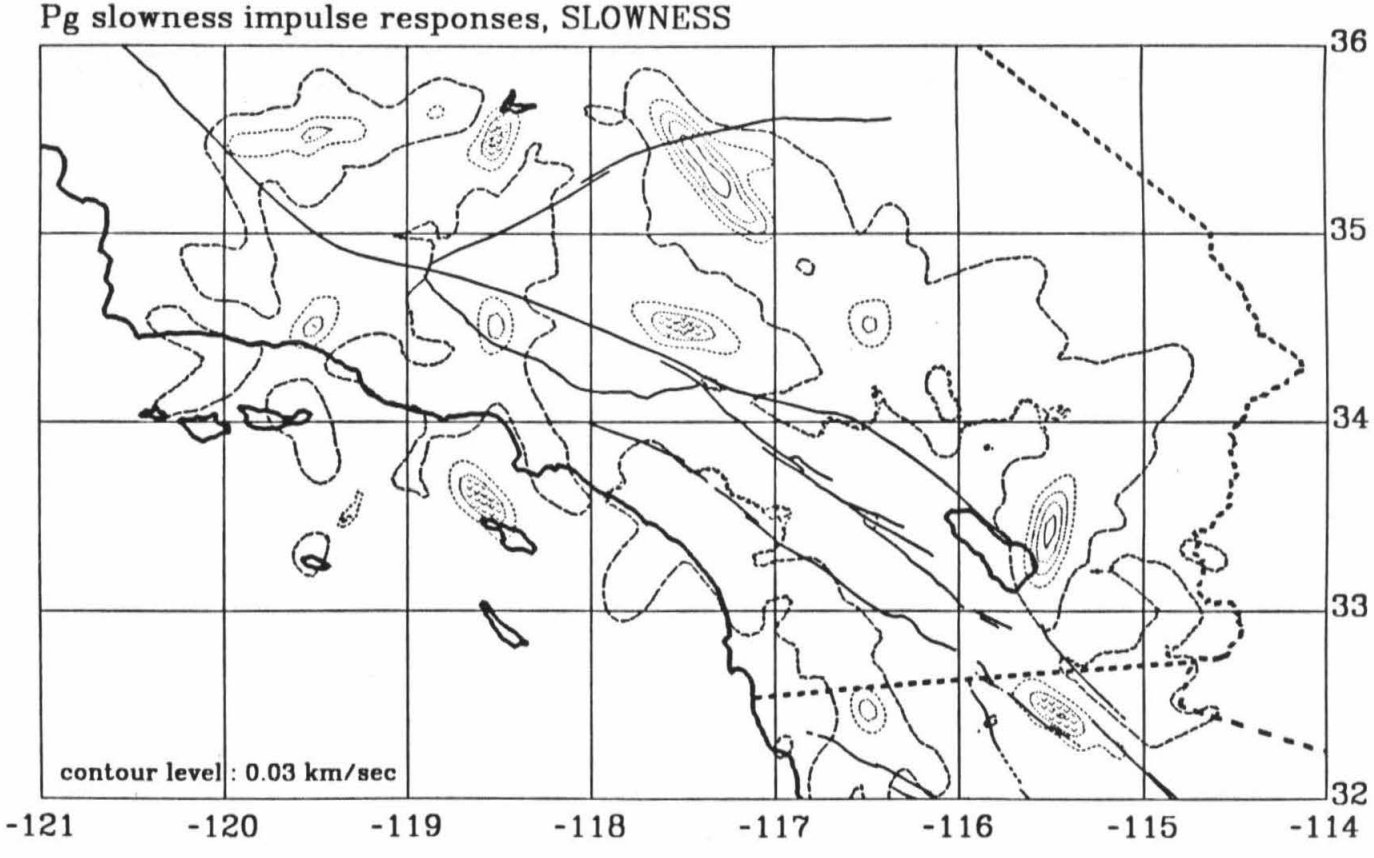

Figure 5c. The slowness response of individual slowness cells for Pg arrivals. Black and white version.

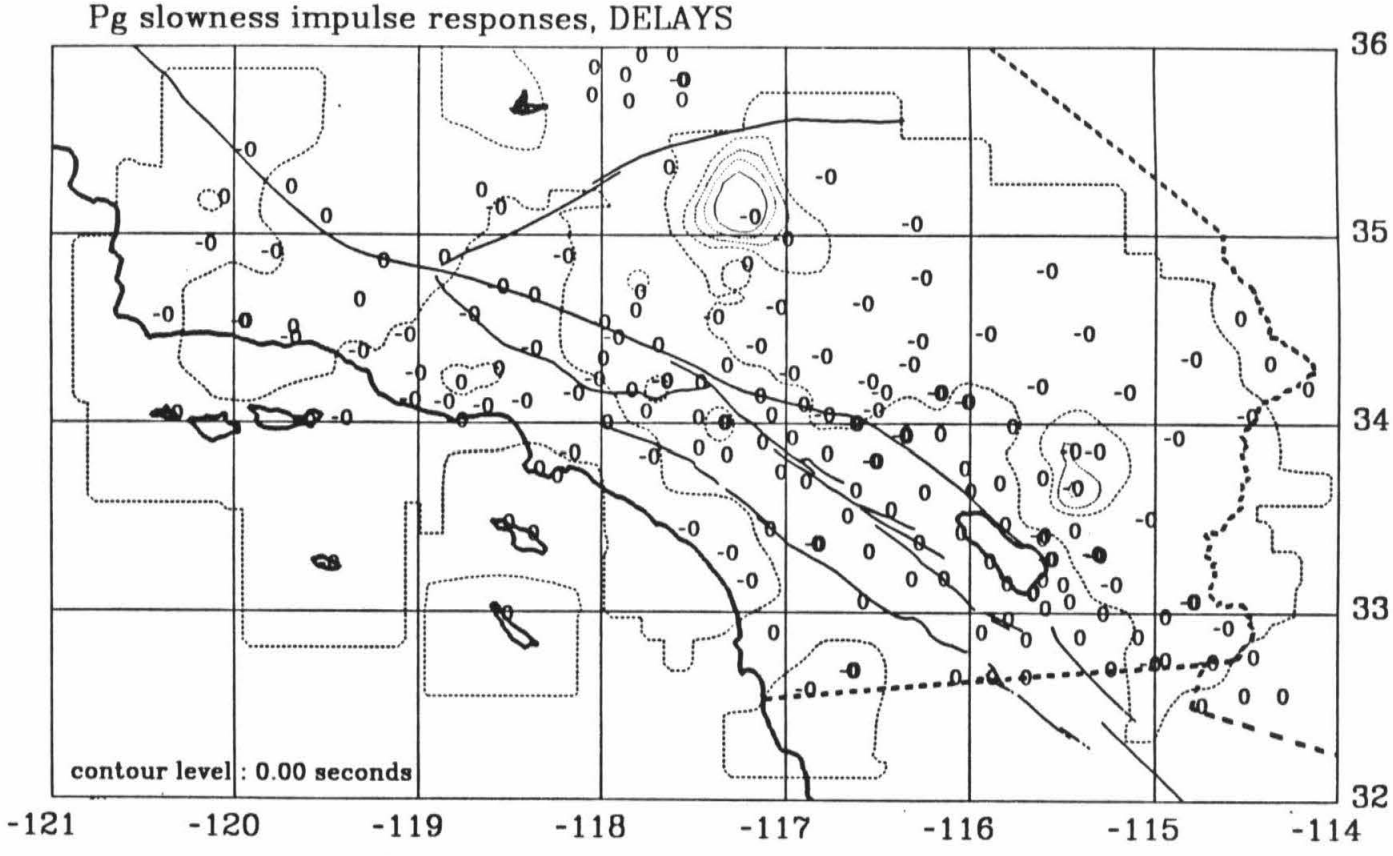

Figure 5d. The station delay response of individual slowness cells for Pg arrivals. Numbers in tenths of seconds. Black and white version.

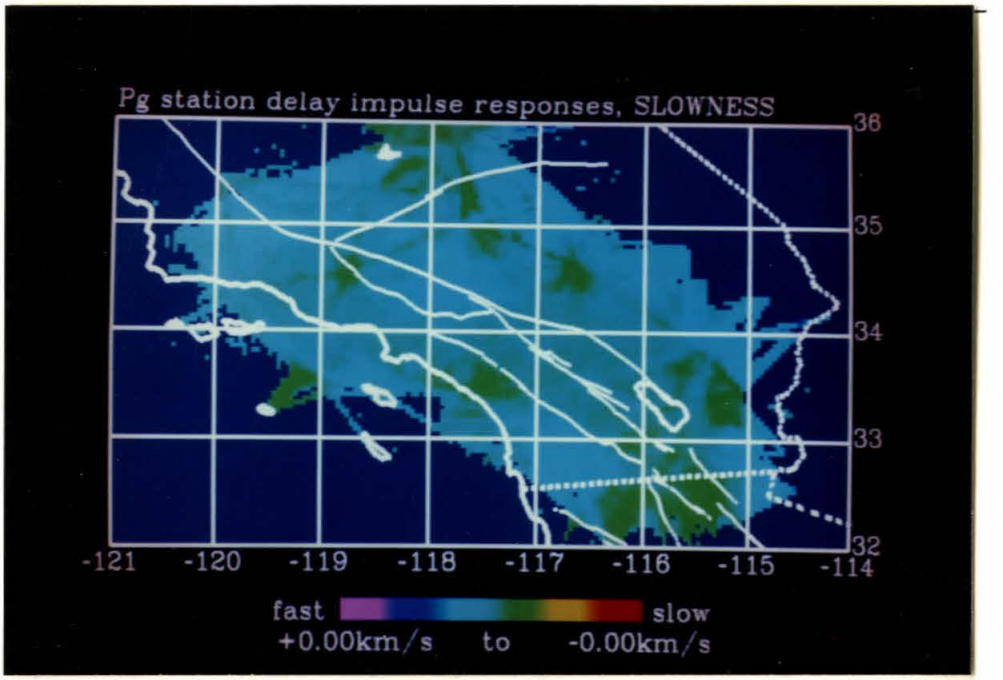

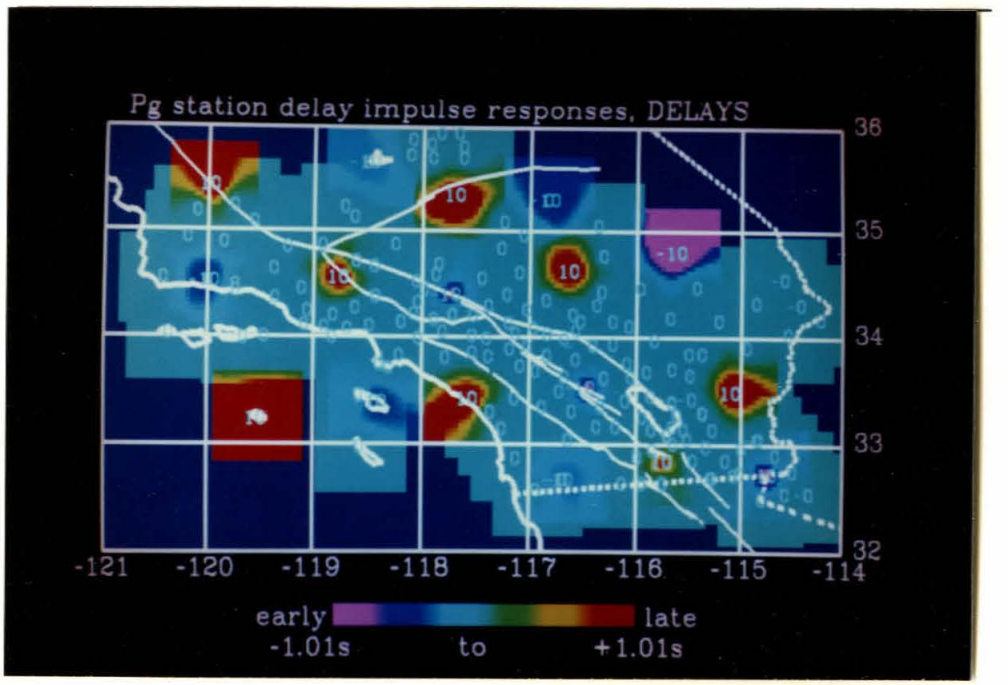

Figures 6a and b. The slowness response of individual station delays for Pg arrivals and the station delay response of individual station delays for Pg arrivals. Numbers in tenths of seconds.

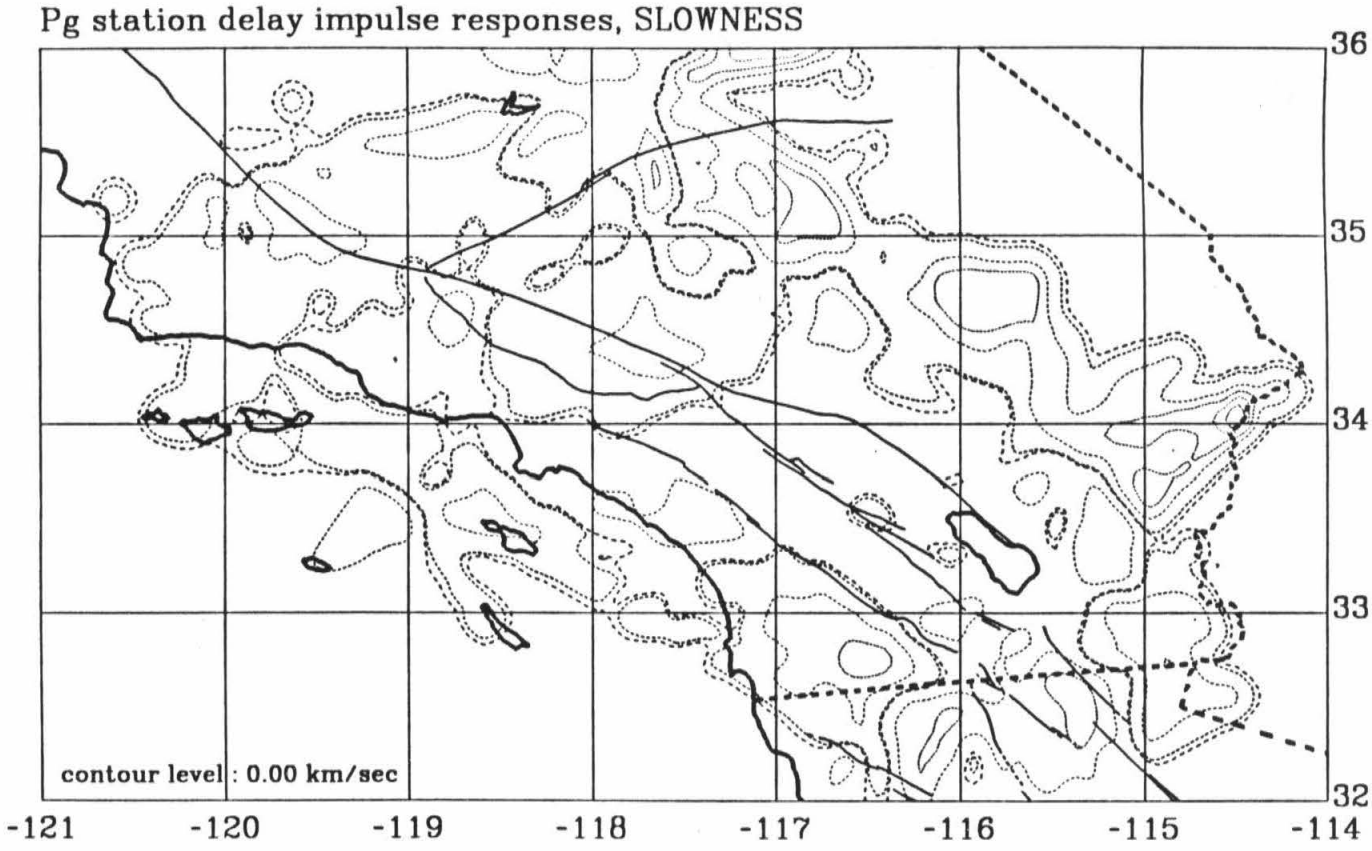

Figure 6c. The slowness response of individual station delays for Pg arrivals. Black and white version.

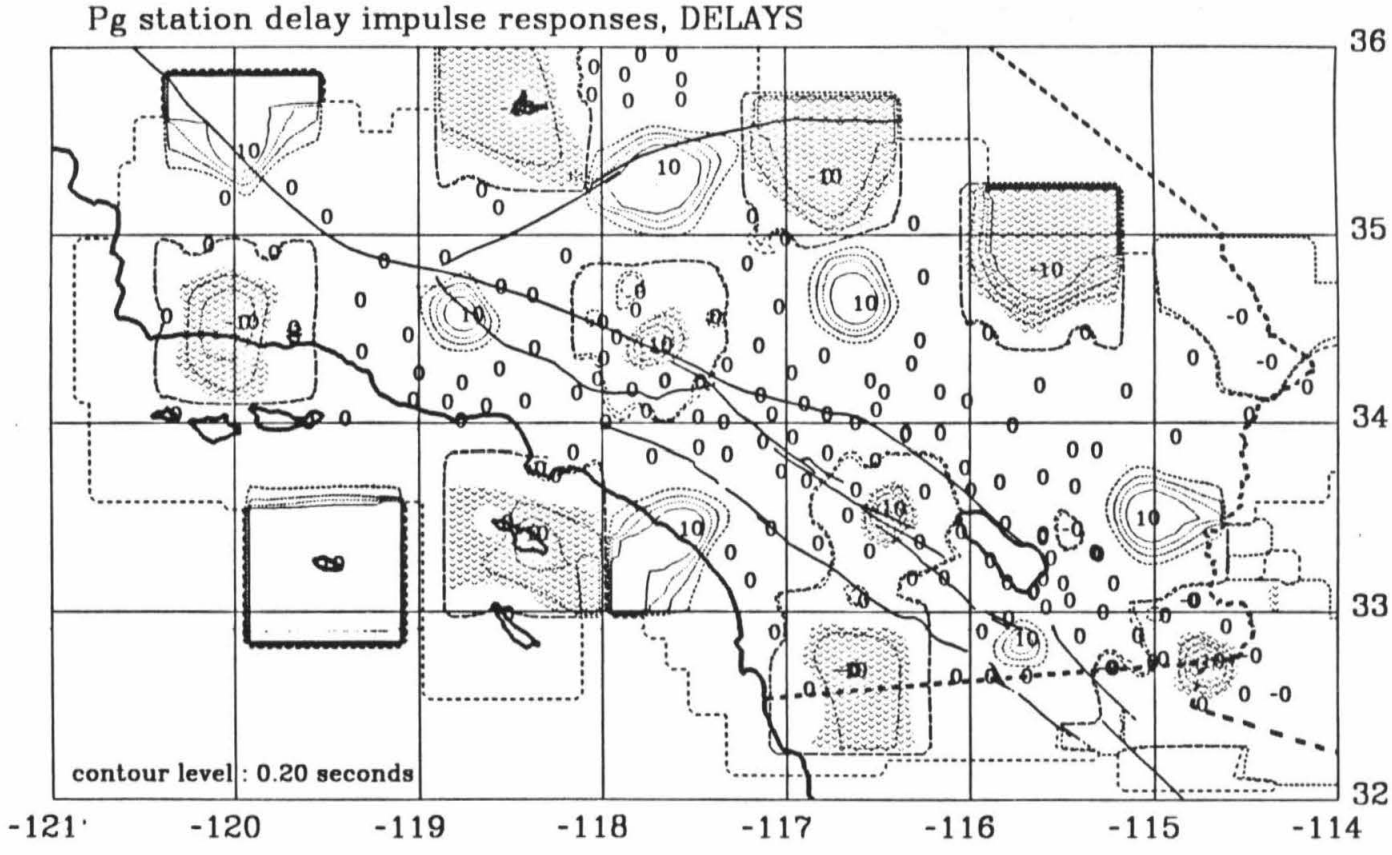

Figure 6d. The station delay response of individual station delays for Pg arrivals. Numbers in tenths of seconds. Black and white version.

raypaths of the data set are used. The results are shown in Figures 7a and b. Examination shows that some tradeoff exists but the main pattern is quite clear. The individual station responses give little tradeoff with the slowness image (Figures 6a and b) but the constructive interference of several close stations is capable of distorting the slowness image. The input amplitudes were ± 0.15 s and ± 0.20 km/s. The average amplitude of the delay stripes is correct but individual stations can have errors of up to 0.2 s. The slowness bars here have maximum amplitudes that are too high by a factor of almost three but the mean amplitude of 0.27 km/s is closer to the input amplitude.

The slowness image for Southern California (Figure 3a) shows many of the streaking artifacts that are very apparent in the slowness impulse image (Figure 5a). Streaking is also apparent in the striped model. This artifact is due to azimuth bias in certain regions. Raypaths are predominantly from one azimuth and so velocity perturbations are spread out along that azimuth. This is primarily a problem with the data distribution and not with the method. Generalized inverse theory would solve the problem by setting unresolved eigenvectors to zero. Tomography produces the recognizable artifact of streaking.

Streaking is particularly obvious from the Coso area (35.7°, −117.6°) where a large number of events and stations are located. Cells on the northeast side of the image are sampled predominantly by raypaths from Coso, causing streaking in the northwest azimuth. Typical resolution widths are on the order of 25 km in Figure 5a. Features in the slowness image much smaller than this are spurious, particularly on the edge where the noise level

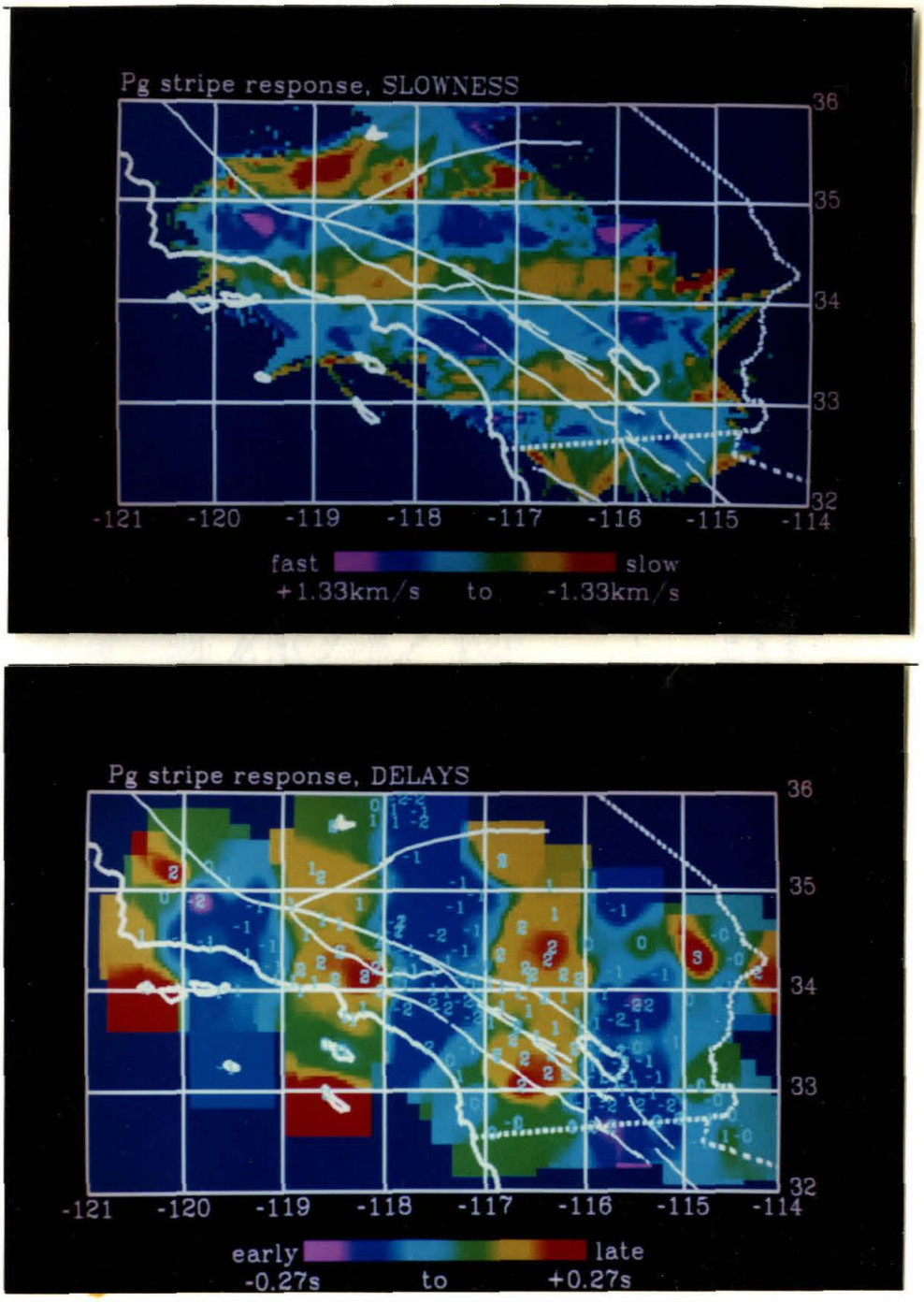

Figures 7a and b. The slowness response for Pg arrivals to a test pattern and the station delay response for Pg arrivals to a test pattern. The original model had horizontal stripes in slowness variations and vertical stripes in the delay variations. Numbers in tenths of seconds.

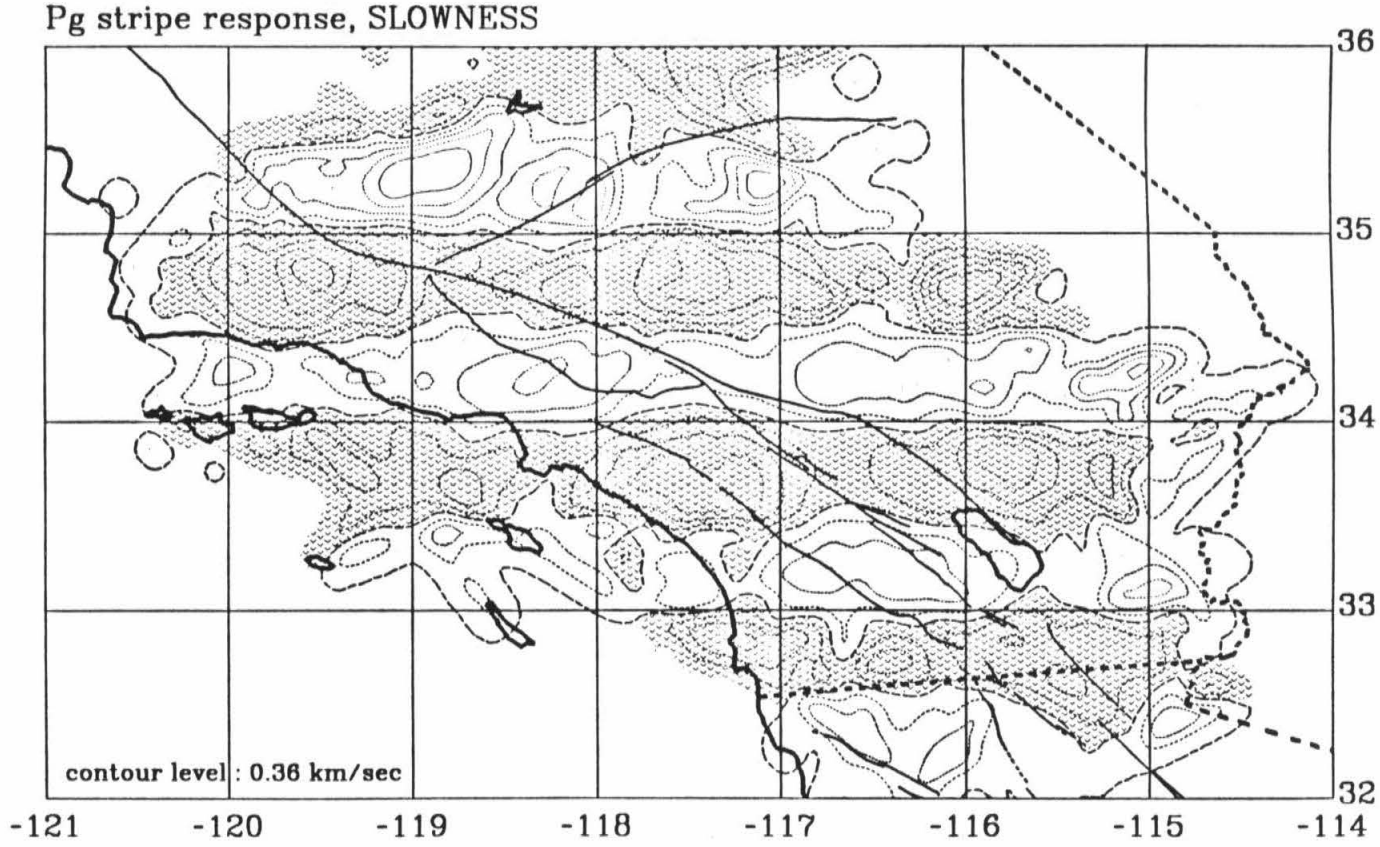

Figure 7c. The slowness response for Pg arrivals to a test pattern. The original model had horizontal stripes in slowness variations and vertical stripes in the delay variations. Black and white version.

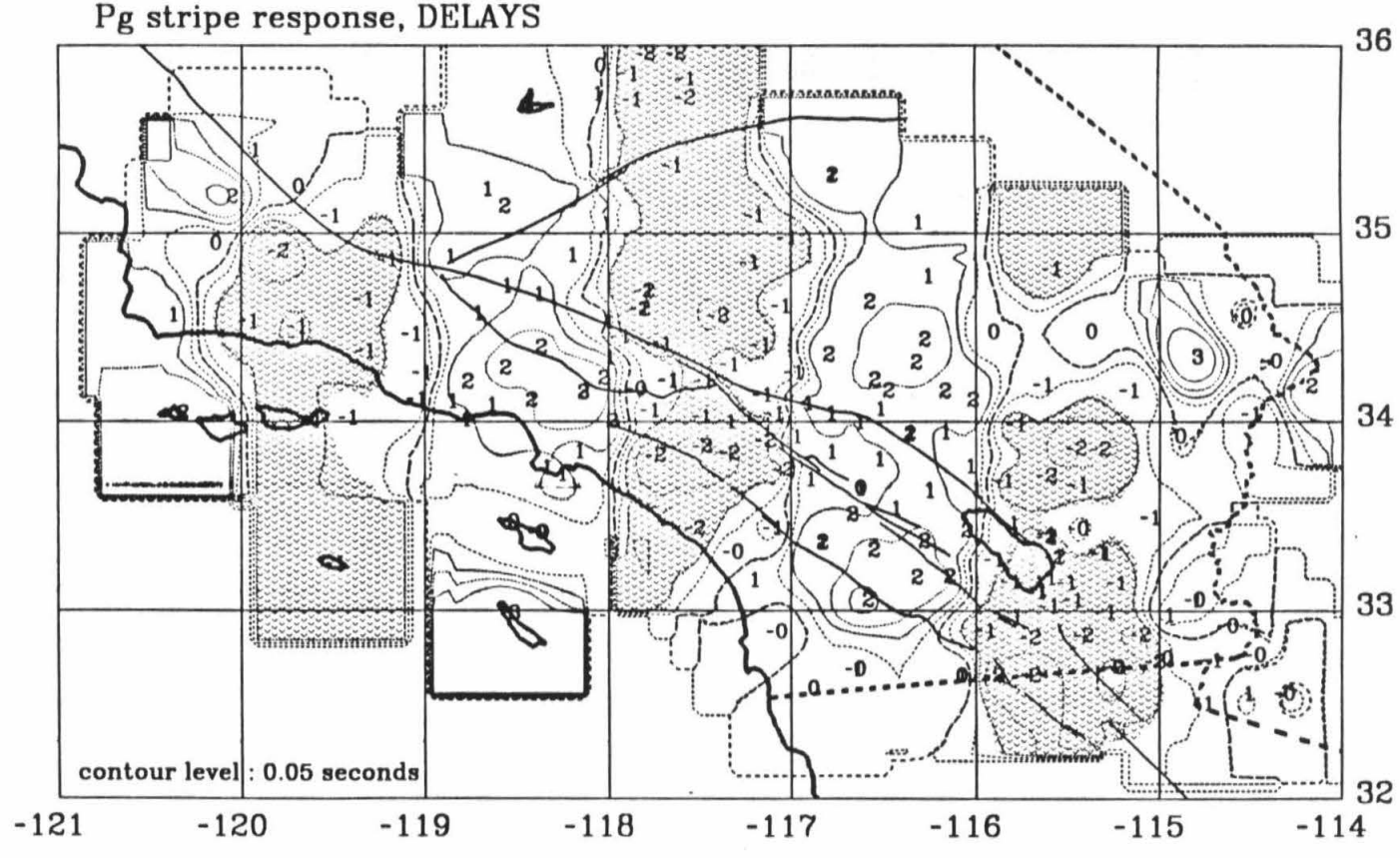

Figure 7d. The station delay response for Pg arrivals to a test pattern. The original model had horizontal stripes in slowness variations and vertical stripes in the delay variations. Numbers in tenths of seconds. Black and white version.

is higher.

As the solution found for Southern California is much smoother than the striped model we feel that the delays found are good within 0.2 s. Comparison of the slowness image and the delays (Figures 3a and b) shows little consistent correlation between the delays and slownesses. Judging from the synthetics, the larger features of the slowness image have essentially the correct mean amplitude but the extreme points are probably correct only within a factor of three. The results show much larger amplitudes than was found earlier by Ergas and Jackson (1981). They had removed station delays by removing their average residual. Our experience found that static delays contribute as much to the residual as do the slowness variations and they must be explicitly included as part of the problem.

Discussion

The San Andreas Fault system is spectacularly imaged in Figure 3a. The San Andreas is particularly apparent south of the Garlock Fault to the Coachella Valley region. Rocks on the Pacific plate are faster with velocities near 6.6 km/s. Rocks on the opposite plate have slower velocities of less than 6.0 km/s. Also nicely outlined are the westernmost Garlock Fault and the northern San Jacinto Fault. The intersection of the Garlock Fault and the San Andreas Fault outlines the Antelope Valley region. Similarly, the corner between the San Andreas and the San Jacinto Faults is well outlined. Comparison with the gravity of Southern California (Oliver, 1981) shows many of these same features. Low velocity values in the Mojave correspond to low

gravity values there.

The associated delays (Figure 3b) show little of the tectonic correlations seen in the slowness image. Instead the delays are dominated by sediment delays in the Ventura and Los Angeles basins and the Salton Trough. Excluding those areas the delays vary on average about ± 0.3 s. This could correspond to up to ± 4.2 km refractor topography in the absence of upper crust velocity variations.

Impressively, the midcrustal velocities do not seem to see either the San Gabriel Ranges or the San Bernardino Ranges. Resolution quality in the Ranges is quite good as seen by the clearness of the San Andreas in Cajon Pass. Both of the batholiths are more dense and thus presumably faster, than the Mojave region. Yet neither of the batholiths show up as a unit at Pg depths. Instead that area seems to have Mojave-type velocities. The San Gabriels should have a velocity intermediate between the Mojave and the Peninsular Ranges, again they are not seen as a unit. It seems that these large batholiths do not exist at depths of 10 km. Evidence shows that most of the province has been displaced. There are 90-degree rotations in the rocks of the westernmost Transverse Ranges (Luyendyk et al., 1980). The San Andreas clearly cuts through the Transverse Ranges at Pg depths. The San Gabriel and San Bernardino mountains could not have formed as a continuous structure, given 300 km of fault offset, so the present juxtaposition is primarily coincidence. Indeed, Powell (1981) has shown that the San Gabriels have moved from analogous terrain south of the San Bernardino Mountains in the Mojave Desert. No root is apparent for the San Gabriels and, at most, an 8 km

root exists for the San Bernardinos, far less than that predicted by isostasy (Lamanuzzi, 1982; Hearn, 1984). However, the gravity-elevation ratio for the Transverse Ranges is consistent with the regional average (Oliver, 1980), thus indicating isostatic balance, but either with a shallower compensation depth or a broader region of compensation. It could be possible that a large detachment surface exists at shallow depths underneath the San Bernardino Mountains. The shallow seismicity base of 5 to 10 km in the Mojave and underneath the San Bernardinos supports this (Corbett, 1984). The Transverse Range province, though, contains more than the San Gabriel and San Bernadino batholith complexes. The Santa Monica Mountains, Santa Ynez Mountains and the Channel Islands are also included in this high relief province. The batholiths of the Transverse Ranges are allochthonous surficial features. The granitic material and other rocks of the Transverse Ranges have piled up in the convergent zone of the big bend area of the San Andreas Fault.

The only part of the Transverse Range area that stands out is the north Ventura Basin. Comparison with the static delays shows large delays for the same area. The sediments of Ventura cause both slow velocities and late arrivals. In contrast, note that the Los Angeles Basin shows up only in the static delays, as does the Salton Trough. This feature is at least partially real and raypaths traversing the region feel the effect of the basin. The slow velocities near Ventura are real and are due to raypaths which actually traverse the basin.

The Tehachapi Range forms the southernmost tip of the Sierran batholith. It is bounded on the south by the Garlock Fault. Although the Sierras

and the Owens Valley region show slower, Mojave-type velocities, the Tehachapies show faster velocities. The Tehachapi Range, then, may be similar to the Transverse Ranges where the granitic rocks are surficial and the topographic high is due to convergence in the big bend area. The westward bend of this southern Sierran tip may indicate that these rocks have been dragged by left lateral movement on the Garlock Fault.

In contrast to the southern Sierran tip and the Transverse Ranges, the Peninsular Ranges do extend to Pg refractor depths. High velocity refractors have been noted here before (Hadley, 1978; Simmons, 1977). Also the tonalites of the Peninsular Ranges have extremely high densities, some up to 2.85 gm/cc (Silver, pers. comm.). Velocities here are from raypaths either refracting through the batholith or along its base. The delays show no evidence for the refractor being deeper there. In fact, along the coast they show evidence for a shallower refractor. Perhaps the base of the batholith becomes shallower along this edge. If we assume higher crustal velocity of 6.2 km/s instead of 5.7 km/s and a refractor velocity of 6.5 km/s there, the time delay due to 5 km of fast overburden is -0.18s. In terms of depth, this could add 2.5 km more to a depth estimate there.

The San Jacinto block, wedged between the San Andreas and the San Jacinto Faults, has a different, lower velocity character than the rest of the Peninsular Ranges. It seems to be more closely associated with Mojave velocities. It also seems to have early delays of 0.2s indicating a refractor 3 km shallower there. The 30 km of offset on the San Jacinto Fault is too small to cause the velocity pattern seen. As the Peninsular Ranges have moved up

against the big bend area the San Jacinto block may have overridden onto the opposite plate. This would develop the surficial bend in the San Andreas even more. The plate boundary, past or present, in the midcrust could cut directly underneath the San Jacinto Fault from Cajon Pass to the Salton Trough.

The Mojave Desert region, particularly in the Antelope Valley region, shows a characteristic velocity of less than 6.0 km/s. These low velocities extend into Arizona (Sinno et al., 1981; Warren, 1969). Similar velocities can also be found in the Gabilan Range, displaced in a right lateral sense from the Mojave. The displacement, which is poorly constrained, seems larger than the 300 km of San Andreas offset.

South of the Salton Sea is an area of very high apparent Pg velocity. Again this result is corroborated by the high apparent Pg velocities (up to 7.0 km/s) that are observed from events in that area. Also, Fuis et al. (1982) find high velocities there. They interpret these as layers of metamorphosized sediments and intruded volcanic material. Their 7.0 km/s layer is at depths of 13 km. The delays that are seen here (0.2 to 0.5 s) are due to the sediments on the valley's surface.

Conclusions

Tomographic backprojection is an efficient and effective method for investigating crustal structure. Here, tomographic backprojection is extended to include station and event static delays. By using this method for the Pg arrivals of the Southern California array, the major crustal blocks of Southern California are clearly outlined. The boundaries of these blocks

correspond with the fault zones of the San Andreas Fault, the Garlock Fault, and the San Jacinto Fault. Lower velocities are in the Mojave region and higher velocities are in the Peninsular ranges and the southern Salton Trough.

Many of the features observed are quite different from their surface expressions. The Transverse Ranges are not seen and neither is the Tehachapi Range. This suggests that these batholiths are only surficial. The San Jacinto block has velocities more akin to the slow Mojave than the faster Peninsular Ranges. It also has a shallower refraction depth. Perhaps the block have overridden Mojave material.

Chapter 4

Pn velocities in Southern California

Introduction

Travel times from the Southern California array are used here to investigate the velocity structure of the Moho discontinuity in Southern California. Dramatic differences in velocities along the surface of the mantle as well as depth to the Moho discontinuity are shown. This work is an extension of two previous papers : Chapter 2 which discusses Moho depths in Southern California and Chapter 3 which develops the tomographic method used here.

The primary purpose of this paper is to more thoroughly investigate lateral variations in Pn velocity. The Moho in Southern California is quite variable. Moho depth varies by 10 km and considerable anisotropy exists (Hearn, 1984; Vetter and Minster, 1981). Other parts of the crust and mantle also show large variations. The upper crust has wave velocities which directly reflect the surface tectonics by clearly defining the fault zones (Hearn and Clayton, 1984). Upper mantle studies find a high velocity ridge directly beneath the Transverse Ranges and low velocities underneath the Salton Trough (Humphreys et al., 1984; Walck and Minster, 1982; Raikes and Hadley, 1979). A detailed study of Moho velocities can give more insight into the tectonics of Southern California and allow one to tie upper mantle structure to

upper crustal structure more closely.

Method

The same tomographic backprojection used for Pg travel times (Chapter 3) is used. This iterative method simultaneously finds station and event delays as well as the lateral variations in Pn velocity. It is based upon a linearized version of the travel time equation for refracted arrivals (Hearn, 1984).

$$t_{ij} = a_i(s_0) + b_j(s_0) + \sum_{k=0}^{n} \Delta'_{ijk} s_k - 2Fs_0 \qquad (1)$$

This equation decomposes the travel time, t_{ij}, between station 'i' and event 'j' into three variable terms and a constant. The parameters a_i and b_j are the delays for station 'i' and event 'j'. They can be expressed as

$$a_i = \sqrt{s_c^2 - s_0^2}\ (h - z_e)$$

$$b_j = \sqrt{s_c^2 - s_0^2}\ h$$

where h is the refractor depth, z_e is the event depth and s_c and s_0 are the crustal slowness and mean refractor slownesses, respectively. The Southern California region is divided into a grid and the slownesses, 's_k' , of each element are found. The 'Δ'_{ijk}' is the distance the ray travels between station 'i' and event 'j' on the refractor face. The 'F" is the horizontal distance the ray travels between the refractor and the surface. Since this equation is applied to zero mean residuals the term with s_0 in equation (1) is assumed to be zero.

In tracing the ray across the grid the ray is only traced along the portion of the refractor on which the ray actually travels. In doing this, as opposed to tracing it from event to station, the delays are automatically corrected so that they all refer to the same refractor slowness, s_0. This way the delays can be correctly compared to each other. Note that the delays can only be determined within a constant factor so that only the relative magnitudes of the delays matter. The station delays are directly interpretable in terms of velocity and structure. The backprojection scheme is quite straightforward. The Pn travel time branch is visually windowed from the rest of the data (Figure 1). A line is then fit to the data and all residuals computed. Station and event delays are estimated by computing the average residual at each station and event. The slowness in each cell is estimated by computing the average apparent slowness for all rays passing through each cell weighted by the distance squared. The slowness image and the two sets of delays are then scaled to minimize the weighted rms residual. The iterative process converges quickly.

One of the artifacts of backprojection algorithms is azimuth bias. When raypaths are predominantly from one azimuth the slowness anomalies are blurred preferentially along that azimuth. This is compensated for by using azimuth averaged slowness estimates in a manner similar to Humphreys et al. (1984). Each slowness estimate is the unweighted average of the mean slownesses found for each of four nonredundant azimuth sectors of raypath approach. At the end of each iteration the station delays, event delays, and slowness image are all three scaled by multiplicative constants determined

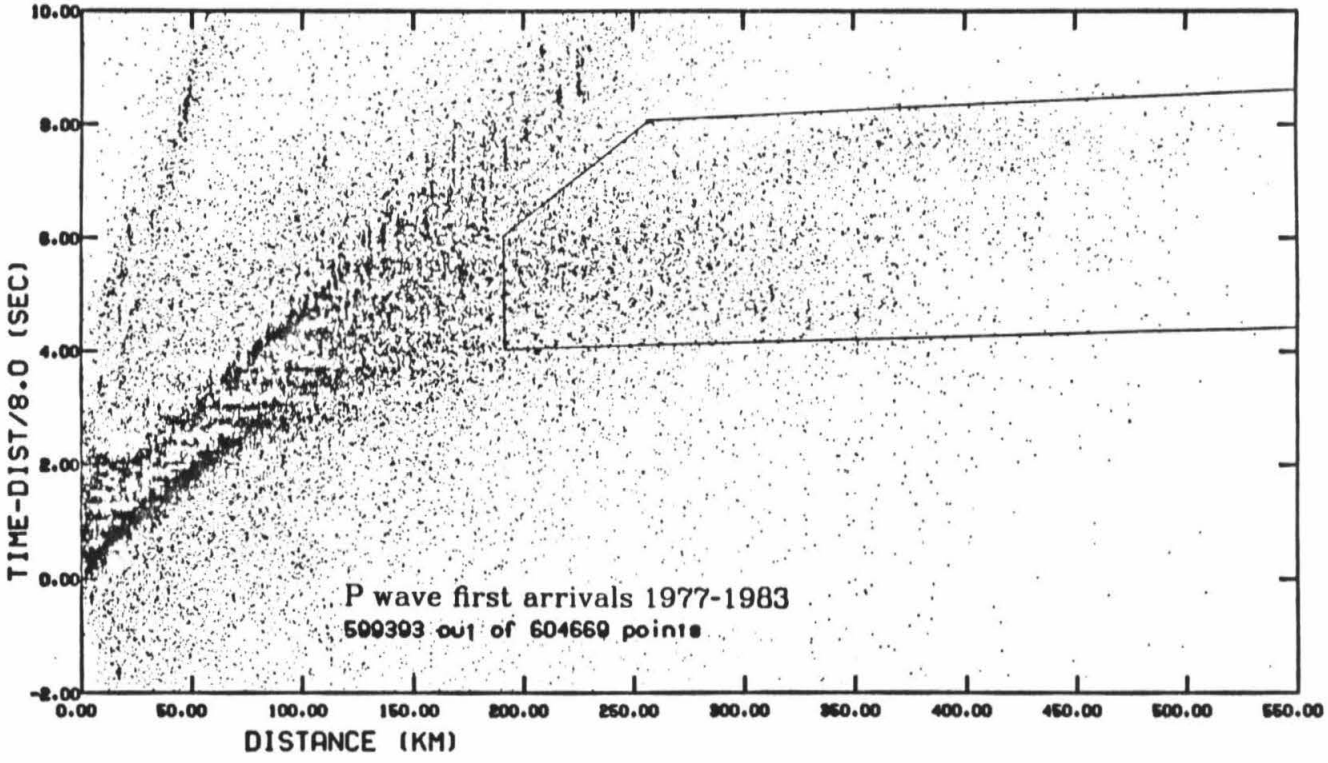

Figure 1. The P wave first arrival data for the Southern California array with the Pn arrivals windowed.

from a three parameter regression.

The processing is basically the same as in Chapter 3, used for the shallower Pg arrivals with only a few modifications. Azimuth weighting is used for Pn since there are fewer arrivals for Pn and so azimuth bias is a more severe problem. Also, cell sizes are larger here (10 km by 10 km) because there is less data and it is necessary to get an adequate number of rays per cell. Cells with ten or more hits and stations and events with 5 or more arrivals are used. Even so, some cells seem to collect noise and so large damping factors are used. The station delays are corrected for Pn by only tracing the raypath along the refractor for the actual path covered; for Pg the rays were actually traced from station to event and corrected for refractor velocity afterwards. Since Pn raypaths are more clearly defined and the path lengths are appreciably longer than the offset distance tracing, the actual refracted raypath is a more accurate representation of the true raypath here.

The data

Pn data collected on the Southern California array between 1978 and 1983 were used. This travel time branch was visually windowed from the rest of the data using a reduced travel time plot (Figure 1). The data were weighted as the inverse variances of 400, 100, 25 and 4 for quality 0, 1, 2 and 3 arrivals. Quality 4 arrivals were not used. A total of 6031 arrival times from 398 events were used. This data set is of poorer quality than used for Chapter 2 but has twice as many arrivals.

Results

The Pn apparent velocity anomalies in Southern California are pictured in Figure 2a and the associated station delays in Figure 2b. Some quite large velocity anomalies of over 1.0 km/s are imposed on the mean velocity of 7.8 km/s. The average velocity perturbation is 0.37 km/s. Station delays range over 2 s.

Both station delays and slowness distribution are quite similar to those computed earlier by Hearn (1984). The major differences between the two sets of delays occur primarily in the Los Angeles and the Ventura Basins. Differences of up to 0.4 s exist. As tests of the tomographic method on the same data of Hearn (1984) yielded the same results, this difference is due to the different data set and not the tomographic method. The different arrivals in this data set could be due to errors, either event location or timing, or due to undermodeling. As this data set was bulk processed, error control was not complete but hopefully the quantity of data has canceled this to some degree. Anisotropic parameters that are significant for Pn raypaths have been ignored (Hearn, 1984; Vetter and Minster, 1981). If rays to these stations came predominantly from a slow direction this could result in late static delays. Another important assumption implicitly made is that the static delays are azimuth independent. Many areas, particularly near the large basins, almost certainly have different crustal structures on opposite sides of them. This and other problems associated with not knowing the true raypath strongly affect the solution. Differences in solutions found with different ray sets demonstrate our lack of knowledge in properly modeling the raypaths.

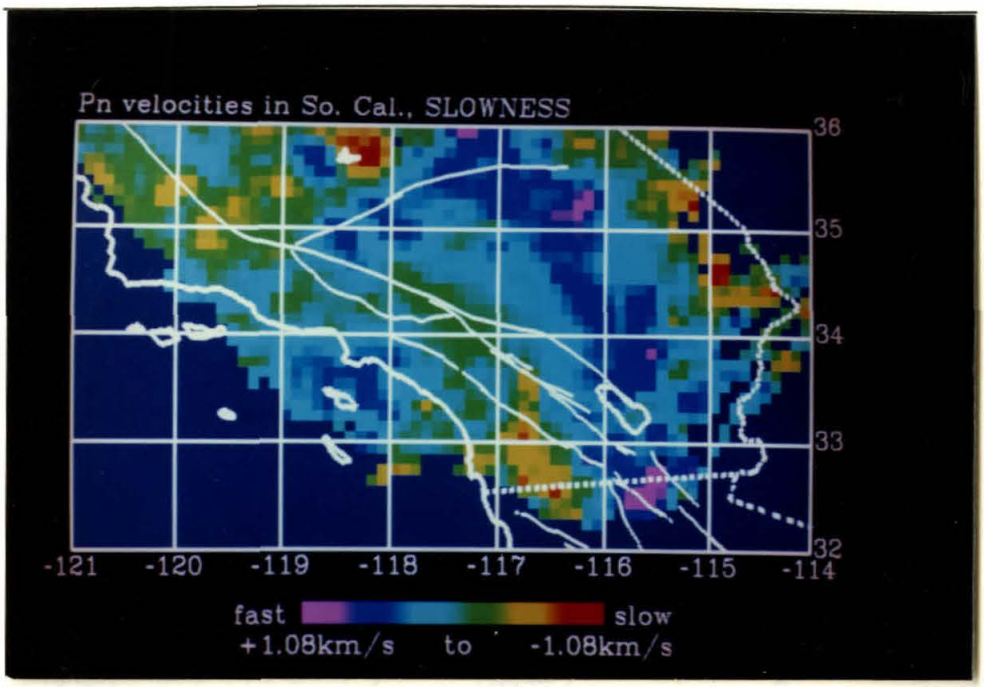

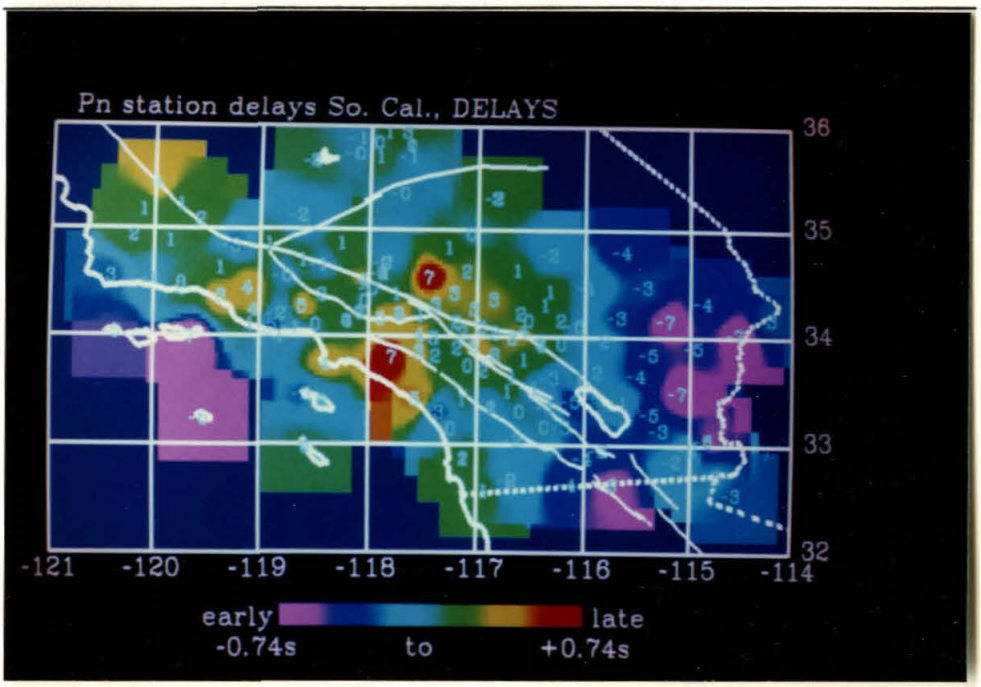

Figures 2a and b. Pn velocity variations in Southern California and Pn station delays in Southern California. Numbers in tenths of seconds.

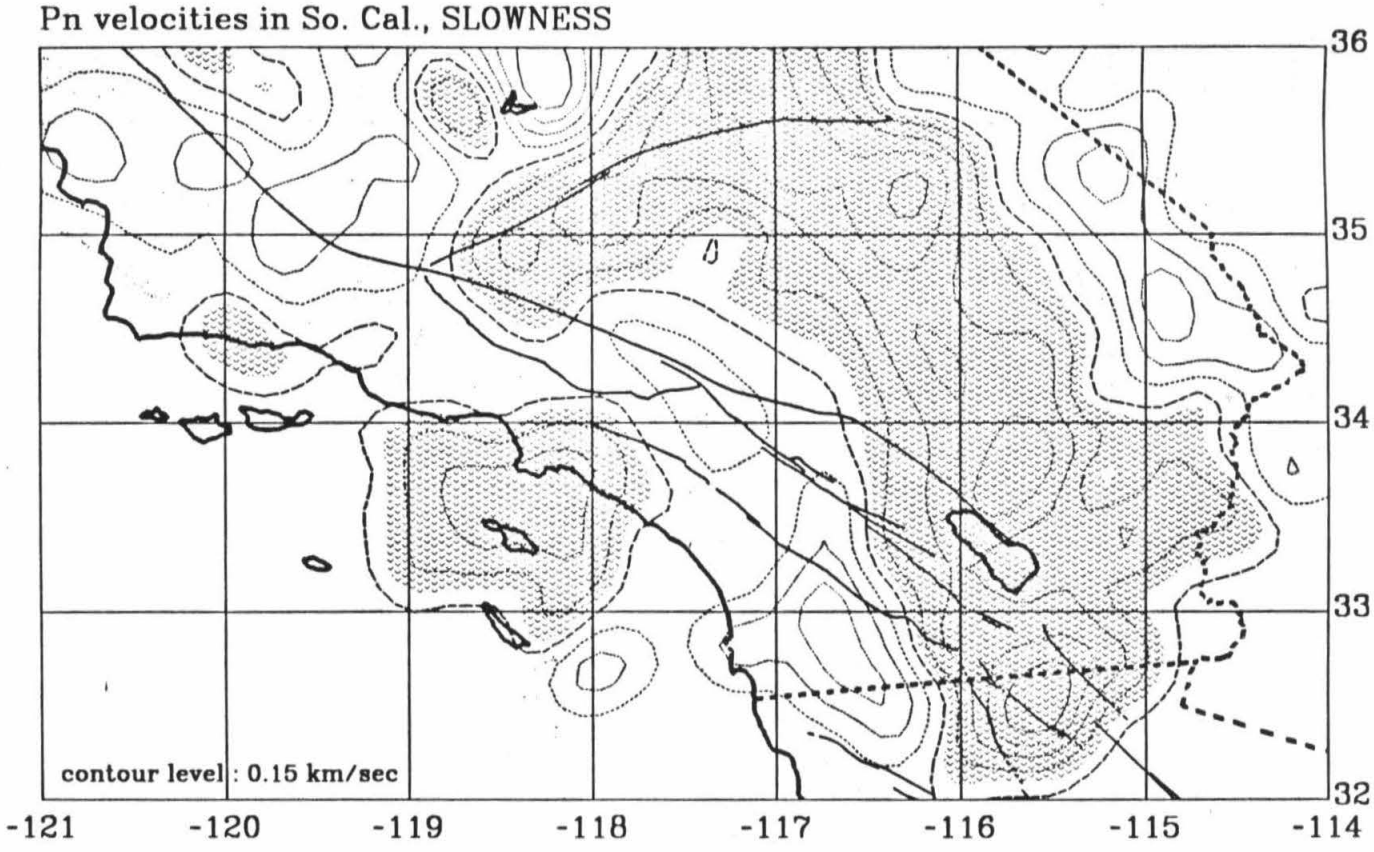

Figure 2c. Pn velocity variations in Southern California. Black and white version.

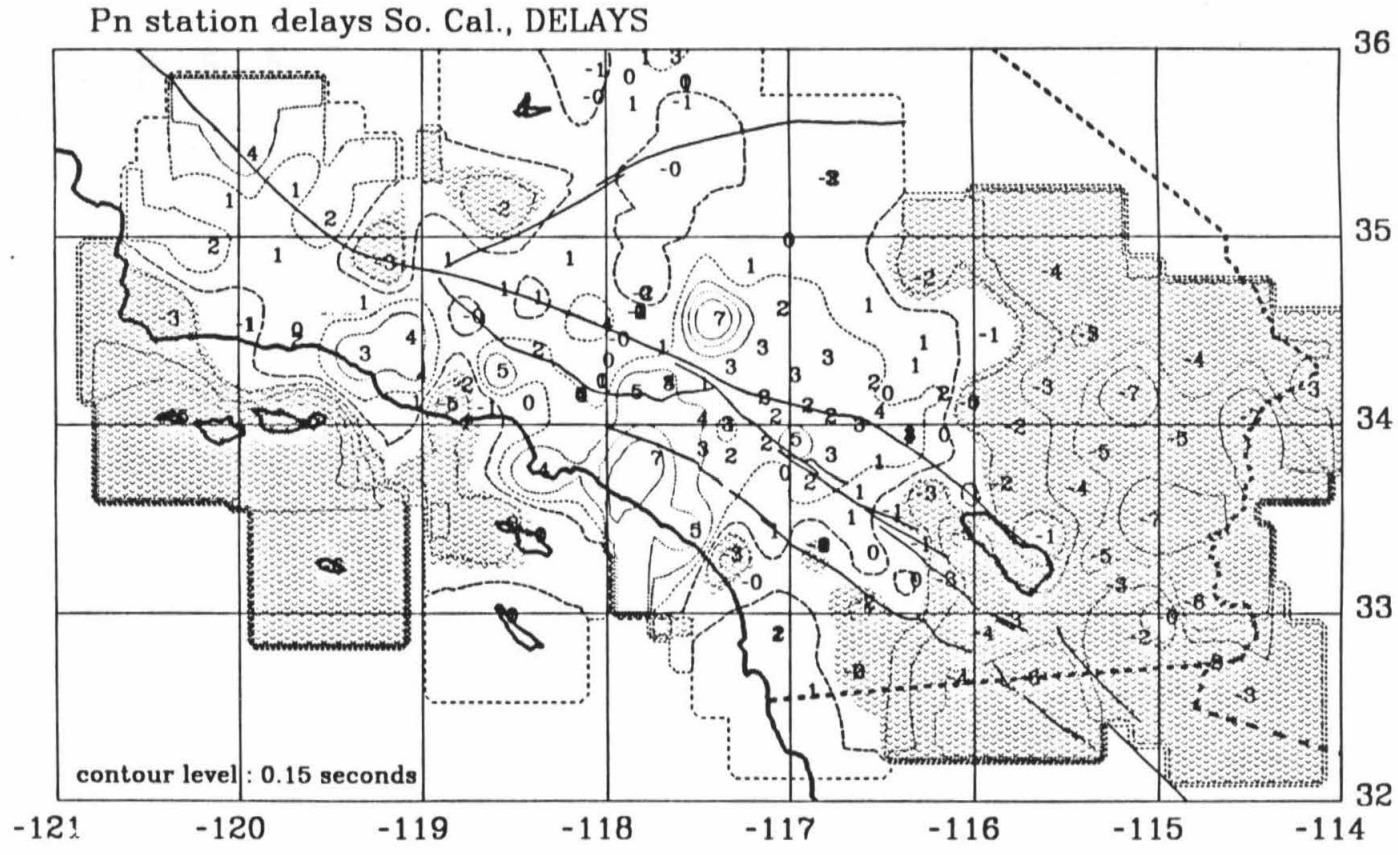

Figure 2d. Pn station delays in Southern California. Numbers in tenths of seconds. Black and white version.

Variance and resolution are demonstrated for the Pn results by using four synthetic models as was done for Hearn and Clayton (1984). Travel times are found for each model using the actual raypath set. The synthetic data are then inverted in the same manner as the data. Variance is determined by using a model consisting of gaussian noise. For a large amount of noise, 0.05 s standard deviation for the highest quality arrivals, the amplitudes are below that of the Pn anomalies. These noise results are shown in Figures 3a and b. Delay noise has a maximum value of 0.23 s and slowness noise maximum of 0.24 km/s. The absolute slowness deviation is 0.06 km/s. The resolution of individual slowness cells is shown in Figures 4a and b. Cell responses blur 50 km depending on the location. Ray streaking due to azimuth bias is quite apparent in more poorly sampled regions. The 0.6 km/s cells turned on give responses of 0.4 km/s and trade off little with the delays causing small 0.1 s values. In Figures 5a and b the response for station delays of 0.1 s is shown at selected stations. These are reconstructed very accurately and cause almost no tradeoff with the slownesses.

The last synthetic is designed to investigate the slowness-delay tradeoff. The original model has horizontal stripes in the slowness image of 0.3 km/s and vertical stripes in the delay image of 0.15 s. Comparison of Figures 6a and 6b shows the tradeoff between the crossing stripes. We see from these figures as well as from the previous results that some areas are not as well reconstructed as others. The slowness amplitude is too high by a factor of 4 and errors in delays can be as high as 0.4 s. The mean absolute velocity deviation is 0.46 km/s. The northeast section of the slowness image is heavily

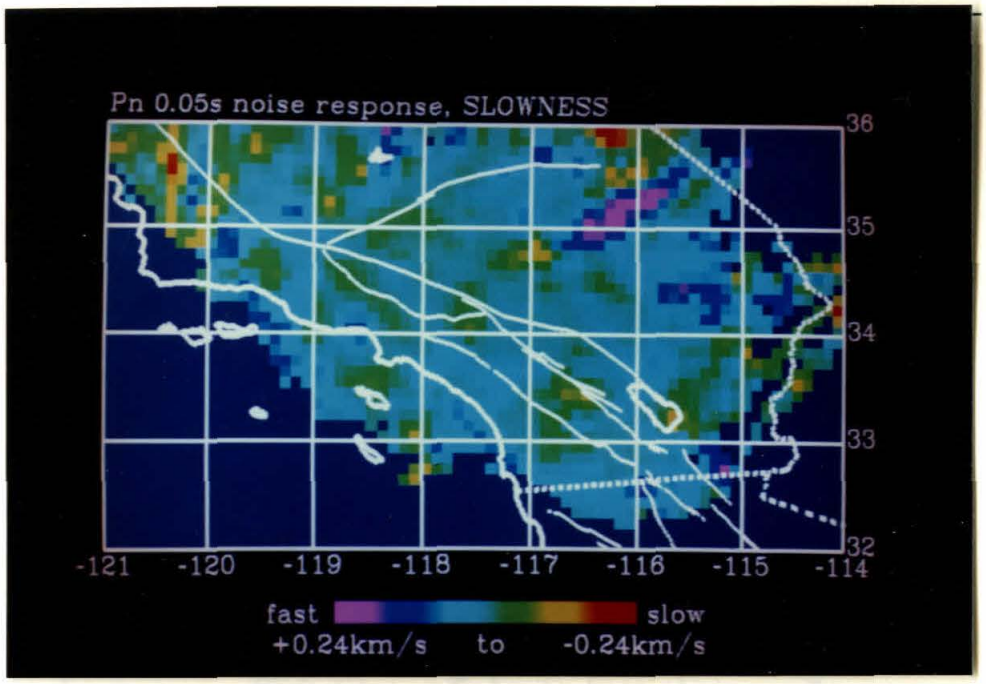

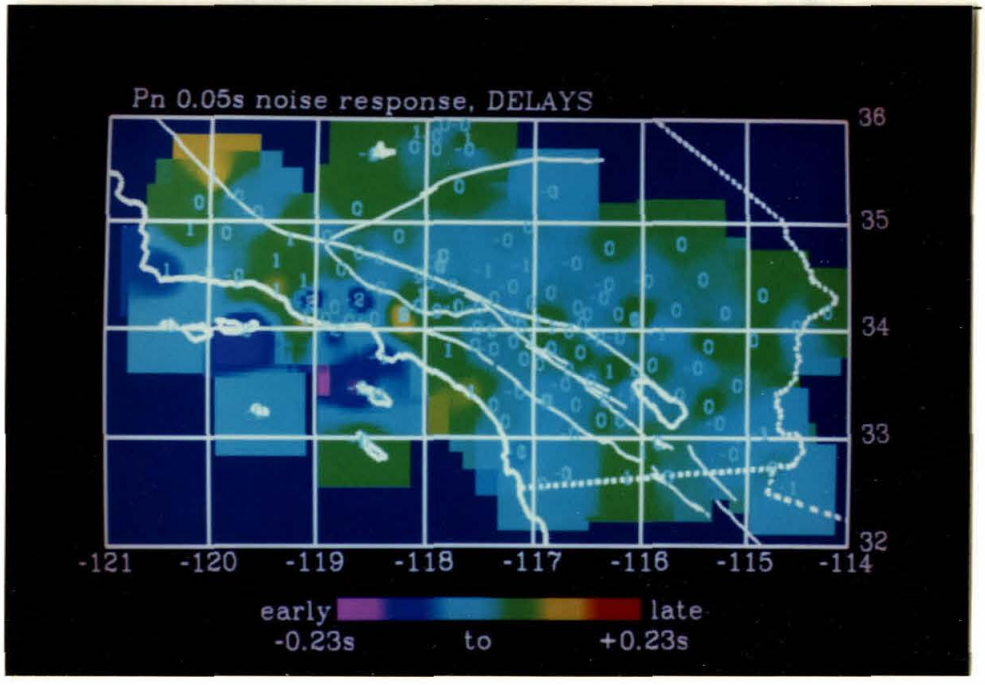

Figures 3a and b. The noise response of Pn velocities and of Pn station delays. Pure noise with a standard deviation of 0.05 s was input. Numbers in tenths of seconds.

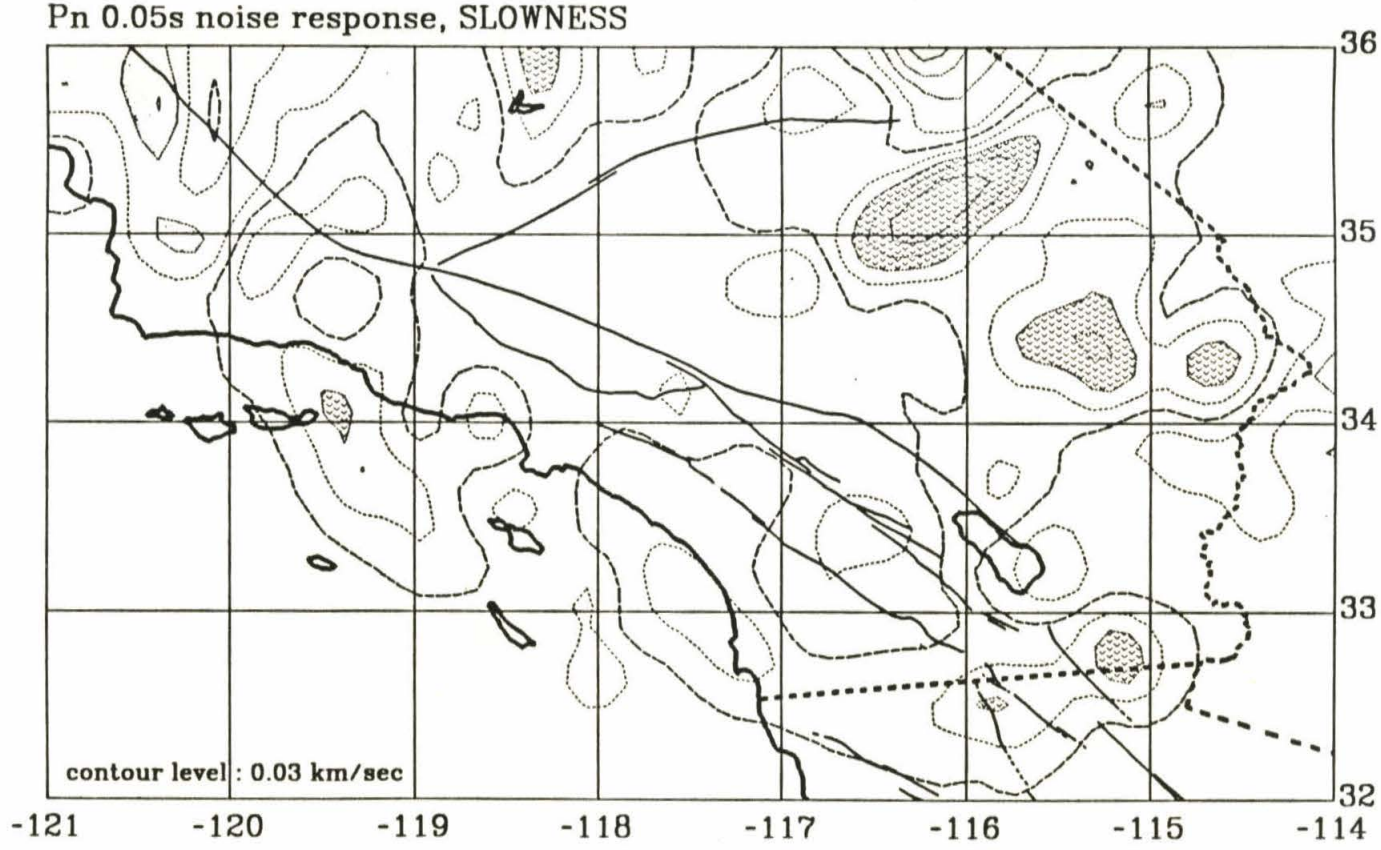

Figure 3c. The noise response of Pn velocities. Pure noise with a standard deviation of 0.05 s was input. Black and white version.

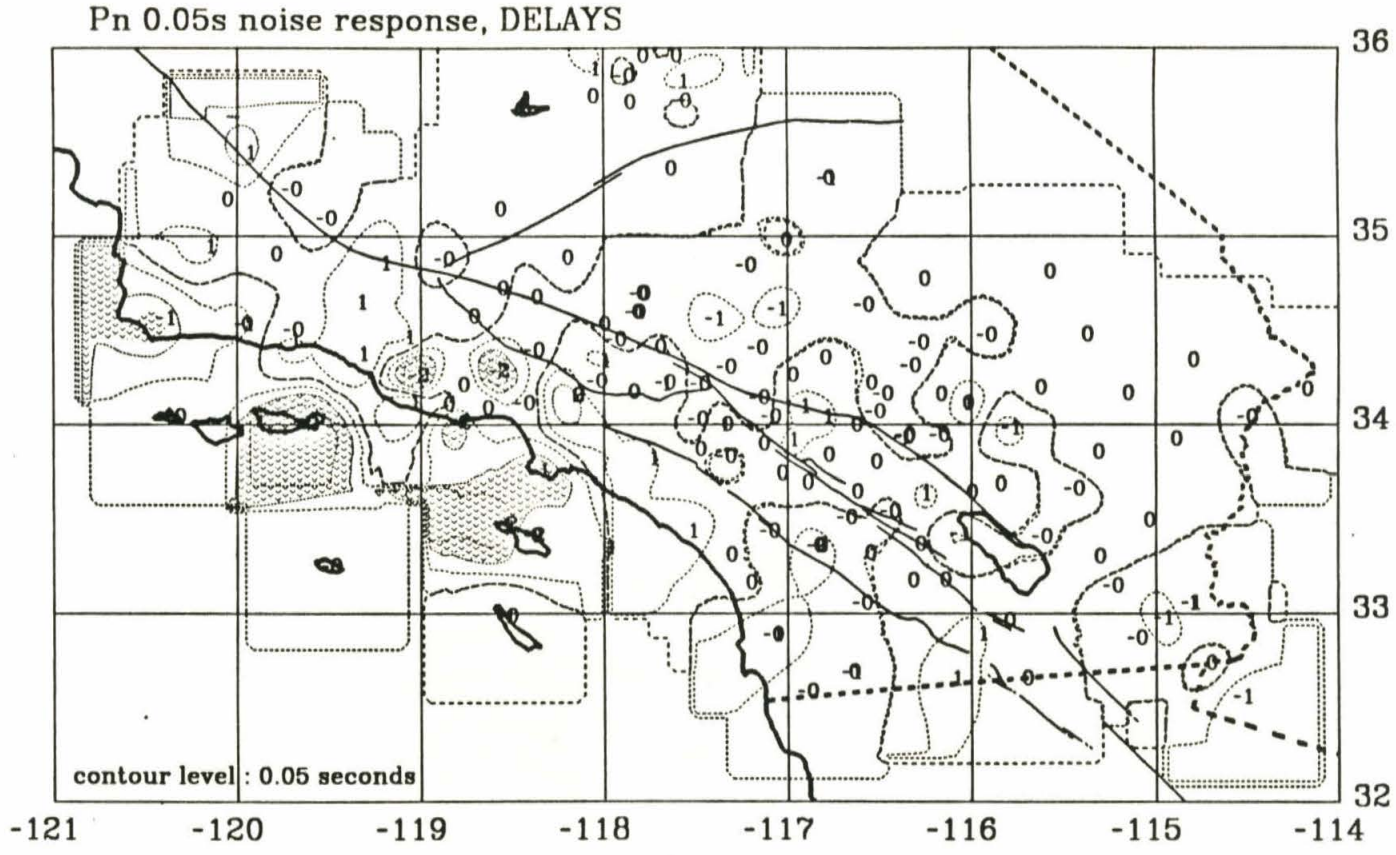

Figure 3d. The noise response of Pn station delays. Pure noise with a standard deviation of 0.05 s was input. Numbers in tenths of seconds. Black and white version.

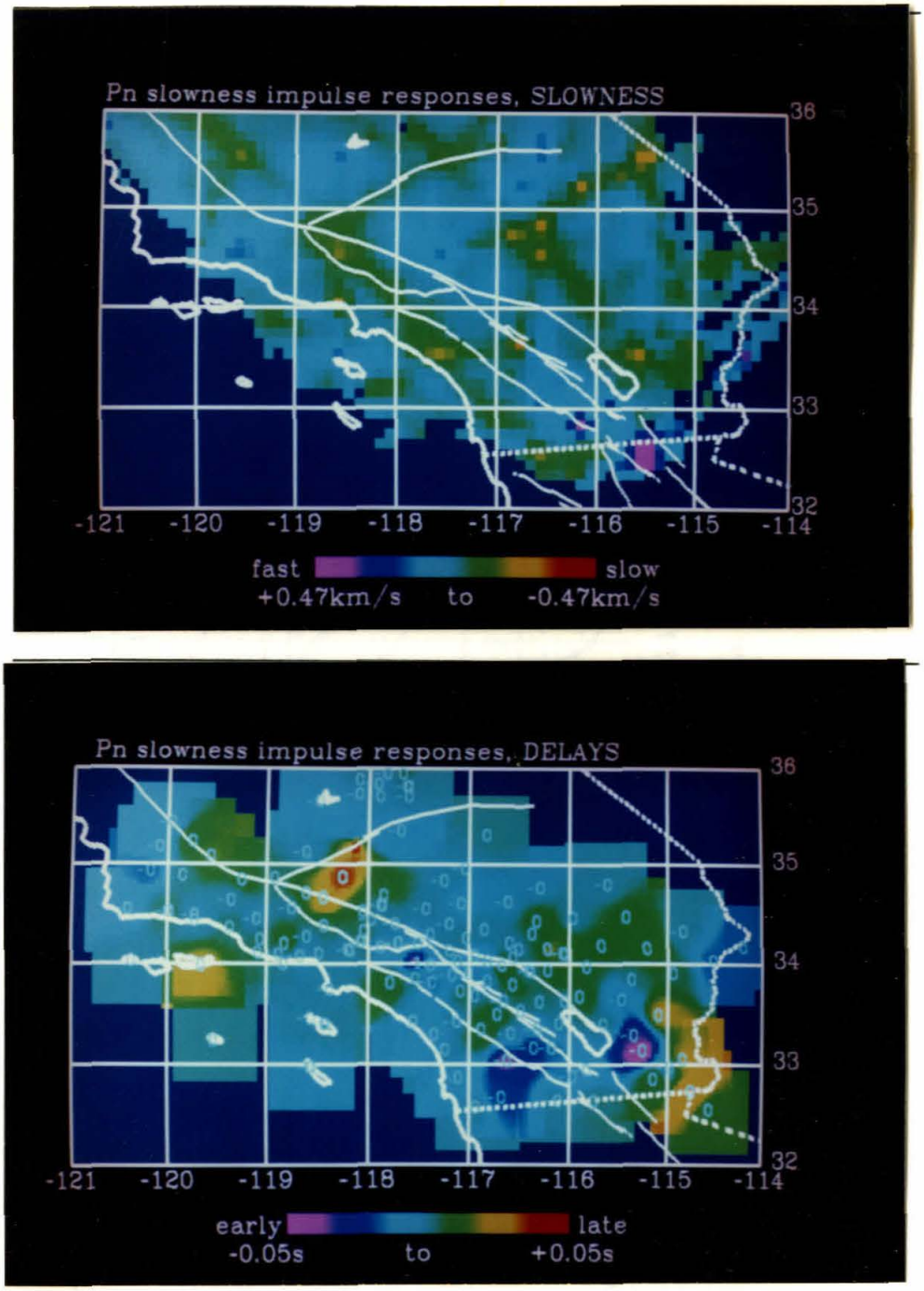

Figures 4a and b. The slowness response of individual slowness cells for Pn arrivals and the station delay response of individual slowness cells for Pn arrivals. Numbers in tenths of seconds.

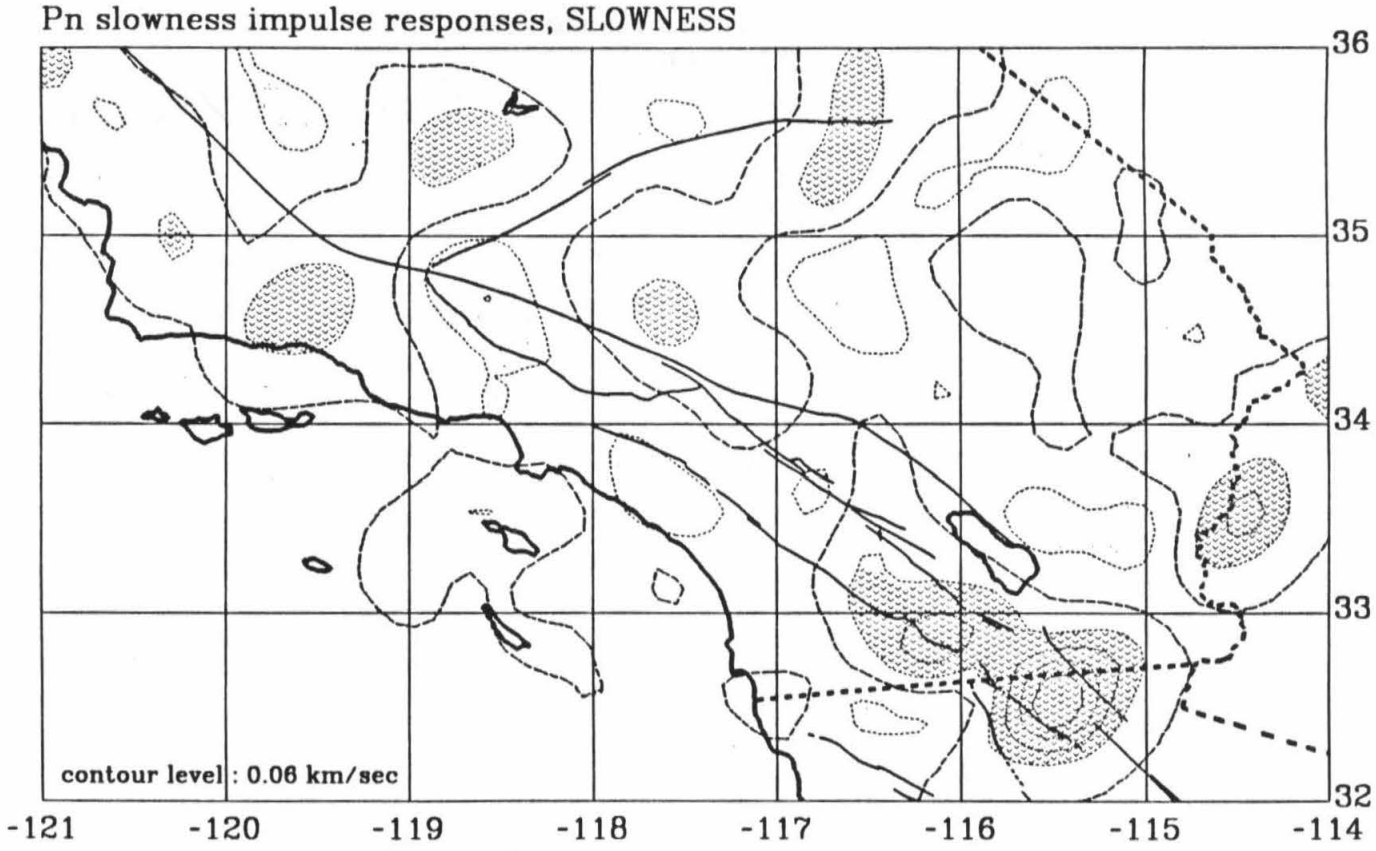

Figure 4c. The slowness response of individual slowness cells for Pn arrivals. Black and white version.

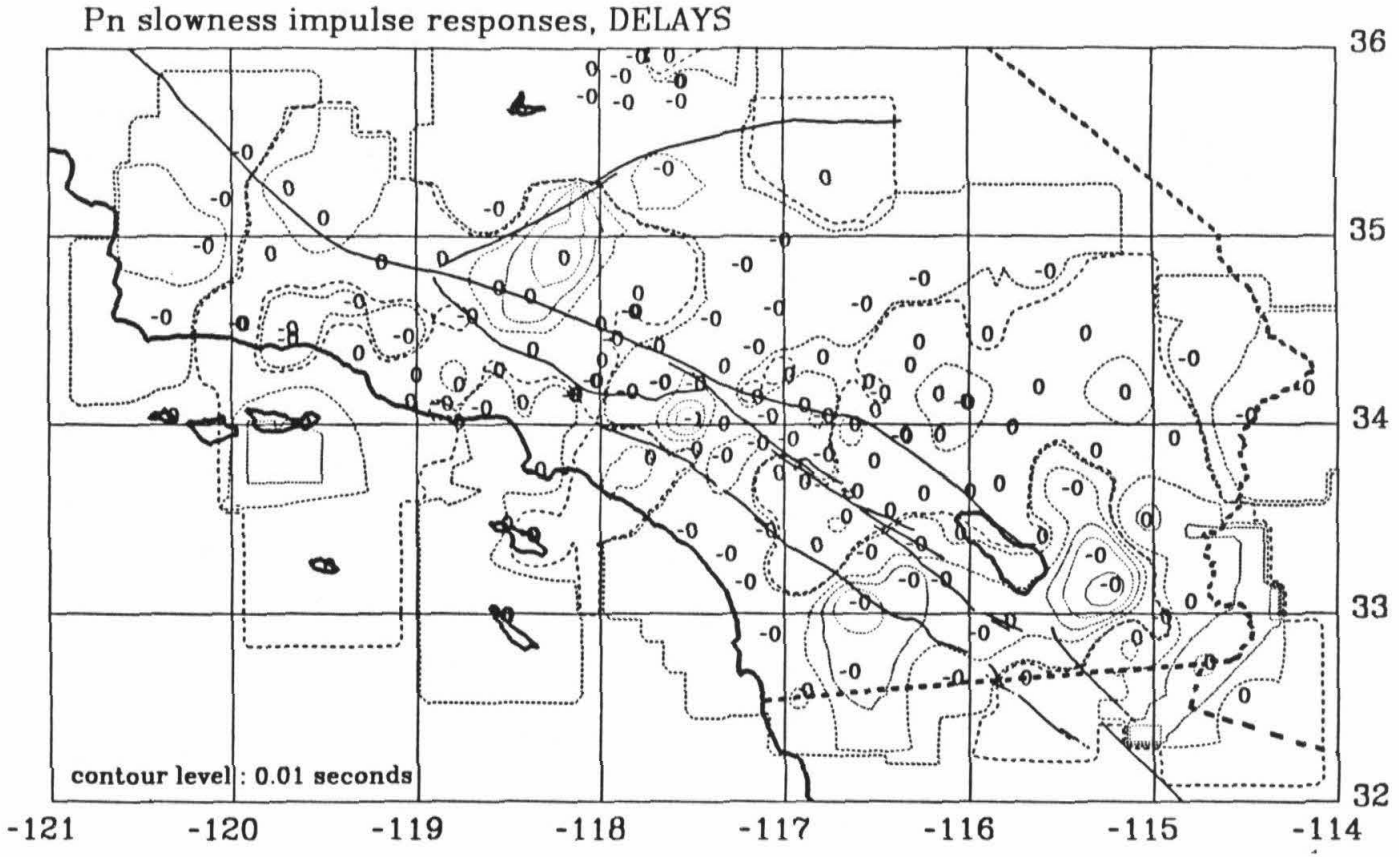

Figure 4d. The station delay response of individual slowness cells for Pn arrivals. Numbers in tenths of seconds. Black and white version.

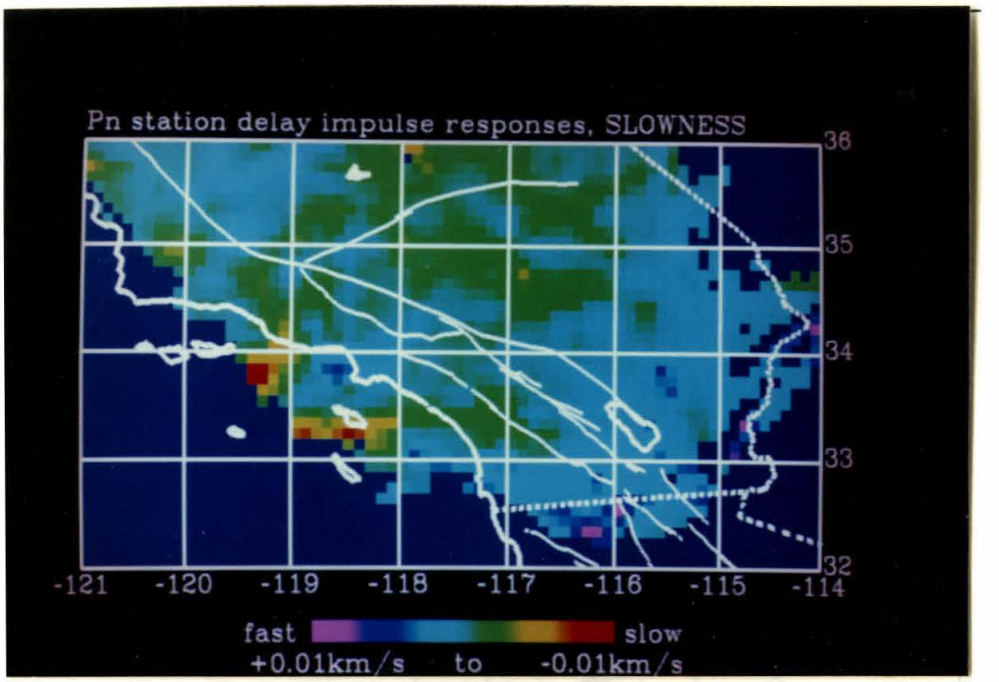

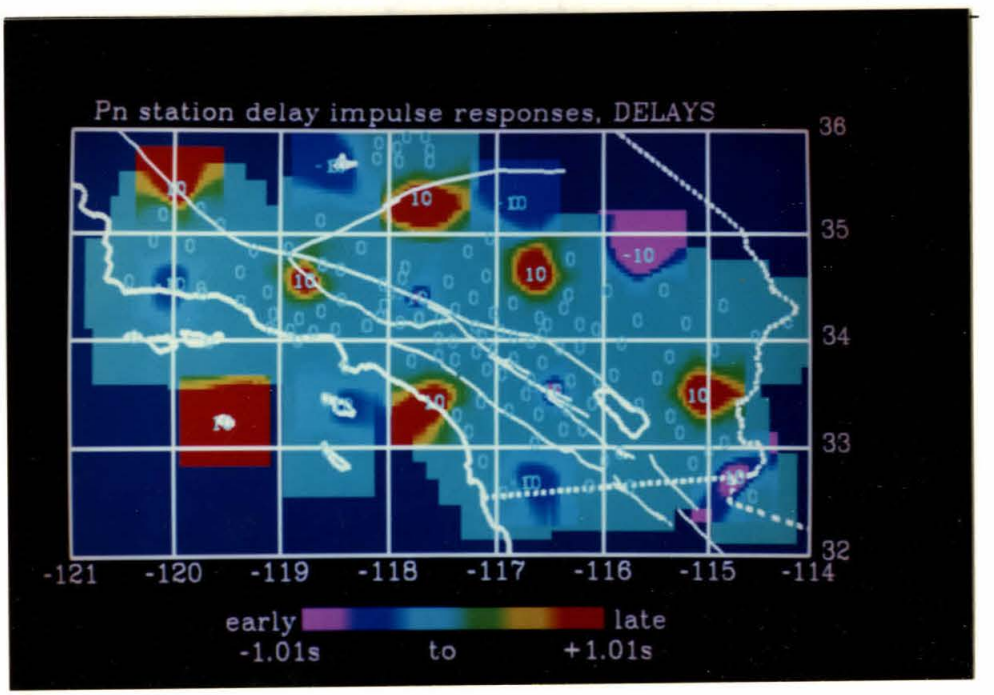

Figures 5a and b. The slowness response of individual station delays for Pn arrivals and the station delay response of individual station delays for Pn arrivals. Numbers in tenths of seconds.

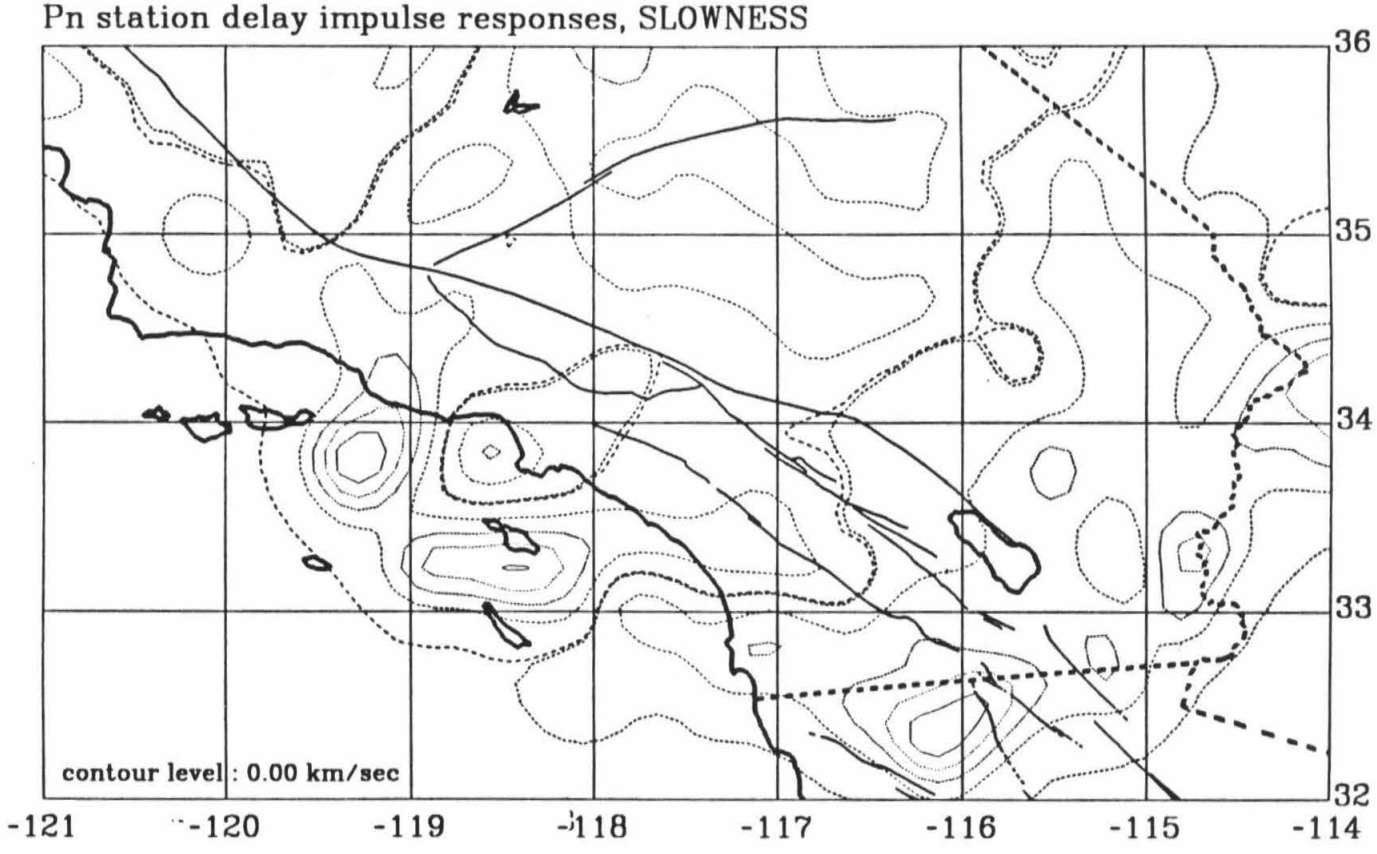

Figure 5c. The slowness response of individual station delays for Pn arrivals.

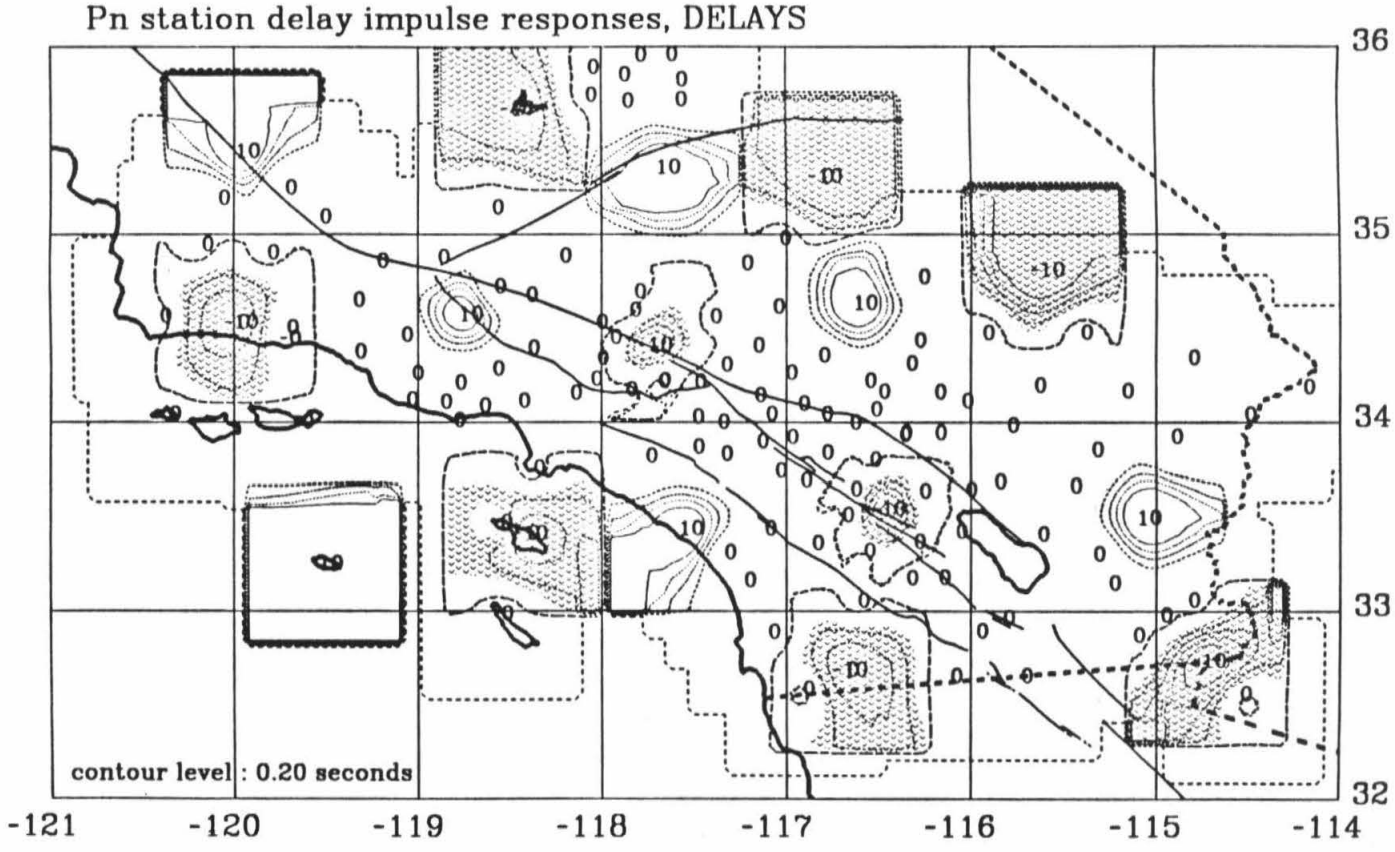

Figure 5d. The station delay response of individual station delays for Pn arrivals. Numbers in tenths of seconds. Black and white version.

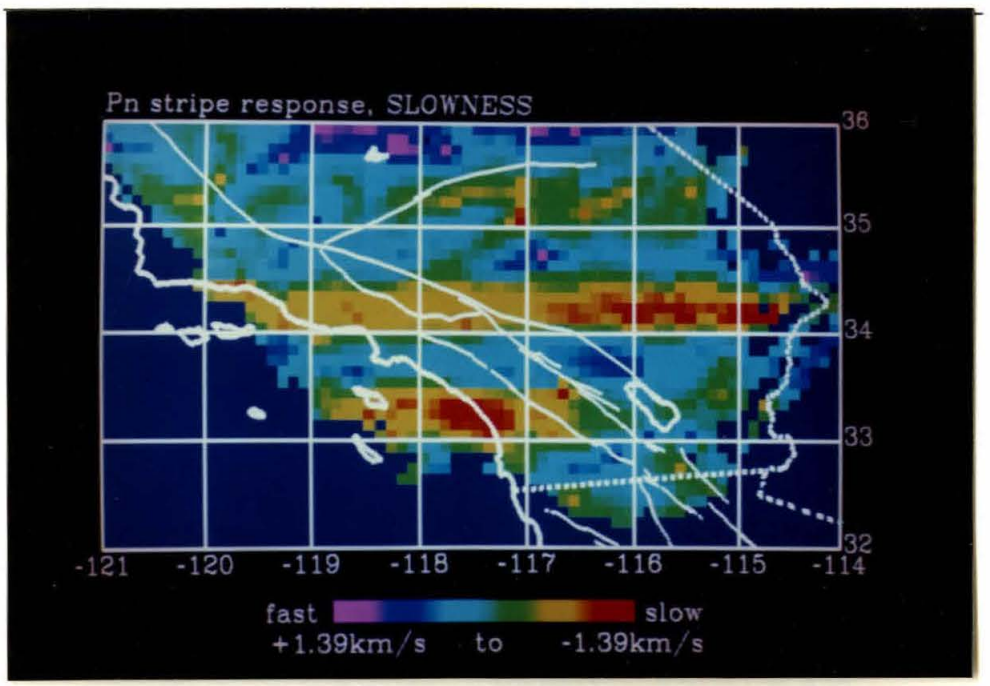

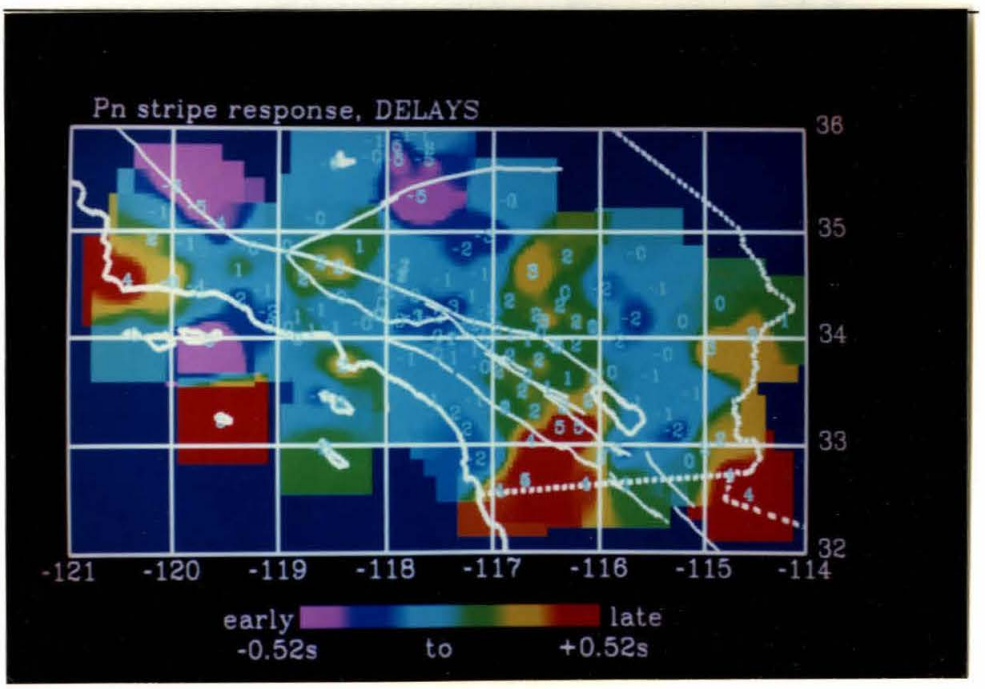

Figures 6a and b. The slowness response for Pn arrivals to a test pattern and the station delay response for Pn arrivals to a test pattern. The original model had horizontal stripes in slowness variations and vertical stripes in the delay variations. Numbers in tenths of seconds.

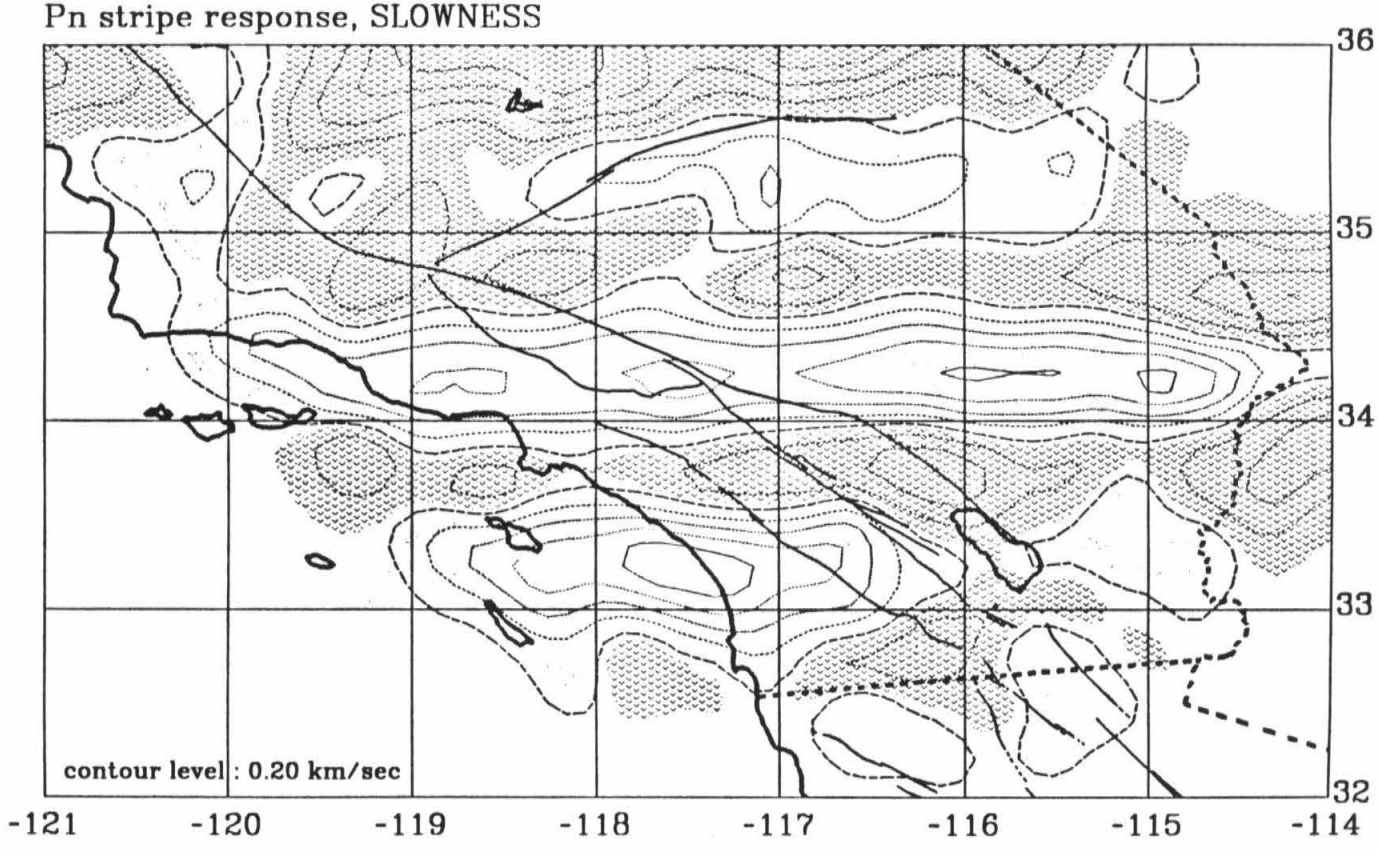

Figure 6c. The slowness response for Pn arrivals to a test pattern. The original model had horizontal stripes in slowness variations and vertical stripes in the delay variations. Black and white version.

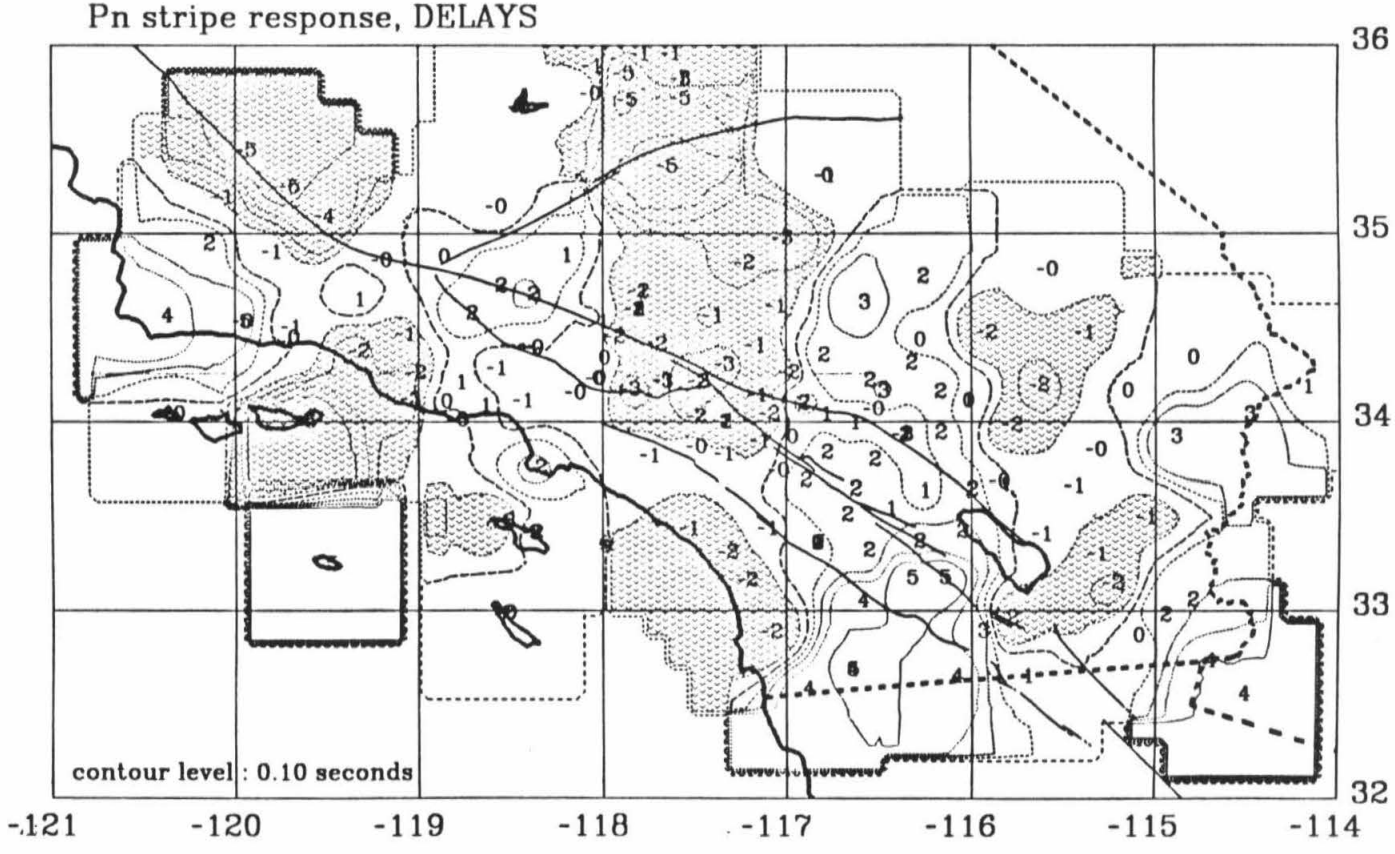

Figure 6d. The station delay response for Pn arrivals to a test pattern. The original model had horizontal stripes in slowness variations and vertical stripes in the delay variations. Numbers in tenths of seconds. Black and white version.

biased by streaking along a northwest azimuth. Reconstruction is most accurate in the center of the plot.

Discussion

In the eastern Mojave a large amount of fast material exists. This anomaly appears to have a northwesterly strike with quite a sharp boundary on its southwest side. There are a large number of events at the Coso area, at the northernmost part of the array, which contribute to streaking in the northwest azimuth. To some extent these high velocities also arise from blurring the early delays in the easternmost part of the array to the northwest. These higher velocities extend down into the Salton Trough and into the Gulf of California. This is especially surprising since the Salton Trough is a spreading center where hotter, lower velocity, material is expected. Indeed, Humphreys et al. (1984) find slow velocities in and under the Salton Trough from teleseismic arrivals. In fact his cross section has low velocities extending into the crust where high velocity mafic material exist (Fuis et al., 1981). Most likely, the actual zone of rifting in the trough is simply too narrow to resolve. The narrow dimension of the rifted zone is near 25 km, and the resolution is not quite that good. Alternatively, the raypaths may be refracting through higher velocity material which has underplated the rift zone.

Slower apparent Pn velocities seem to underlie the Transverse Ranges and part of the Peninsular Ranges. The Transverse Ranges do show a small root in the station delays and this is what is most likely delaying raypaths

crossing this region. Similarly the southern Sierra Nevada around Lake Isabella shows slow Pn velocities, also due to a mountain root. A deep root is not necessarily required to cause an appreciable delay. The Peninsular Ranges show no evidence for a root in the delays so we conclude that truly low Pn velocities do exist here. The slow Pn region in the Peninsular Ranges coincides with an area of an anomalously high isostatic gravity anomaly (Oliver, 1981) but a connection between the two is not clear.

The Mojave Desert along the Colorado River shows the early delays that have been discussed in more detail in Chapter 2. These arrivals result from a thin 22 km crust that centers along the Colorado River. This region also has higher Pn velocities (~8.2 km/s). Structurally, Pn velocities in the area probably represent conditions when this portion of North America was formed while the shallow depths of the Moho represent more recent extensional tectonics associated with early basin-range extension (Zoback et al., 1981).

Pn velocities do not show the dramatic contrast along fault zones that has been found for Pg rays. Unfortunately, we do not have the resolution that was obtained there. Velocities on the North American plate are distinctly higher than those on the Pacific plate and the mean delays are less on the North American plate. The transition occurs over no more than 100 km. The Moho discontinuity is at a depth where the earth deforms in a ductile manner. Although the plate boundary certainly extends to this depth the boundary may be a broad zone of deformation. The results indicate that the apparent Pn velocities along the San Andreas have been decreased due to the root of the Transverse Ranges. This makes defining the width of the plate boundary

difficult.

Chapter 5

Conclusions and Speculations

Crustal structure and tectonics in Southern California

The studies of this thesis extend the surface tectonics of Southern California downward so that differences in the tectonic responses of the upper and lower crust can be seen. The San Andreas Fault clearly extends as a planar feature to at least 10 km, but not necessarily to Moho depths. The apparent Pn velocities, which represent velocities at the surface of the mantle, are different on the Pacific and the North American plates, but there is no clear contrast between them. Similarly, San Jacinto Fault is present at Pg depth levels but not apparent in the Pn results.

This separation of the crust from the mantle is because of their different rheological regimes. The upper crust is brittle and seismic while the lower crust is ductile and aseismic. Their responses to tectonic forces are quite different and this has led to the separate velocity patterns for the Pg and the Pn arrivals.

One mechanism for separating the upper brittle crust from the lower, ductile crust is detachment faulting. These nearly flat faults occur at mid-crustal depths and move aseismically. Older detachments in Southern California that have been exposed at the surface include the Rand Thrust, the

Pelona Thrust, and the Whipple Mountains Thrust. Recently Crouch et al. (1984) presented reflection data which show the coastal Hosgri Fault zone turning into a nearly flat fault in the midcrust. He infers that much of the California Coast Ranges are underlain by such detachments and their topography is largely caused by movement on these surfaces. Recent COCORP profiles in the Mojave (Cheadle et al., 1984) show many possible detachments.

Our methods in evaluating array data cannot directly detect detachment faulting; however, several observations are made that are easily explained by such faults occurring in the crust. The Transverse Ranges are not apparent at Pg depths (~10 km). This implies that the rock types under the ranges at this depth are the same as those found adjacent to the mountains at that depth. The Transverse Ranges then could be allochthonous features which have ridden on detachment surfaces to their present location. These detachment surfaces are at depths shallower than 10 km. Seismicity under the San Bernardino Mountains extends only to 5 km north of the San Andreas while it extends to depths deeper than 15 km south of the San Andreas (Corbett, 1984). This shallow seismicity base defines the brittle to ductile contact under the ranges and could be a good site for detachment faulting. Similarly, the Tehachapi Range should have a low Sierran velocity at depth but there is no indication of this. These mountains, too, do not seem to extend to the midcrust. Either the base of the batholith is shallow or the batholith has been moved.

The Peninsular Ranges show characteristic high velocities that correspond to their high density. The San Jacinto block, however, is distinct.

It has slower Mojave-type velocities. The Peninsular Ranges may be overriding the opposing plate in this area on a detachment surface. At depth the plate boundary is or has been under the San Jacinto Fault zone. The San Jacinto Fault only has 30 km of displacement on it and so it could be a late developing feature of the overthrusting.

If these detachments occur within the upper half of the crust and continue to occur in the lower half, it is not surprising that the Moho velocity pattern is different from the upper crust. Detachment faulting effectively separates the brittle interactions on the surface from the ductile interactions at depth thus enabling the upper and lower crust to act independently. At deep depths the crust is responding more to isostatic compensation operating along the fault at Cajon Pass than it is to the shear force across the plate boundary.

The sediment delay is quite apparent from the Pg data results. Detailed structural studies have been done by Fuis et al. (1982) who infer high velocity intrusive rocks beneath the valley fill. Our results show the same high velocities in the upper crust and our delays show the sedimentary fill. We also find high velocities in the Pn rays. This is surprising since the Salton Trough, a spreading center, is underlain by partially melted, low velocity, mantle (Humphreys et al, 1984; Walck, 1982). Several explanations exist for the fast Pn rays. The actual spreading center may be too narrow to resolve at this depth. The zone of new crust is the width of the Central Valley (20 km) by the offset on the San Andreas (200 km). Alternatively, mantle material may freeze onto the base of the crust forming a thin high velocity solid layer over a lower

velocity partially melted mantle. No evidence exists for any anomalously thin crust in the Trough. As the plates pull apart one might expect the thickness of newly formed crust to be near the thickness of normal ocean crust plus the sediment thickness. If such a region exists it is too narrow to be seen without a detailed experiment. The American plate adjacent to the trough is thin (22 km) compared to the adjacent Pacific Plate (25 km).

The thin crust of the Colorado River region is part of the thin crust that dominates the Basin and Range Region. This thin crust exists in the Nevada portion (Priestly, 1981) of the Basin and Range region as well. In the Colorado River region we associate the thin crust with the metamorphic core complex that exists there. Large detachment surfaces are also exposed in the region. Crustal thinning seems to have occurred by stretching of the lower crust and fracturing on normal faults in the upper crust. The detachment provides a surface separating the two regions. Zoback (1981) has reviewed evidence that suggests two phases of extension in the Basin and Range region. They associate crustal thinning with the first phase of extension that occurred prior to the Miocene.

Isostatic balance in Southern California is a confusing issue. The western Transverse Ranges have a small root (Lamanuzzi, 1981). This can be seen in both the Pn static delays and by the slow patch in apparent Pn velocities. The eastern Transverse Ranges do not seem to have a local root but a broad root, which also balances the topographically high Antelope Valley region, may be present. Low gravity values (Oliver, 1981) reflect a crustal root under the western Transverse Ranges. The isostatic balance of the Transverse Range

province is complicated by the upper mantle high velocity anomaly that underlies them (Humphreys et al., 1984; Walck and Minster, 1982; Raikes and Hadley, 1979). Statically, this anomaly should result in a broad high gravity anomaly superimposed on the crustal gravity anomalies. Dynamically, however, the high velocity mantle anomaly should be sinking thus pulling the crust downward causing low gravity values.

In contrast to the Transverse Ranges there is little evidence for a root in the Peninsular Ranges. None of the stations within this province show any appreciable delay. High upper crustal velocities in the ranges correspond to the high density mafic granites of the batholith. Pn velocities, however, are anomalously low. The Bouguer Gravity anomaly for these ranges does show a trend of low gravity following the crest of the ranges. Calculation of isostatic gravity anomalies (Oliver, 1981), assuming a constant density crust, shows that a major isostatic balance problem exists in the western Peninsular Ranges. A large platform of relatively high Bouguer gravity anomaly extends from the San Diego coast inward to the Elsinore Fault (Oliver, 1981). The gravity high does correspond to a patch of slow Pn velocity but no obvious connection exists. Teleseismic results show no anomalous mantle there. If the Peninsular Ranges are in isostatic balance it is not accomplished with a constant density crust. Rock densities decrease from west to east within the Peninsular Ranges (L.T. Silver, pers. comm.). If this trend extends sufficiently deep into the crust then isostatic balance can be maintained without a root.

A simple calculation can give some insight into the balance of the Peninsular Ranges. First, let us assume a flat Moho under a flat-bottomed batholith

and restrict all density anomalies to the batholith. Mass balance can then be used to estimate the depth of compensation, which, for our assumptions, is the base of the batholith. Densities within the range vary between 2.75 to 2.85 gm/cc and the 750 m is the topographic relief. The depth of compensation is then given by :

$$h = \frac{750m \times 2.75gm/cc}{0.10gm/cc} = 20.6km.$$

This calculation indicates that for isostatic balance the Peninsular Ranges extend down into the lower half of the crust. Of course variations in the basal depth of the batholith also can also accommodate the isostatic balance.

Even if the Peninsular Ranges are isostatically balanced internally within the province there is still a problem in balancing them relative to the rest of Southern California. The observed 27 km average depth in the region is less than the average California crustal thickness. The regional compensation of the Peninsular Ranges must be accomplished by a low density lower crust or upper mantle or by dynamic forces produced by the plate motions.

References

Aki, K. and P. G. Richards, *Quantitative Seismology, Vol. 2*, W. H. Freeman and Company, San Francisco, CA., 1980.

Backus, G. E., Possible forms of seismic anisotropy of the uppermost mantle under oceans, *J. Geophys. Res.*, *70*, 3429-3439, 1965.

Bamford D., M. Jentsch, and C. Prodehl, Pn anisotropy studies in northern Britain and the eastern and western United States, *Geophys. J. R. Astron. Soc.*, *57*, 397-429, 1979.

Bamford, D., Pn velocity anisotropy in a continental upper mantle, *Geophys. J. R. Astron.. Soc.*, *49*, 29-48, 1977.

Bamford, D., An example of the iterative approach to time term analysis, *Geophys. J. R. Astron. Soc.*, *31*, 365-372, 1973a.

Bamford, D., Refraction data in western Germany-A time term interpretation, *Z. Geophys.*, *39*, 907-927, 1973b.

Bath, M., An analysis of the time term method in refraction seismology, *Tectonophysics*, *51*, 155-169, 1978.

Bierman, G. J., *Factorization Methods for Discrete Sequential Estimation*, Academic Press, New York, 1977.

Bracewell, R. N., Strip integration in radio astronomy, *Aust. J. Phys.*, *9*, 198-217, 1956.

Bracewell, R. N. and A. C. Riddle, Inversion of fan beam scans in radio

astronomy, *Astrophys. J.*, *150*, 427-434, 1967.

Cheadle, M.J., B.L. Czuchra, T. Bryne, C.J. Ando, J.E. Oliver, L.D. Brown, S. Kaufman, P.E. Malin, and R.A. Phinney, The deep crustal structure of the Mojave Desert, California, from COCORP reflection data, in press, 1984.

Clayton, R. W. and R. P. Comer, Reconstruction of mantle heterogeneity by iterative backprojection of travel times : 2 Results for P waves, in press, 1984.

Comer, R. P. and R. W. Clayton, Reconstruction of mantle heterogeneity by iterative backprojection of travel times : 1 Accuracy and resolution, in press, 1984.

Corbett, E. J., Seismicity and crustal structure studies of Southern California : Tectonic implications from improved earthquake locations, Ph. D. Thesis, California Institute of Technology, Pasadena, CA., 1984.

Crossen, R. S., and N. I. Christenson, Transverse isotropy of the upper mantle in the vicinity of pacific fracture zones, *Bull. Seismol. Soc. Am.*, *59*, 59-72, 1969.

Crouch, J.K., S.B. Bachman, and J.T. Shay, Post-Miocene compressional tectonics along the central California margin, in *Tectonics and Sedimentation Along the California Margin*, Pacific Section SEPM, Vol. 38, 35-54, 1984.

Davis, G. A., J. L. Anderson, E. G. Frost, and T. J. Shackelford, Mylonitization and detachment faulting in the Whipple-Buckskin-Rawhide Mountains terrain, Southeastern California and Western Arizona, in *Cordilleran Metamorphic Core Complexes*, *Geol. Soc. Am. Mem.*, *153*, 79-129, 1980.

Deans, S. R., *The Radon Transform and some of its Applications*, John Wiley and Sons, New York, NY, 1983.

Dines, K. A. and R. J. Lytle, Computerized geophysical tomography, *Proc. IEEE, 67*, 1067-1073, 1979.

Draper, N. R., and H. Smith, *Applied Regression Analysis*, John Wiley and Sons, New York, NY, 1966.

Dzewonski, A. and D.L. Anderson, Seismic Tomography, *Scientific American*, in press, 1984.

Elders, W. A., W. R. Rex, T. Meidav, P. T. Robinson, and S. Biehler, Crustal spreading in Southern California, *Science, 178*, 15-24, 1972.

Ergas, R. A., and D. D. Jackson, Spatial variations of crustal seismic velocities in Southern California, *Bull. Seismol. Soc. Am., 71*, 671-689, 1981.

Fuchs, K., Seismic anisotropy of the subcrustal lithosphere as evidence for dynamical processes in the upper mantle, *Geophys. J. R. Astron. Soc., 49*, 167-179, 1977.

Fuis, G.S., W.D. Mooney, J.H. Healy, G.A. Mechan and W.J. Lutter, Crustal structure of the Imperial Valley Region, in *"The October 15, 1979 Imperial Valley Earthquake", U. S. Geol. Surv. professional paper, 1254*, 25-50, 1982.

Hadley, D., Geophysical investigations of the structure and tectonics of Southern California, Ph.D. Thesis, California Institute of Technology, Pasadena, 1978.

Hadley, D., and H. Kanamori, Seismic structure of the Transverse Ranges, California, *Geol. Soc. Am. Bull., 88*, 1769-1478, 1977.

Hadley, D. and H. Kanamori, Crustal structure and temporal velocity change in Southern California, *Pageoph.*, *113*, 157-280, 1975.

Healy, J. N., Crustal structure along the coast of California from seismic refraction measurements, *J. Geophys. Res.*, *68*, 5777-5787, 1963.

Hearn, T. M., Pn travel times in Southern California, *J. Geophy. Res.*, *89*, 1843-1855, 1984.

Hearn, T. M. and R. W. Clayton, Upper crustal structure in Southern California from a tomographic analysis of array data, in preparation, 1984.

Hill, R. I., Petrology and petrogenesis of batholitic rocks, San Jacinto Mountains, Southern California, Ph.D. Thesis, California Institute of Technology, Pasadena, CA, 1984.

Humphreys, E., R. W. Clayton, and B. H. Hager, A tomographic image of mantle structure beneath Southern California, *Geop. Res. L.*, *11*, 625-627, 1984.

Husebye, E. S., A. Christoffersson, K. Aki, and C. Powell, Preliminary results on the 3-dimensional seismic structure of the lithosphere under the USGS seismic array, *Geophys. J. R. Astron. Soc.*, *46*, 319-340, 1976.

Johnson, C. E., CEDAR -- an approach to the computer automation of short-period local seismic networks, Ph.D. Thesis (part 1), California Institute of Technology, Pasadena, 1979.

Keller, B., Pn in the western Transverse Ranges, preprint, University of California, Santa Barbara.

Kind, R., Residuals and velocities of Pn waves recorded on the San Andreas Seismograph Network, *Bull. Seismol. Soc. Am.*, *62*, 85-100, 1972.

Lamanuzzi, V., Relative Pn travel time residuals for stations in Southern

California, Master's Thesis, University of Southern California, Los Angeles, 1981.

Luyendyk, B. P., M. J. Kamerling, R. Terres, Geometric model for Neogene crustal rotations in Southern California, *Geol. Soc. Am. Bull.*, *91*, 211-217, 1980.

Menke, W., The resolving power of cross-borehole tomography, *Geophys. Res. Lett.*, *11*, 105-108, 1984.

Morris, G. B., R. W. Raitt, and G. G. Shor, Velocity anisotropy and delay-time maps of the mantle near Hawaii, *J. Geophys. Res.*, *74*, 4300-4316, 1969.

Nava, F. A., and J. N. Brune, An earthquake-explosion reversed refraction line in the Peninsular Ranges of Southern California and Baja California Norte, *Bull. Seismol. Soc. Am.*, *72*, 1195-1206, 1982.

Okal, E. A., and J. Talandier, Rayleigh wave phase velocities in French Polynesia, *Geophys. J. R. Astron. Soc.*, *63*, 719-733, 1980.

Oliver, H.W., ed., Interpretation of the gravity map of California and its continental margin, *Calif. Div. Mines Geol. Bull.*, *205*, 1982.

Pakiser, L. C., and J. N. Brune, Seismic models of the root of the Sierra Nevada, *Science*, *21*, 1088-1094, 1980.

Pechmann, J. C., The relationship of small earthquakes to strain accumulation along the San Andreas Fault, Ph.D. Thesis, California Institute of Technology, Pasadena, 1983.

Powell, R. E., Geology of the crystalline basement complex, eastern Transverse Ranges, Southern California : Constraints on regional tectonic interpretation, Ph. D. Thesis, California Institute of Technology, CA., 1981.

Priestley, K. F., A. S. Ryall, and G. S. Fenzie, Crust and mantle structure in the northwest Basin and Range province, *Bull. Seismol. Soc. Am.*, *72*, 911-923, 1982.

Radon, J., A translation of Radon's 1917 paper, in *The Radon Transform and some of its applications*, by S.R. Deans, John Wiley and Sons, New York, N.Y., 204-217,1917

Raikes, S. A., and D. Hadley, The azimuthal variation of teleseismic *P*-residuals in Southern California: Implications for upper-mantle structure, *Tectonophysics*, *56*, 89-96, 1979.

Raikes, S. A., The azimuthal variation of teleseismic P-wave residuals for stations in Southern California, *Earth Planet Sci. Lett.*, *29*, 367-372, 1976.

Raikes, S. A., Regional variations in upper mantle structure beneath Southern California, *Geophys. J. R. Astron. Soc.*, *63*, 187-216, 1980.

Raitt, R. W., G. G. Shor, T. J. G. Francis, and G. B. Morris, Anisotropy of the Pacific upper mantle, *J. Geophys. Res.*, *74*, 3095-3109, 1969.

Raitt, R. W., G. G. Shor, and H. K. Kirk, Mantle anisotropy in the Pacific Ocean, *Tectonophysics*, *12*, 173-186, 1971.

Roland, S. W., Computer implementation of image reconstruction formulas, in *Image Reconstruction from Projections*, G. T. Herman, ed., Springer-Verlag, Berlin, 1979.

Roller, J. C., and J. H. Healy, Seismic-refraction measurements of crustal structure between Santa Monica Bay and Lake Mead, *J. Geophys. Res.*, *68*, 5837-5849, 1963.

Rosenfeld, A. and A. C. Kak, *Digital Picture Processing*, *Vol. 1*, Academic

Press, New York, N. Y., 1982.

Scheidegger, A. E., and P. L. Willmore, The use of a least squares method for the interpretation of data from seismic surveys, *Geophysics*, *22*, 9-22, 1957.

Shor, G. G., Deep reflections from Southern California blasts, *EOS Trans. AGU*, *36*, 133-138, 1955.

Shor, G. G., and R. W. Raitt, Seismic studies in the Southern California continental borderlands, *Proc. Int. Geol. Cong. 20th*, 243-259, 1958.

Simmons, R. S., Seismicity of San Diego, 1934-1974, *Bull. Seis. Soc. Amer.*, *67*, 809-826, 1977.

Sinno, Y. A., G. R. Keller, and M. L. Sbar, A crustal seismic refraction study in west central Arizona, *Jour. Geop. Res.*, *86*, 5023-5038, 1981.

Thatcher, W., and J. N. Brune, Surface waves and crustal structure in the Gulf of California region, *Bull. Seismol. Soc. Am.*, *63*, 1689-1698, 1973.

Vetter, U., and J. B. Minster, Pn velocity anisotropy in Southern California, *Bull. Seismol. Soc. Am.*, *71*, 1511-1530, 1981.

Walck, M. C., and J. B. Minster, Relative array analysis of upper mantle velocity variations in Southern California, *J. Geophys. Res.*, *87*, 1757-1772, 1982.

Warren, D. H., A seismic-refraction survey of central Arizona, *Geol. Soc. Am. Bull.*, *80*, 257-282, 1969.

Wesson, R. L., J. C. Roller and W. H. K. Lee, Time-term analysis and geological interpretation of seismic travel time data from the Coast Ranges of central California, *Bull. Seis. Soc. Amer.*, *63*, 1447-1471, 1973.

Willmore, P. L. and A. M. Bancroft, The time term approach to refraction seismology, *Geophys. J. R. Astron. Soc.*, *3*, 419-432, 1960.

Zoback, M. L., R. E. Anderson and G. A. Thompson, Cainozoic evolution of the state of stress and style of tectonism of the Basin and Range province of the western United States, *Phil. Trans. R. Soc. Lond.*, *300*, 407-434, 1981.